TorsinA and Neuronal Nuclear Pore Complex Biogenesis

by

Sumin Kim

A dissertation submitted in partial fulfillment
of the requirements for the degree of
Doctor of Philosophy
(Cellular and Molecular Biology)
in the University of Michigan
2023

Doctoral Committee:

Associate Professor Sami J. Barmada, Chair
Associate Professor Stephanie L. Bielas
Associate Professor Catherine A. Collins, Case Western University
Professor William T. Dauer, UT Southwestern
Professor Phillis I. Hanson

Sumin Kim

suminkim@umich.edu

ORCID iD: 0000-0002-7388-819X

© Sumin Kim 2023

Acknowledgements

Many people have supported me throughout the process of getting a Ph.D. in Cellular and Molecular Biology. First and foremost, I would like to thank my advisors, Drs. Bill Dauer and Sami Barmada. Bill has been instrumental in shaping who I am as a scientist. My approach to science and who I strive to be as a member of the scientific community are heavily influenced by his mentorship. Even after moving to Texas, he has been supportive, making sure that I have everything I need and always starting our meetings asking how I am doing. I am grateful for Sami for allowing me to join the lab in my third year and continue to work on my thesis project in his lab. Sami's positivity has helped uplift me countless times when I felt skeptical about my science and career. I also learned a lot about different topics (RNA, neurodegenerative research) in Sami's lab and his expertise helped expand my scientific scope throughout graduate training. Bill and Sami have both always been unequivocally supportive of my goals, including encouraging my attendance at multiple conferences and providing strong support for the many fellowships and grants I have applied for. Their mentorship has allowed me to become an independent, confident scientist. I feel very fortunate to have a great relationship with both mentors, and they have shaped what kind of mentor I want to be as I continue my journey in science.

I am also grateful for Dr. Sam Pappas, who has been my constant source of support for many years and whose findings sparked this dissertation work. Sam is an incredibly kind, supportive, and patient mentor and a great friend as well. He has met with me weekly even after moving to Dallas to make sure I feel supported and less isolated. He is a fantastic mentor and I feel

very lucky to have had the chance to learn from him and get to know him for the past several years. I also thank Dr. Sarah Veatch, without whom several key aspects of the projects would not have been possible. I was able to explore multiple different fluorescent labeling and microscopy methods thanks for her and her lab, which were wonderful learning experiences. I also appreciate her constant support including coming to my ASCB conference presentation this past year. She has also supported my applications for several fellowships and offered lots of helpful insights regarding academia, funding, publishing etc.

Throughout this Ph.D., I also received mentorship from many faculty members regarding my project, career and navigating academia. In particular, I thank Dr. Dan Yellajoshyula, a previous postdoc in the Dauer lab, for his support, guidance, and advice, and my thesis committee members, Drs. Cathy Collins, Stephanie Bielas, and Phyllis Hanson, for their feedback on this project and helping me prioritize directions.

I would like to thank my friends from graduate school, especially Anna-Lisa Lawrence, Maria Virgilio, and Amanda Erwin, for being a big part of my support system and for the countless conversations about graduate education, being women in science, and scientific project ideas. I also thank Jay Li, who started in the Dauer lab around the same time – I cannot not imagine a better labmate and friend to have shared the first several years of this PhD with.

I thank my partner, Ben Meinen. Ben has been a part of my Ph.D. journey from the first year. Seeing each other grow as scientists and exploring new places together have been key highlights from the past several years. I am very excited for our future together in the same city again. Lastly, I am immensely grateful for my parents. I am a scientist thanks to their unwavering support and love.

Table of Contents

Acknowledgements ii
List of Figures vii
Abstract viii
Chapter 1 Introduction 1
1.1 The Nuclear Envelope and Nuclear Pore Complexes 1
1.1.1 Nuclear pore complex architecture 1
1.1.2 Function of the nuclear pore complex 2
1.1.3 Spatial distribution of nuclear pore complexes 4
1.1.4 Nuclear pore complex assembly 4
1.1.5 Regulation of NPC number 6
1.1.6 Nuclear pore complexes in neurons and neurological diseases 7
1.2 TorsinA and DYT1 Dystonia 7
1.2.1 DYT-TOR1A dystonia 7
1.2.2 TorsinA: an atypical AAA+ protein 8
1.2.3 TorsinA molecular function 9
1.2.4 TorsinA at the nuclear envelope 10
1.2.5 TorsinA and neuronal nuclear pore complexes 11
Chapter 2 Research Design and Methods 15
2.1 Mouse husbandry 15
2.2 Generation of HaloTag-Nup107 mouse line 15
2.3 Primary neuron culturing 16
2.4 Differentiation of induced pluripotent stem cells 16
2.5 Western blot 17
2.6 qPCR of torsinA transcripts 18
2.7 Light microscopy 18
2.7.1 Immunofluorescene labeling for confocal and structured illumination microscopy 18
2.7.2 Sample preparation and imaging for direct stochastic optical reconstruction microscopy 19
2.7.3 HaloTag-Nup107 labeling 19
2.7.4 NLS-mCherry-NES reporter assay 20
2.7.5 PolyA+ fluorescence in situ hybridization 20
2.7.6 Expansion microscopy 21
2.7.7 Microscopes and image acquisition 22
2.8 Electron microscopy 23
2.8.1 Transmission electron microscopy 23
2.8.2 Scanning transmission electron microscopy tomography 24
2.9 Image analysis 24
2.9.1 NPC segmentation from dSTORM 24
2.9.2 Autocorrelation analysis of dSTORM and SIM data 26
2.9.3 Calculation of nearest neighbor distances from dSTORM segmented NPCs 26
2.9.4 Determination of nucleoporin puncta localization and density from SIM data 27
2.9.5 Nearest neighbor distance analysis of SIM data 27

2.9.6 Nucleoporin puncta colocalization 27
2.9.7 Nuclear rim fluorescence intensity measurement of nucleoporins 28
2.9.8 Nuclear-cytoplasmic ratio calculations 28
2.9.9 Nuclear envelope bleb analysis 29
2.10 Statistics 29
2.11 Code availability 30
2.12 Data availability 30
Chapter 3 Nuclear Pore Complex Biogenesis is Upregulated during Neuronal Maturation 32
3.1 Abstract 32
3.2 Introduction 33
3.3 Results 35
3.3.1 NPC density increases during neuronal maturation 35
3.3.2 Novel HaloTag-Nup107 knock-in allele enables labeling of endogenous NPC dynamics 36
3.3.3 NPC increase is observed in maturing induced pluripotent stem cell-derived neurons 38
3.4 Discussion 39
Chapter 4 TorsinA is Essential for the Timing and Localization of Neuronal Nuclear Pore Complex Biogenesis 53
4.1 Abstract 53
4.2 Introduction 54
4.3 Results 56
4.3.1 TorsinA is essential for uniform NPC distribution but not upregulation of NPC density 56
4.3.2 TorsinA-deficient neurons exhibit abnormal nucleocytoplasmic transport 59
4.3.3 Neurons homozygously harboring the disease-relevant ΔE mutation exhibit abnormal NPC clusters 61
4.3.4 Sites of NPC biogenesis are abnormal in torsinA-KO neurons 62
4.3.5 NE blebs form at sites of NPC biogenesis 63
4.3.6 Bleb-associated NPCs exhibit narrow channel size 64
4.3.7 NE blebs resolve as neurons continue to mature 65
4.3.8 Completion of NPC assembly is delayed in torsinA-KO neurons 65
4.4 Discussion 66
Chapter 5 Assessing the Critical Temporal Window of TorsinA Function in Developing Neurons 93
5.1 Abstract 93
5.2 Introduction 94
5.3 Results 95
5.3.1 A TetO-Tor1a mouse line to modulate torsinA expression 95
5.3.2 TorsinA expression cannot be induced in maturing primary neurons 96
5.3.3 Loss of torsinA exclusively in maturing neurons causes abnormal NPC clustering 98
5.3.4 TorsinA suppression is ineffective later maturing neurons 99
5.4 Discussion 100
Chapter 6 Discussion and Future Directions 108
6.1 Regulation of NPC number 108
6.2 Determinants of NPC localization 110
6.3 Impact of aberrant NPC biogenesis on torsinA-KO neuronal function 112

6.4 The emergence and disappearance of NE blebs 114
6.5 Neuronal NPC biogenesis as a critical period 116
6.6 Closing thoughts 117
Bibliography 119

List of Figures

Figure 1.1: NPC architecture 13
Figure 1.2: NPC assembly mechanisms 14
Figure 2.1: Segmentation of NPCs from dSTORM images 31
Figure 3.1: Nuclear pore complex biogenesis is upregulated during neuronal maturation 42
Figure 3.2: Identification and analysis of nucleoporin puncta 44
Figure 3.3: Multiple NPC components exhibit density increase during neuronal maturation 45
Figure 3.4: Validation of HaloTag-Nup107 mouse line 47
Figure 3.5: Neurons bearing a novel HaloTag-Nup107 knock-in allele demonstrate endogenous NPC upregulation 48
Figure 3.6: NPC nuclear rim intensity increases in neurons differentiated using dual SMAD inhibition 50
Figure 3.7: NPC nuclear rim intensity increases in neurons differentiated via neurogenin2 overexpression 52
Figure 4.1: TorsinA is essential for uniform NPC distribution but not upregulation of NPC biogenesis 72
Figure 4.2: Comparison of WT and torsinA-KO neuronal NPC spatial organization and nuclear morphology 75
Figure 4.3: TorsinA-KO neurons exhibit deficient recruitment of transport components and abnormal protein transport 76
Figure 4.4: TorsinA-KO neurons exhibit perinuclear PolyA+ RNA puncta 78
Figure 4.5: Neurons homozygously harboring the disease-relevant ΔE mutation exhibit abnormal clusters 79
Figure 4.6: Setting up NPC pulse-chase using neurons harboring HaloTag-Nup107 allele 80
Figure 4.7: Sites of NPC biogenesis are abnormal in torsinA-KO neurons 81
Figure 4.8: NPC spatial distribution analysis from pulse-chase study 82
Figure 4.9: NE blebs spatially and temporally coincide with NPC biogenesis 83
Figure 4.10: Bleb-associated pores are narrow and exhibit nucleoplasmic central plugs 85
Figure 4.11: NE blebs resolve as neurons continue to mature 87
Figure 4.12: NPC assembly completes following NE bleb resolution 88
Figure 4.13: Nup358 is recruited to persisting NPC clusters in DIV18 torsinA-KO neurons 90
Figure 4.14: Summary of the effects of torsinA loss on NPC spatial organization and dynamics 91
Figure 5.1: Validation of tetO-Tor1a system 103
Figure 5.2: Doxycycline treatment does not induce torsinA expression in maturing primary neurons 104
Figure 5.3: Loss of torsinA exclusively during neuronal maturation causes abnormal NPC clustering 106
Figure 5.4: Removal of doxycycline in mature primary neurons is not sufficient to knock down torsinA expression 107

Abstract

Nuclear pore complexes (NPCs) are large multiprotein assemblies essential for macromolecular transport between the nucleus and cytosol. Mutations in NPC components cause early onset neurological disorders, and NPC defects are implicated in several nervous system diseases including DYT-TOR1A dystonia (DYT1), a neurodevelopmental movement disorder caused by a loss-of-function mutation in the AAA+ protein torsinA. Yet, little is known about NPC biogenesis and dynamics, and the biological function of torsinA and the molecular defects underlying DYT1 dystonia remain largely unknown. Using super-resolution microscopy, we observe a striking upregulation in NPC density in maturing mouse primary neurons, identifying neuronal maturation as a novel, physiological context of NPC biogenesis. While NPCs are uniformly distributed in wild-type (WT) neurons, torsinA-knockout (KO) neurons develop severe clusters of NPCs. In contrast to the drastic difference in distribution between WT and torsinA-KO neurons, NPC density is normal in torsinA-KO neurons, suggesting that torsinA is essential for NPC spatial organization, but not total number. To elucidate the dynamics of NPC formation and localization, we developed a HaloTag-Nup107 mouse line and conducted pulse-chase studies of existing and newly-formed NPCs. Abnormal clusters arise in torsinA-KO neurons due to aberrant localization of nascent NPCs, indicating that torsinA is a novel determinant of sites of neuronal NPC biogenesis. Scanning transmission electron microscopy tomography reveals that mislocalized NPCs in torsinA-KO neurons spatially correlate with abnormal blebbing of the nuclear envelope (NE). These findings are consistent with a model in which absence of torsinA causes continued

budding of the inner nuclear membrane at sites of new NPC formation, resulting in NE blebs and stalling NPC assembly. Interestingly, while NPC clusters persist, NE blebs are transient, allowing NPC assembly to resume in mature neurons. Collectively, our work highlights the significance of torsinA function during a discrete developmental window and advances the understanding of fundamental mechanisms underlying NPC biogenesis and spatial organization.

Chapter 1 Introduction

1.1 The Nuclear Envelope and Nuclear Pore Complexes

1.1.1 Nuclear pore complex architecture

The nuclear pore complex (NPCs) is a large complex of approximately 120MDa in molecular weight[1–3]. NPCs serve as the gateway between the nucleus and the cytoplasm, facilitating nucleocytosolic transport of proteins and RNA[4]. The mammalian NPC is composed of about 1000 copies of ~30 protein components termed nucleoporins that are arranged into an 8-fold symmetrical structure[5]. Three stacked rings form the scaffold structure of the NPC: the nuclear ring (NR), inner ring (IR), and the cytoplasmic ring (CR) (Figure 1.1). These rings are intricately assembled from multiple subcomplexes and form the central pore channel of the NPC through which cargo is transported. A well-studied example of a subcomplex is the Y-complex, which contains 10 Nups including Nup107[1]. Although the CR and NR rings are mostly symmetric, some asymmetry exists in the stoichiometry of the components as well as their binding partners, giving rise to asymmetrical angles where the inner nuclear membrane (INM) and the outer nuclear membrane (ONM) fuse[5]. Three transmembrane nucleoporins are found in the vertebrate NPC and interact with the scaffold Nups: Pom121, Nup210 (also known as GP210), and Ndc1. Ndc1 is the only transmembrane Nup that is conserved across eukaryotes and appears to coordinate a hub to mediate the interaction between the NPC scaffold and the nuclear membrane[5]. Nup210 is a single transmembrane protein with a large luminal domain and inserts across the nuclear membrane, interacting with Ndc1 and IR components. The IR is important for the NPC permeability barrier

and contains Phe-Gly (FG)-repeat-containing Nups (FG-Nups) such as Nup98, which can interact with cargo and facilitate transport through the pore channel[6,7]. The nuclear basket, containing Nup153, interacts with the NR, and cytoplasmic filament components, including Nup358, interact with the CR[2]. Recent advances in electron microscopy and *in situ* structural modeling have revealed an almost complete structure of the scaffold rings. However, the exact structure of these non-scaffold components as well as the FG-Nups remain unclear. Additionally, cell type-specific differences in NPC structure and any associated variability in NPC assembly and function have yet to be examined in detail.

1.1.2 Function of the nuclear pore complex

NPCs allow molecules to cross the nuclear envelope via passive diffusion and facilitated transport. The disordered FG domains of the IR components form a permeability barrier that allows passive transport of molecules smaller than ~5nm and below ~60kDa[2,8,9]. Facilitated transport depends on nuclear transport receptors (NTRs) and is usually coupled to Ran (Ras-related nuclear protein)-GTP hydrolysis[10–15]. The compartmentalization and maintenance of the Ran gradient is critical for active NPC-mediated transport[13,15]. The Ran guanine-nucleotide exchange factor RCC1 is a chromatin binding protein that localizes in the nucleus, resulting in a high nuclear Ran-GTP concentration[12,16]. Conversely, Ran-GDP is prevalent in the cytoplasm since the Ran GTPase-activating proteins RanGAP1 and RanBP1 are cytoplasmic[15]. In the cytoplasm, importin-α recognizes cargo expressing a nuclear localization signal (NLS) and recruits importin-β to form an importin α/β-cargo complex. Importin-β interacts with Nup358 (also known as RanBP2; Ran-Binding Protein 2), which docks the cargo complex at the cytoplasmic face of the NPC[13]. Upon import through the central pore channel, the complex disassembles and cargo is released[17]. Nucleoplasmic Ran-GTP binds importins and facilitates their translocation back in the cytoplasm.

RanGAP1/RanBP1-mediated GTP hydrolysis then allows importins to dissociate and start a new import cycle. Export of protein cargos expressing a nuclear export signal (NES) is dependent on an exportin such as CRM1 and Ran-GTP binding. The cargo-exportin-Ran-GTP complex dissociates after cytoplasmic translocation upon GTP hydrolysis[15].

In addition to protein transport, NPCs mediate mRNA export and thereby play a key role in regulating gene expression[18]. Most mRNAs utilize a distinct mRNA export factor, NXF1, and export is dependent on interactions with FG-Nups[19] and cytoplasmic filament components such as Nup214 and Nup358[20]. NPCs may facilitate mRNA export by coordinating with RNA transcription and processing[18]. The transcription and export complex 2 (TREX-2) localizes to the NPCs in a nuclear basket-dependent manner[21]. TREX-2 recruits Mediator to bridge mRNA transcription and export[21,22]. TREX-2 association with NXF1 greatly increases NXF1's mRNA binding affinity[23], likely allowing assembly of a transport-competent mRNP granule at the nuclear basket of NPCs.

Emerging evidence suggests that NPCs impact gene regulation independently of nucleocytoplasmic transport by spatially organizing chromatin. Early electron microscopy studies clearly show that regions near NPCs exclude heterochromatin[24], raising the possibility that nonrandom spatial patterning of NPCs contributes to establishment of the 3D genome architecture. Recent reports demonstrate that several nucleoporins including Nup98[25,26] and Nup153[27,28] interact with chromatin modifiers or directly with the chromatin, and that perturbations to these proteins result in changes in gene expression profiles. Whether these interactions indeed occur at the NPC or are functions of non-NPC pools of individual nucleoporins remains a key question, along with how NPC localization impacts gene expression. The latter is a challenging question due to

limitations in the current understanding of NPC organization and would be best studied in a system in which NPC distribution is altered without impacting nucleoporin protein levels.

1.1.3 Spatial distribution of nuclear pore complexes

NPCs in mammalian cells appear to exist in clusters (activated lymphocytes) or exhibit short-range patterning (HeLa cells, neurons), and hexagonal array-like NPC organization is observed in plant cells and *Xenopus* oocytes[24]. Yet, how NPC spatial organization is regulated is unknown. The most drastic NPC spatial organization phenotypes arise from deletion of nucleoporins in *Saccharomyces cerevisiae*, which exhibit severe, asymmetrical accumulation of NPCs in a single region of the nuclear periphery[29–35]. The absence of a filamentous lamin network to anchor NPCs in these yeast cells may contribute to the severity of this phenotype, as NPCs are able to redistribute across the nuclear membrane post-formation[32,34]. In mammalian cells, NPCs appear to localize along lamins[36,37], and deletion of ELYS, but not other nuclear basket NPC components (Tpr and Nup153) in mouse embryonic fibroblasts causes NPCs to be displaced from laminA and instead cluster inside large holes within the lamin network[37]. Based on these observations, lamins may associate with certain nuclear-facing Nups to maintain NPC spatial organization in mammalian cells. Whether they play an active role in determining the sites of NPC formation or merely ensure that NPCs remain stably anchored after assembly onset remains unclear, however. How NPC spatial distribution is determined, established, and maintained and why such nonrandom organization is important are also unknown.

1.1.4 Nuclear pore complex assembly

During mitosis, NPCs are disassembled into subcomplexes upon phosphorylation of several nucleoporins, lamins, and INM proteins[38–40]. Initially, NPCs form via a post-mitotic

mechanism that involves reassembly of these disassembled subcomplexes concomitantly with reformation of the nuclear envelope[41,42,40,43], which is fragmented and absorbed into the ER at the beginning of mitosis[44]. This assembly occurs in 'noncore' regions of the membrane that are in contact with the chromosomes in late anaphase, avoiding the dense spindle microtubules[40,45]. Postmitotic NPC assembly is rapid and occurs within few minutes[40,42,46]. The NR component ELYS that interacts with chromatin in anaphase recruits scaffold components and Nup153, which then allow for recruitment of transmembrane components[40]. This postmitotic assembly mechanism is distinct from that of interphase NPC assembly, which involves *de novo* formation of new NPCs into an intact double membrane[45,47] (Figure 1.2).

Interphase NPC assembly proceeds from the nuclear side, with the INM budding towards the ONM, growing vertically and laterally until INM-ONM fusion occurs and a full NPC can be assembled[45]. Interphase NPC assembly in mitotic cells is a slower process and completes over a span of hours. Intermediates of NPC formation can be observed by electron microscopy (EM); these intermediates appear like small dome-capped structures with diameters smaller than that of regular NPCs[24,48,49]. The nuclear basket component Nup153 and scaffold components such as Nup107 are present early in assembly, whereas cytoplasmic components such as Nup358 are recruited after INM-ONM fusion[45]. The INM budding and fusion steps of interphase NPC formation require extensive membrane deformation, which may be achieved by membrane-binding or -bending proteins. Pom121 is a transmembrane nucleoporin whose depletion results in inhibition of interphase NPC formation, perhaps indicating the importance of nascent NPC membrane anchoring in early assembly steps[50]. Additionally, the amphipathic helices of Nup53, Nup133, and Nup153 have been shown to be crucial for interphase, but not mitotic NPC assembly[51,52]. Reticulons may also play a role in interphase NPC assembly as they can trigger or

stabilize membrane curvature[53]. Indeed, inhibiting Rtn4 in *Xenopus* egg extracts prevents early assembly steps of NPC in interphase[54]. While the initial steps of interphase NPC assembly have recently been characterized, the subsequent steps including recruitment of the cytoplasmic components are unclear. Additionally, whether interphase NPC assembly requires a unique machinery – possibly to trigger or drive INM budding – and what factors mediate the INM-ONM fusion are unknown.

1.1.5 Regulation of NPC number

During interphase, total NPC number nearly doubles[48,50,55,56]. NPC formation accompanies the expansion of the nuclear envelope in dividing cells, however, and NPC density is not significantly increased[36,47,48,57,58]. In contrast to similarly maintained NPC density in mitotic cells, NPC density is upregulated in developing neurons, which are terminally differentiated. NPC number increases about 5-fold between embryonic day 18 (E18) and postnatal day 15 (P15), corresponding to an approximately twofold upregulation in NPC density[59]. NPC density plateaus between P15 and P50, then slightly decreases in older animals (by P180).

How NPC number is sensed and regulated is unknown. NPC number is independent of nuclear size, nuclear surface area, and DNA synthesis[56,60]. NPC number may correlate with the cellular metabolic flux and demand on nucleocytosolic transport: NPC number decreases in differentiating chick erythroblasts in which RNA synthesis is downregulated[56], and increases in phytohemagglutinin-activated lymphocytes[48]. The robust NPC density increase in developing neurons may therefore reflect a greater need for information transfer between the nuclear and cytoplasmic compartments than what is necessary in interphasic mitotic cells. This cell-type difference raises a question of whether distinct factors regulate NPC number or transport flux in lifelong interphase cells since NPCs cannot be disassembled and reassembled as in mitotic cells.

1.1.6 Nuclear pore complexes in neurons and neurological diseases

As terminally differentiated cells, neurons must regulate and maintain NPC number and function in a closed interphase nucleus. Neuronal NPCs are extremely stable: scaffold nucleoporins are some of the longest-lived proteins in the mammalian brain, with some proteins residing for over 12 months[61,62]. Neuronal NPC integrity is likely maintained by turnover of individual proteins while the core of the NPC architecture remains stable. This allows for NPC quality control in the absence of a cell cycle-associated mechanism to disassemble and reassemble NPCs. The remarkable stability of the NPC core structure underscores the importance of proper NPC formation in neurons, as aberrant NPC assembly is likely to persists long-term without an active turnover mechanism.

As highly compartmentalized cells that rely on external cues for growth and function, neurons are heavily dependent on nucleocytosolic transport. Neurodevelopmental processes such as axonal guidance, dendritic growth, and synaptogenesis are dependent on export of mRNPs for local translation[63–68]. Neuronal plasticity requires nuclear import of signaling molecules and transcription factors in response to synaptic cues[69–71]. Indeed, mutations in nucleoporins cause CNS disorders[72,73] and NPC defects have been linked to several neurological diseases[74–78], indicating that neurons may be especially susceptible to aberrant NPC function. Despite their functional importance, neuronal NPCs are poorly characterized. When NPC biogenesis occurs in neurons and whether neuron-specific factors mediate NPC formation and maintenance are unknown.

1.2 TorsinA and DYT1 Dystonia

1.2.1 DYT-TOR1A dystonia

Dystonia is a movement disorder characterized by involuntary twisting movements and abnormal posturing. DYT-TOR1A (DYT1) is a hereditary form of dystonia caused by a 3bp deletion in the *TOR1A* gene that encodes the AAA+ (ATPase associated with diverse activities) protein torsinA[79,80]. This mutation results in the deletion of a single glutamic acid residue (ΔE) near the C-terminus of torsinA[79–81]. DYT1 dystonia is dominantly inherited and exhibits incomplete penetrance, in which ~30% of ΔE mutation carriers develop symptoms[82]. Symptom onset generally occurs in childhood and early adolescence, and carriers of the ΔE mutation with no symptoms by the age of 26 are unlikely to develop DYT1[82]. This pattern of DYT1 clinical manifestation suggests the existence of a critical developmental period during which neurons are especially vulnerable to disease insult. The pathophysiology of DYT1 is unclear; current therapies involve targeting the downstream circuit dysfunction[83] rather than correcting the direct abnormalities caused by the genetic mutation.

1.2.2 TorsinA: an atypical AAA+ protein

TorsinA resides in the nuclear envelope (NE)/endoplasmic reticulum (ER) endomembrane space[84–86]. Five proteins belong to the torsin family in vertebrates (torsinA, torsinB, torsin2A, torsin3A, and torsin4A). Of these, torsinB most closely resembles torsinA, sharing 68% of the identical sequence[81]. Torsins are atypical of the canonical AAA+ family of proteins in that they lack a highly conserved arginine finger and uniquely localize to the ER and the NE[87]. The missing arginine finger is necessary for ATP hydrolysis and is instead provided by a cofactor. TorsinA and torsinB share the same cofactors: lamina associated polypeptide 1 (Lap1) at the NE or luminal domain like Lap1 (Lull1) at the ER[88–91]. The disease-causing ΔE mutation weakens torsinA-cofactor interactions necessary for ATP hydrolysis and is therefore a loss-of-function (LOF) mutation[90,91]. While most AAA+ proteins function in a homo- or heterohexameric state, the

functional state of torsinA is unknown[87]. Proposed structures include a heterohexameric ring composed of three torsinA and three cofactor proteins, a planar or stacked homohexameric ring[92], and most recently a helical tube[93]. The helical tube is the only high-resolution structure that has been published and the most promising of the speculated models. However, this work is conducted with a soluble truncated torsinA mutant lacking the N-terminus that contains a hydrophobic membrane-association domain, and future studies are needed to elucidate how this structure allows torsinA-cofactor interactions[93].

1.2.3 TorsinA molecular function

The spatiotemporal pattern of torsinA expression suggests a particular importance for torsinA function during neurodevelopment. TorsinA expression is high in neural tissue compared to other tissues[89,94] and higher in early postnatal neural development than in adulthood[95]. TorsinA function has been implicated in protein trafficking and ER stress response[96–100] and NE egress of viral particles[101] or large mRNP granules[102]. However, there is still no consensus regarding torsinA function due to conflicting reports[103,104] and differing cell types in which these experiments are carried out. Additionally, few studies are conducted in the physiologically relevant neural context, posing further challenges to understanding torsinA function and the molecular deficits that result from torsinA ΔE mutation.

Several recent studies suggest that torsinA function is essential for lipid metabolism. *Drosophila* fat body cells without dTorsin (the sole *Drosophila* torsin protein) are smaller and exhibit large lipid droplets and higher triacylglycerol (TAG) levels, suggesting dTorsin as a potential regulator of lipin, an enzyme that converts phosphatidic acid (PA) to TAG[105]. Lipin hyperactivity is observed in brain tissue of torsinA-KO embryos[106], and ultrastructural abnormalities in dTorsin-KO fat cells are rescued by modulating regulators of lipin[107]. Deletion of

torsinA or its cofactor Lap1 in hepatocytes results in abnormal secretion and even intranuclear accumulation of lipids[108], further implicating torsinA function in lipid homeostasis. It is unclear, however, whether torsinA directly regulates lipid metabolism or partakes in a different process that impacts lipid homeostasis downstream.

1.2.4 TorsinA at the nuclear envelope

Emerging evidence suggests a role for torsinA at the NE that appears to be conserved across species and is relevant to the neural tissue. An ATP hydrolysis-deficient substrate-trap form of torsinA and the torsinA-ΔE mutant accumulate at the NE[88], indicating that the NE is an active, disease-relevant site of torsinA function. A hallmark of torsinA deletion or loss of function is the emergence of abnormal NE blebs, in which aberrant INM budding results in omega-shaped outpouchings in the NE lumen[89,95,109]. These blebs are exclusively observed in post-migratory maturing neurons[109], worsening during the first week of postnatal development and resolving by adulthood in a conditional torsinA-KO DYT1 mouse model[95]. NE blebs are found in torsinA-knockout (KO) mice and mice with homozygous knock-in of the disease-causing ΔE mutation[109], supporting ΔE as a LOF mutation. Visually similar blebs are observed in yeast mutants lacking Nups[29–31], suggesting a potential connection between NE blebs and NPCs and linking torsinA function to NPC biology. Consistent with this possibility, torsinA-KO neurons in tissue and in culture exhibit mislocalized clusters containing NPC components[75], and *C. elegans* germline cells lacking the torsinA homolog OOC-5 exhibit asymmetric accumulation of nucleoporins[110]. In mitotic cells, a single torsinA deletion does not cause overt NE phenotypes, but deletion of two or more torsin paralogs results in similar NE blebs[93,107,111–113]. Immuno-gold EM studies suggest that these blebs colocalize with NPC components[111], and blocking interphase NPC assembly by knocking down Pom121 significantly decreases the frequency of these blebs[112], further supporting

a connection between NE blebs, NPCs, and torsinA. The cause for NE blebs and the mechanism of clearance are unknown. Proteins involved in quality control such as ubiquitin and chaperones, and myeloid leukemia factor 2 appear to accumulate in the blebs[111–115]. However, whether these proteins are directly relevant to NE bleb formation or clearance and how they relate to torsinA are unclear.

The developmental dependence of NE blebs in neurons and the observed cell-type differences suggests potential involvement of other torsin family proteins in modulating NE phenotypes. Of particular interest is torsinB due to its sequence similarity and shared cofactors with torsinA[81,89]. TorsinB is highly expressed in nonneuronal tissue[89,94] and its expression in neural tissue increases during postnatal development, coinciding with decreasing torsinA levels and the disappearance of NE blebs[95,116]. Double knockdown of torsinA and torsinB in neural progenitor cells results in early NE bleb emergence (i.e. in migrating neurons), and delayed or inhibited disappearance of blebs[95]. TorsinB-mediated modulation of NE blebs is bidirectional: its overexpression in a torsinA-LOF neuronal differentiation model significantly rescues the NE bleb phenotype[95]. Consistent with these molecular findings, torsinB overexpression in a torsinA-LOF mouse model rescues neuropathological and behavioral phenotypes[117]. Overall, these reports indicate that the spatiotemporal expression pattern of torsinB underlies the discrete neurodevelopmental window of the NE bleb phenotype. Furthermore, these studies highlight the existence of a critical neurodevelopmental window during which torsinA function is critical; in this period, neurons are more susceptible to torsinA dysfunction since torsinB is not able to serve a compensatory role due to its low expression.

1.2.5 TorsinA and neuronal nuclear pore complexes

Despite recent advances in NPC biology, several fundamental questions remain regarding their organization, regulation, and biogenesis. NPCs in neurons are even more poorly understood despite their emerging relevance to diseases. The NE bleb and nucleoporin cluster phenotypes observed in torsinA-KO neurons further underscore the importance of elucidating neuronal NPC biology to advance our understanding of the molecular events underlying DYT1. This dissertation seeks to identify the period of neuronal NPC biogenesis and characterize this process using quantitative microscopy approaches. The link between torsinA, abnormal nucleoporin clusters, and NE blebs are probed by combining light and electron microscopy techniques. Specifically, we address the identity of the nucleoporin clusters in torsinA-KO neurons and their spatiotemporal relationship to NE blebs. These findings delineate early molecular deficits that arise due to torsinA loss and strongly support neuronal NPC biogenesis as the event underlying the critical window of vulnerability to torsinA LOF. These studies form the foundation for future studies on fundamental regulators of NPC organization and on cellular mechanisms of DYT1.

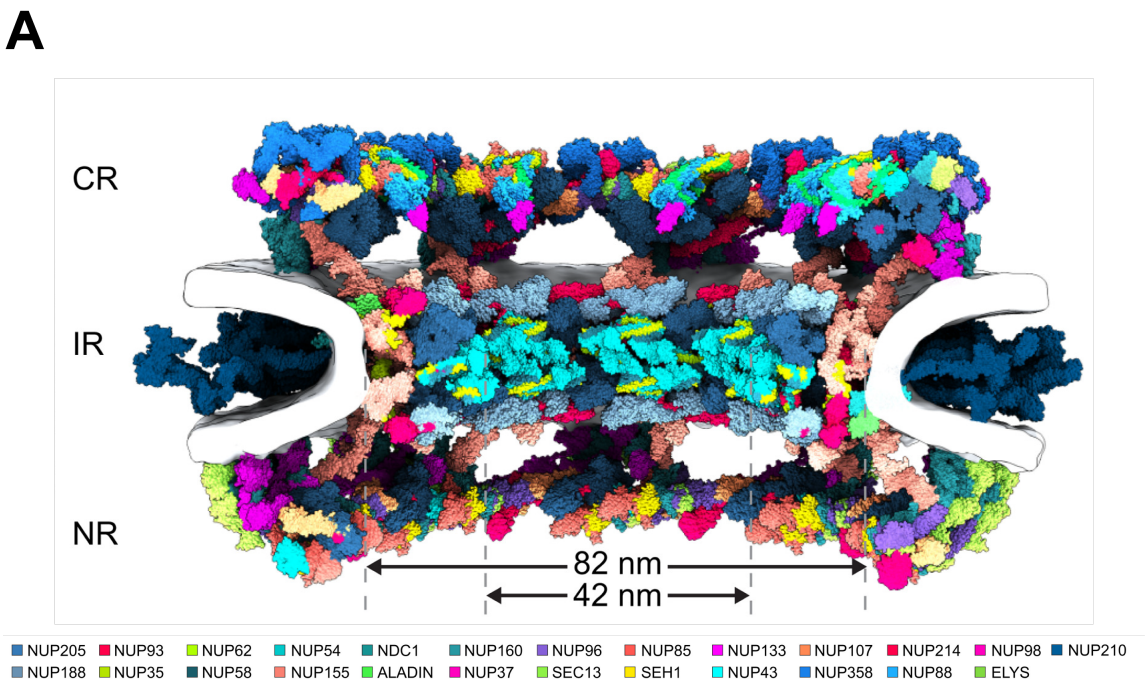


Figure 1.1: NPC architecture

Architecture of the vertebrate NPC, color coded for individual proteins. CR=cytoplasmic ring, IR=inner ring, NR=nuclear ring. Additional structural components and nucleoporins not in the structure but discussed in this dissertation are listed.

Figure adapted from Mosalaganti et al. *Science* (2022)[5]

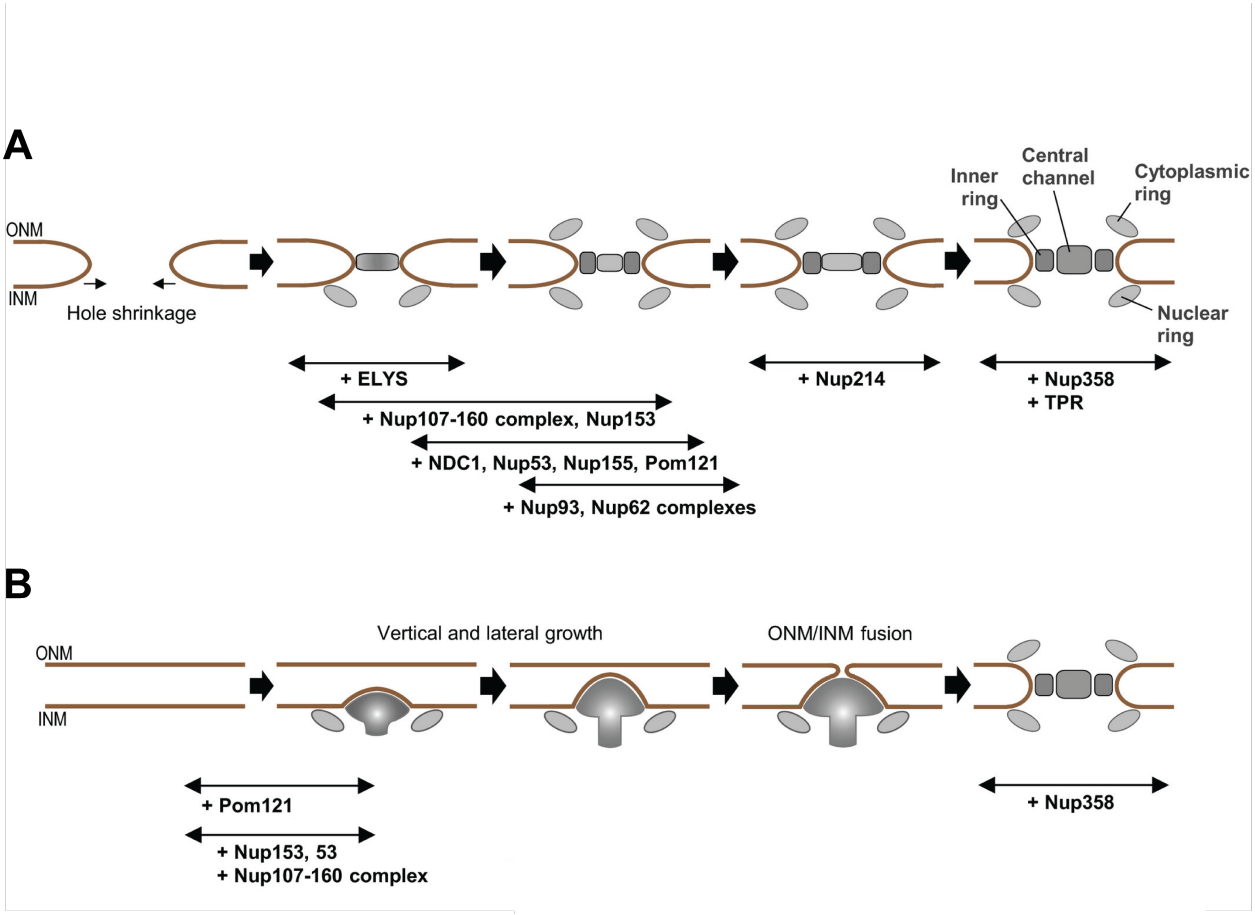


Figure 1.2: NPC assembly mechanisms

A. Post-mitotic NPC assembly mechanism. This mechanism accompanies NE reformation and occurs rapidly.
B. Interphase NPC assembly mechanism. The inner nuclear membrane (INM) starts to bud. Vertical and lateral growth leads to eventual fusion with the outer nuclear membrane (ONM). Cytoplasmic components such as Nup358 is recruited after the NPC pore channel forms.

Figure adapted from Otsuka et al. *FEBS Letters* (2018)[40]

Chapter 2 Research Design and Methods

2.1 Mouse husbandry

All animal work was approved by the University of Michigan Institutional Animal Care and Use Committee. Experimental procedures were conducted in accordance with the approved protocols and the National Institutes of Health Guide for the care and use of laboratory animals. Mice were maintained at the University of Michigan in a temperature- and light-controlled animal facility room with access to food and water *ad libitum*. *Tor1a*$^{-/-}$ and *Tor1a*$^{+/+}$ mice were derived from *Tor1a*$^{+/-}$ intercross, and *Tor1a* $^{\Delta E/\Delta E}$ mice were derived from *Tor1a*$^{+/\Delta E}$ intercross[109]. Constitutive *TetO-Tor1a* mice were derived from previously reported conditional *TetO*-expressing mice[118].

2.2 Generation of HaloTag-Nup107 mouse line

The HaloTag-Nup107 mouse line was generated using CRISPR/Extreme Genome Editing technology in partnership with Biocytogen. HaloTag with a short linker and TEV site was inserted immediately upstream of the Nup107 start codon. *Nup107*$^{KI/KI}$ mice were crossed into *Tor1a*$^{+/-}$ line[109] to generate *Nup107*$^{KI/KI}$ *Tor1a*$^{+/-}$ breeders. The following primers were used for genotyping: TGTGCTTCCGGAGAGCGGGAAG, ATAGGTTTGCCTGAAACTCCTGTGAC, and CGTGGTCGTCGAAGAAATAACCCAG. PCR cycle (95°C, 3 min; 95°C, 15 s; 70°C, 20 s (-0.7°C/c); 72°C, 1 min, 15 cycles; 98°C, 15 s; 60°C, 20 s; 72°C, 1 min, 25 cycles; 72°C, 7 min) yielded bands at 681bp for WT and 341bp for Nup107 knock-in.

2.3 Primary neuron culturing

Brains were isolated from P0 pups into ice cold, filtered dissection buffer (6.85 mM sodium chloride, 0.27mM potassium chloride, 0.0085mM sodium phosphate dibasic anhydrous, 0.011mM potassium phosphate monobasic anhydrous, 33.3mM D-glucose, 43.8mM sucrose, 0.277mM HEPES, pH 7.4). After removing the cerebellum and the meninges, cortices were dissected out, placed into a microcentrifuge tube, and cut into small pieces with dissection forceps. Cortices were incubated in 50µL papain (2mg/mL; BrainBits) and 10µL DNase I (1mg/mL; Worthington Biochemical) for 30min at 37 °C. 500µL BrainPhys Neuronal Medium (Stemcell Technologies) and 10µL additional DNase I were added, and cortices were triturated using P1000 and P200 pipet tips. Triturated cortices were centrifuged at 1000rpm for 5min. After discarding the supernatants, the pellets were triturated and centrifuged three more times until the supernatant remained clear and neuronal pellets were visible. Pelleted neurons were resuspended in BrainPhys Neuronal medium with SM1 supplement, then plated onto 35mm #1.5 glass-bottom dishes (MatTek Life Sciences) or 12mm circular #1.5 coverslips (Neuvitro) coated with polyethylenimine (100 µg/ml; Polysciences). Neurons were incubated in 5% CO2 at 37 °C, with half media change every four days. Neurons derived from one animal were plated on several coverslips such that cells from a single biological replicate can be collected on different days for time course experiments.

For experiments to induce torsinA expression in Chapter 5, 2µg/mL doxycycline hyclate (Cayman Chemicals, #14422) was added to neuronal media and media replaced every two days.

2.4 Differentiation of induced pluripotent stem cells

Induced pluripotent stem cells (iPSCs) were differentiated to neurons using the dual SMAD inhibition method[1] or the neurogenin-2 expression method[119,120] as previously described.

2.5 Western blot

Brains from P0 mouse pups were isolated into ice cold, filtered dissection buffer as with primary neuron isolation. Dissected cortices were placed into a microcentrifuge tube containing 100µL lysis buffer (RIPA (ThermoFisher; #89900) with cOmplete Mini Protease Inhibitor Cocktail (Roche; #11836153001)) and homogenized using a plastic plunger followed by pipetting with a P200 pipet tip. Samples were spun down at 15,000 g and supernatants were collected. Pierce BCA protein assay (ThermoFisher; #23227) was performed to determine protein concentration and lysates were normalized to 1 µg/µL with lysis buffer. Normalized lysates were mixed with sample-loading buffer (Invitrogen NP0007) containing 2-mercaptoethanol (80µL added to 920µL sample-loading buffer) and boiled for 5 min at 95°C. 7.5 µg of protein and Precision Plus Kaleidoscope protein standard (Bio-Rad #1610375) were loaded and run on 4–12% Bis-Tris gels (Invitrogen NP0323PK2). Protein was then transferred (350 mA for 1 hr at 4°C) onto a 0.22 µm PVDF membrane in transfer buffer containing 20% methanol. Membranes were blocked in 5% non-fat dry milk in TBS-T (Tris-buffered saline (TBS) with 0.1% Tween-20), washed once in TBS-T, and incubated overnight at 4°C with primary antibodies. The next day, membranes were washed three times with TBS-T, incubated 1h at room temperature in secondary antibodies, then imaged.

For HaloTag-Nup107 validation in Chapter 3, membranes were cut horizontally at the 75kDa mark. Top half was probed with anti-Nup107 (1:1000; ab236634) and HaloTag (1:500; Promega G9211). Bottom half was probed with anti-GAPDH (1:1000, MAB374) and anti-β-actin (1:1000, Cell Signaling 4967). Donkey anti-mouse 680 and donkey anti-rabbit 800 IR secondary antibodies were used at 1:10,000 dilution in 1:1 mixture of TBS-T and Intercept (TBS) Blocking

buffer (LICOR 927-60000) containing 0.01% Tween-20. Membranes were imaged using Odyssey CLx.

For experiments in Chapter 5, membranes were cut at the 50kDa mark and probed for anti-torsinA (bottom membrane; Abcam, ab34540; 1:10,000) and rabbit anti-calnexin (top membrane; Enzo Life Sciences, SPA-860; 1:20,000) primary antibodies. The secondary antibody was an HRP-conjugated anti-rabbit antibody (Cell Signaling Technology, 7074; 1:20,000). Bands were visualized using chemiluminescent substrate and exposure to x-ray film.

2.6 qPCR of torsinA transcripts

Primary neurons were grown in 6-well plates. RNA was isolated using the RNeasy Mini Kit (QIAgen) or the Direct-zol RNA Miniprep Kit (Zymo Research). cDNA was reverse transcribed from 400-500ng of RNA with the iScript kit (Bio-Rad). Quantitative PCR was then performed using Power SYBR Green (Applied Biosystems) with primers complementary to mouse *Tor1a* (CTCATTGACCGGAACCTCATAG, GTCATCTCTTCCGCTACCTTG) and *ACTB (*GCAAGCAGGAGTACGATGAGT, AGGGTGTAAAACGCAGCTCAG).

2.7 Light microscopy

2.7.1 Immunofluorescene labeling for confocal and structured illumination microscopy

Neurons plated on coverslips were rinsed with sterile Hank's Balanced Salt Solution (HBSS) and fixed for 10min with pre-warmed 4% paraformaldehyde (PFA) (Electron Microscopy Sciences) in phosphate buffered saline (PBS). Fixed neurons were rinsed three times with PBS and permeabilized in 0.1% Triton X-100 (Millipore Sigma) in PBS for 10min. Neurons were then incubated in blocking buffer containing 5% bovine serium albumin (BSA) and 5% Normal Goat Serum (Jackson ImmunoResearch) for 30min, and labeled with primary antibodies diluted in PBS

containing 0.1% normal goat serum overnight in 4 °C. The following day, neurons were washed three times in PBS, stained with secondary antibody for one hour, and washed three times with PBS. DNA was stained using Hoechst 33342 (1:10000 in PBS) for 5 minutes. Cells were washed twice with PBS and mounted in ProLong gold antifade mountant (ThermoFisher) for confocal or ProLong glass antifade mountant for SIM. For timecourse experiments, coverslips of neurons derived from the same animal were fixed on different days (timepoints). Coverslips fixed on earlier timepoints were stored in PBS at 4 °C until the end of the timecourse. Once all coverslips were collected, they were stained and mounted simultaneously.

2.7.2 Sample preparation and imaging for direct stochastic optical reconstruction microscopy

Neurons were rinsed with sterile HBSS and fixed for 10min with pre-warmed 4% PFA (Electron Microscopy Sciences) in PBS. Following fixation, neurons were rinsed three times with PBS and permeabilized in 0.2% Triton X-100 (Millipore Sigma) in PBS for 5min. Neurons were then incubated in blocking buffer containing 5% BSA for 30min, and labeled with Nup210 polyclonal antibody (Bethyl laboratories A301-795A; 1:200 in PBS) for two nights at 4 °C. Neurons were washed three times in PBS and stained with goat-anti-rabbit Alexa Fluor 647 Fab Fragment (1:800; Jackson ImmunoResearch 111-607-003) for an hour, washed three times with PBS, and imaged. Imaging and processing to determine localization and correct drift were conducted as previously described (Shaw et al. Biophysical Journal 2022). Samples were imaged in a buffer containing 100mM Tris, 25mM NaCl, 10% glucose, 1% beta-mercaptoethanol, 500 µg/ml glucose oxidase (Sigma) and 80 µg/ml catalase (Sigma). Images were rendered by generating 2D histograms from localizations followed by convolution with a Gaussian for display purposes.

2.7.3 HaloTag-Nup107 labeling

For visualization of the HaloTag-Nup107 protein, neurons were incubated in media containing 50nM JF646 HaloTag ligand[121] (Promega GA1120) or JFX554 HaloTag ligand[122] (Kind gift of L. Lavis, Janelia) for 30 minutes. Excess ligands were then washed out by incubating labeled cells twice in neuronal media for >1h. Cells were then fixed and immunostained with antibodies. For pulse-chase labeling in Fig. 4, DIV3 neurons plated on glass coverslips were incubated in media containing 50nM JFX554 HaloTag ligand overnight. On DIV4, all coverslips were rinsed with Hank's balanced salt solution (HBSS), incubated in neuronal media twice for 1h each to wash out excess ligand, then rinsed again with HBSS. At least one coverslip was fixed to establish DIV4 NPC density. Remaining coverslips were incubated in conditioned neuronal media containing 50nM JF646 HaloTag ligand. Coverslips were subsequently washed and fixed on DIV6, 8, and 10. On DIV7, half of media was replaced with fresh conditioned media containing 50nM JF646. Conditioned neuronal media was generated by collecting media from excess neurons of the same age and combining 1:1 with fresh neuronal media. All rinses and media changes were done with care to ensure coverslips do not dry out. After DIV10, all fixed coverslips were immunostained with Nup153 and Alexafluor 488 to label total NPC population.

2.7.4 NLS-mCherry-NES reporter assay

NLS-mCherry-NES (pDN160) reporter (Addgene plasmid #72660[123]) was transfected into DIV7 neurons using DNA-In-Neuro Transfection Reagent (MTI Globalstem) in BrainBits transfection medium for 5.5 hours. Coverslips were then returned to BrainPhys Neuronal medium overnight. Cells were fixed at DIV8 with 4% PFA.

2.7.5 PolyA+ fluorescence in situ hybridization

DIV10 neurons cultured on circular 12mm coverslips were fixed in 4% PFA made in RNase-free PBS for 10 minutes. After fixation, coverslips were washed in RNase-free PBS twice, permeabilized in RNase-free PBS with 0.1% Triton-x100 for 15 minutes, then washed twice for 5 minutes each in 2x SSC (Saline-sodium citrate) buffer (diluted from 20x SSC buffer; Invitrogen AM9763). During fixation and washes, complete hybridization buffer containing 2µg/mL Oligo dT_{30}-Cy5 probe (custom ordered from Integrated DNA Technologies), 0.01% RNase-free BSA (Thermo Scientific #23209), 0.5mg/mL yeast tRNA, 10mM Ribonucleoside Vanadyl Complex (New England BioLabs #S1402S) in hybridization buffer containing 10% Dextran sulfate (Millipore Sigma D8906) and 20% Formamide (Invitrogen AM9342) in 2X SSC was prepared. Incubation chamber was assembled by laying a clean piece of parafilm flat on a 10cm dish and treating for RNase. Following all washes, beads of 50µL of complete hybridization buffer were pipetted on to the parafilm and each coverslip was laid cell-side facing down on the buffer. Damp kimwipes lined the walls of the 10cm dish to create a humid hybridization chamber, and the dish was covered with a lid and foil to block any light and incubated for 1.5-2 hours in 37°C. Afterwards, coverslips were washed for 15 minutes in 4x SSC, twice for 15 minutes each in 2x SSC, 5 minutes in RNase-free PBS, 10 minutes in RNase-free PBS with Hoechst to stain the nuclei, and lastly 10 minutes in RNase-free PBS. Finally, coverslips were mounted in ProLong gold antifade mountant (ThermoFisher) overnight and imaged.

2.7.6 Expansion microscopy

DIV10 neurons cultured on circular 12mm coverslips were fixed and immunostained with primary and secondary antibodies as described above. After the final wash following secondary antibody labeling, samples were incubated for 1h at room temperature in 25mM MA-NHS (methacrylic acid N-hydroxy succinimidyl ester) diluted in PBS[124] then washed three times in PBS.

Gelling chamber was assembled by covering a glass slide with a layer of parafilm and using stacks of two #1.5 square coverslips as spacers placed 8mm apart, in a setup similar to what was previously described[125]. Each coverslip was flipped onto spacers neuron-side down and the resulting chamber was gently filled with U-ExM gelling solution on ice[126] (19% sodium acrylate, 10% acrylamide, 0.1% bis-acrylamide in PBS with 0.5% TEMED and 0.5% APS added last), then incubated in a humid container for 1h at 37 °C. Afterwards, gels was carefully isolated, digested with proteinase-K as in the U-ExM protocol, and allowed to expand for 30 minutes in a 6-well dish filled with ddH_2O. Subsequently, gels were each moved to a 10cm dish, exchanged twice with fresh ddH_2O, then allowed to expand overnight at 4 °C in fresh ddH_2O. Approximately 4x expansion was estimated based on the width of the expanded gel. Fully expanded gels were cut in pieces and mounted cell-side-down on glass-bottomed 60mm dishes coated with poly-L-lysine. Gels were covered with clean ddH_2O and imaged on ECLIPSE Ti inverted laser-scanning Nikon A1 confocal microscope with a 60x Apochromat water immersion (NA 1.2) objective using NIS-Elements AR (Nikon).

2.7.7 Microscopes and image acquisition

SIM imaging was conducted on a Nikon N-SIM microscope equipped with an sCMOS camera (Flash 4.0; Hamamatsu Photonics, Japan) and LU-NV laser unit (Nikon) using a 100x Apochromat oil objective (NA 1.49). Z-stack acquisitions were centered around the flat plane of the nuclear envelope (NE) facing the adherent surface of the coverslip. 9 optical sections for dual-color imaging (Alexafluor488 and Alexafluor555 immunofluorescence labeling) and 7 optical sections for triple-color imaging (JFX554, JF646, and Alexafluor488 immunofluorescence labeling) were obtained at 200nm intervals. For reconstruction from raw data, illumination modulation contrast was set at 1 and high-resolution noise suppression was set between 0.1 and

0.8. After reconstruction, two optical slices most perfectly situated in the flat NE plane were combined into maximum intensity projection for analysis. For visualizing nucleoporin nuclear rim intensity, coverslips were imaged on ECLIPSE-Ti inverted laser-scanning Nikon A1 confocal microscope using an Apochromat Lambda 60x oil (NA 1.4, WD 0.13) objective. HaloTag-labeled neurons in Fig. 2b were imaged on an ECLIPSE-Ti2 Nikon inverted microscope equipped with a spinning-disk scan head (Yokogawa, CSU-X1) and an EM-CCD camera (iXon Ultra 888) with an Apochromat TIRF 60x oil objective (NA 1.49). All microscopes were operated with NIS-Elements AR (Nikon) and all imaging was conducted at room temperature. For presentation, images were adjusted for brightness and contrast. For experiments comparing fluorescence intensity, all adjustments were conducted using the same settings.

PolyA+ RNA FISH and NLS-mCherry-NES reporter experiments in Chapter 4 were imaged with epifluorescence using a Zeiss AxioImager M2 microscope with Apotome. All images were taken using either a 20x (Zeiss 20x/0.5 EC Plan NeoFluar) or 63x (Zeiss 63x/1.40 Oil Plan Apo) objective with apotome structured illumination. 5 μm (for primary neurons) z-stacks were taken at 63× (1 μm steps between images), and maximum intensity projections were produced. Staining, imaging, and analysis were performed in parallel for all replicates.

2.8 Electron microscopy

2.8.1 Transmission electron microscopy

Primary neurons were cultured on 35mm MatTek glass bottom dishes. For pre-fixation, cells were incubated in 1.25% glutaraldehyde in 0.05M cacodylate buffer at 37 °C for 5 minutes then 4°C overnight. Cells were post-fixed in a mixture of 1% osmium tetroxide (OsO4) and 1% potassium ferrocyanide [K4Fe(CN)6] in 0.1M cacodylate buffer. For improved contrast of the subcellular structures, the pre- and post-fixed cells were stained with 1% thiocarbohydrazide,

additional 1% OsO4, 1% uranyl acetate, and Walton's lead aspartate. Cells were dehydrated in ethanol, infiltrated in Spurr's resin, and thermally polymerized at 70°C for 48 hours. A Leica EM UC7 ultramicrotome was used to cut 70nm ultrathin serial sections and the sections were placed on 300 mesh Cu bare grids. Sections were coated with 4nm carbon by a Leica EM ACE600 high vacuum coater, observed under a JEOL JEM-1400 Plus LaB6 transmission electron microscope at 60keV high tension, and imaged by an AMT NanoSprint 12 CMOS camera.

2.8.2 Scanning transmission electron microscopy tomography

To reconstruct 3D representations of specimens, a high voltage transmission electron microscope (Titan Halo, 300kV; Thermo Fisher Scientific) was operated in scanning mode, enabling us to image thick sample sections (~750nm). The sections were cut from a resin-embedded material processed for electron microscopy as described above, and then placed on 50nm Luxel film slot grids. After the grids were glow-discharged on both sides, gold particles of different size (10nm, 20nm and 50nm) were deposited on the sample surfaces for alignment purpose. The specimen under interest was tilted from −60° to +60° every 0.5° at four evenly distributed azimuthal angle positions as previously described[127] and micrographs were collected on an annular dark field detector. Data acquisition was performed with SerialEM (version 3.6.12) at magnifications corresponding to pixel sizes in the range of 0.5nm to 2.5nm at full resolution. An iterative reconstruction procedure[127] was used to reconstruct the final volumes. Segmentation and animations were generated manually using 3dmod software (version 4.11.7; University of Colorado Boulder, Boulder, CO, USA).

2.9 Image analysis

2.9.1 NPC segmentation from dSTORM

Individual NPCs were segmented through a multi-step and fully automated process designed to identify objects of a particular size and aspect ratio while not biasing towards particles with distinct pores. First, an initial segmentation was conducted using a home-built implementation of DBSCAN[128,129], with ε=40 nm and minPts = 25 (Figure 2.1A). The size of the major and minor axes of segmented objects were then determined by tabulating the eigenvalues of the covariance of x,y points with each segment. Single pores were defined as segments with major axes between 33 and 53nm, and minor axes between 23 and 43nm (Figure 2.1B). For DBSCAN objects with major and minor axes larger than this range, we further segmented pores as follows: Images were reconstructed from points with 5nm bin sizes, then blurred with a disk-shaped filter with radii corresponding to 70nm. Local maxima were then identified in filtered images, then culled to remove maxima less than 90nm apart. Localizations acquired within 80nm of the remaining local maxima were associated as candidate particles. Candidate particles were retained if their major and minor axes met the same criteria as used in the initial DBSCAN segmentation (Figure 2.1C).

Segmented pores were aligned using algorithms described previously[130]. To speed computation and estimate errors, localizations for a randomly chosen subset (250) of segmented pores were inputted into the alignment algorithm using 100nm pixels as units, with the "scale" parameter set to 10nm (0.1 in 100nm units). The final step was accomplished with imposed 50-fold symmetry to generate an angularly symmetric super particle. The density functions were tabulated by calculating the radial distance of super-particle localizations from the center of the particle, then binning to make a histogram, using bin-widths of Δr=2.5nm and each bin was divided by the total number of localizations in the super-particle, to correct for systematic differences in imaging conditions across conditions. Histograms were further divided by the area associated with

each bin = $2\pi r\Delta r$ to obtain the normalized localization density at each radius. For each super-particle, the radius associated with the maximum localization density was estimated by fitting normalized histograms to a 2^{nd} order polynomial between 25 and 55nm, then returning the maximum of the fit. Significance between conditions was determined using a 2-tailed t-test of bootstrapped replicates through the ttest2 function in MATLAB.

Super-particles generated from WT DIV18 nuclei were used to validate the segmentation procedures used. NPCs in these nuclei can be densely distributed, leading to some particles segmented as large clusters in the initial DBSCAN segmentation. Aligned NPCs were created from single pores identified from the first DBSCAN segmentation step, additional pores identified from secondary segmentation, and the pool of all segmented pores (Figure 2.1D). The localization densities along the radial distance of these aligned NPC particles were similar, so pooled NPCs were used for DIV10 WT vs. torsinA-KO average NPC dimension comparisons in Chapter 4.

2.9.2 Autocorrelation analysis of dSTORM and SIM data

For dSTORM images, pair auto-correlations were tabulated from localizations within a user-defined mask, as described previously[128]. For SIM images, pair auto-correlations were tabulated from images with a user-defined mask, as described previously[131]. In some panels, curves are normalized to the value of the first spatial bin (corresponding to r<30nm) as normalized g(r) = 1+(g(r)-1)/(g(r<30nm)-1). In all cases, curves shown represent the average over cells with errors indicating the SEM over cell measurements.

2.9.3 Calculation of nearest neighbor distances from dSTORM segmented NPCs

The centroids from each segmented NPC were determined by averaging the x and y coordinates of all localizations in the segmented NPC particle. Nearest neighbor distances were

determined by tabulating pairwise distances between all NPC centroids with a cutoff of 1μm using the crosspairs_indicies () function in https://github.com/VeatchLab/smlm-analysis, then extracting the shortest distance associated with each NPC.

2.9.4 Determination of nucleoporin puncta localization and density from SIM data

Nuclear ROIs were traced manually in FIJI[132]. For each image, a binary mask of ROIs was generated and saved. For images with high background signal (i.e. Nup antibody-labeled images), min/max histograms were adjusted on FIJI such that Otsu thresholding excludes nonspecific background signal. MATLAB scripts were used to obtain coordinates of nucleoporin puncta. First, all masks were eroded by 15px to exclude the nuclear rim where the nuclear envelope starts to curve, then overlayed with corresponding images after Otsu-thresholding. Then, imextendedmax (extended-maxima transform) was used on individual nuclei from these images to identify peaks of nucleoporin puncta. The x-y coordinate of each peak was recorded. If the peak of a puncta spanned two or more pixels, the centroid was used as the coordinate. Puncta density was calculated by dividing the number of unique peaks by the area of the eroded nuclear ROI. Outputs from the thresholding and masking step and images of unique peaks were saved as .tif files to enable visual inspection of proper peak identification.

2.9.5 Nearest neighbor distance analysis of SIM data

The nearest neighbor distance between nucleoporin puncta and the number of puncta within a specified radius were calculated in MATLAB using the knnsearch() and rangesearch() functions, respectively.

2.9.6 Nucleoporin puncta colocalization

Colococalization of puncta was determined based on assessment of whether peaks from one channel ("query") overlay with the thresholded puncta of the other channel ("search") using a custom written function. To determine % colocalization between Nup153 and HaloTag-Nup107, an image of unique peaks from the "query" channel were overlayed with the thresholded image of the "search" channel and the % of peaks whose coordinate's pixel value in the "search" channel image is >0 was calculated. To determine the density and coordinates of new JF646 puncta in the HaloTag pulse-chase experiment, this method was adapted such that JF646 peaks that did not colocalize with JFX554 puncta were counted.

2.9.7 Nuclear rim fluorescence intensity measurement of nucleoporins

Each channel of confocal z-stack was exported as a separate .tif file. For each nucleus, the z-plane that most closely represented the middle plane of the nucleus was determined by eye and the nuclear rim was manually traced in FIJI. For nuclear rim intensity analyses of iPSC (induced pluripotent stem cell)-derived neurons in Figures 3.6 and 3.7, a segmented line selection tool was used to trace an open-ended line of 2-pixel thickness, and mean intensity was measured without conversion of these lines to ROIs. For nuclear rim intensity analyses in Figures 3.3 and in Chapter 4, a polygon selection tool was used to create a closed-contour ROI of the nucleus. Using a custom-written FIJI macro script, these ROIs were converted into 4px-wide bands containing only the nuclear periphery, which were then used to measure the fluorescence intensity of nucleoporins at the nuclear rim.

2.9.8 Nuclear-cytoplasmic ratio calculations

NLS-mCherry-NES nuclear/cytoplasmic ratios were calculated as described previously[75,133], using FIJI to calculate mean pixel density per μ^2 from 63x apotome images of a

single plane through the nucleus of individual neurons containing normal ubiquitin distribution or perinuclear ubiquitin rings. DAPI was used to outline the nucleus and Map2 or mCherry delineated the cell soma. Nuclear/cytoplasmic ratio of PolyA+ RNA FISH were also similarly calculated using FIJI. Nuclei were outlined with Hoechst and soma were outlined with the oligo dT_{30}-Cy5 FISH signal.

2.9.9 Nuclear envelope bleb analysis

TEM images were acquired such that one entire nucleus and associated NE blebs (if applicable) were visible per image. Upon imaging all coverslips, all folders and files were blinded such that genotype and neuronal age identifiers were removed. All nuclei were analyzed for 1) presence of blebs and 2) number of blebs. Number of blebs was determined by counting structures that fit the following criteria: 1) a clear bleb "neck" that connects to the inner nuclear membrane and is enveloped by the outer nuclear membrane, or 2) a membrane-bound vesicle-like structure directly adjacent to the nuclear membrane that is enveloped by the outer nuclear membrane. Note that this method of blinded quantification consistently undercounts NE blebs by excluding all structures that appear like double-membrane vesicles, which are visible portions of blebs whose connection to the inner nuclear membrane occurs on a different plane from the imaging plane. Following quantification, images were unblinded and grouped by biological replicate for processing.

2.10 Statistics

Statistical information, including n (total cells analyzed), mean, and statistical significance values, is indicated in the figures or figure legends. Data are plotted using superplots[134] when applicable. N (number of biological replicates) is represented in superplots and statistical tests

were performed on means of biological replicates. At least three biological replicates were used per experiment. Statistical tests were determined upon consultation with CSCAR (Consulting for Statistics, Computing, and Analytics Research) at the University of Michigan. Sphericity was assumed for ANOVA tests based on the Mauchly's test of sphericity, which failed to reject the null hypothesis. Statistical significance was determined with Graphpad Prism 9 using the tests indicated in each figure. Data were considered statistically significant at $*P < 0.05$, $**P < 0.01$, $***P < 0.001$ and $****P < 0.0001$.

2.11 Code availability

FIJI, MATLAB, and python scripts used to analyze and plot data are available on https://github.com/suminkim/NPC_NE_measurements.

2.12 Data availability

STEM volumes will be available on the Cell Image Library.

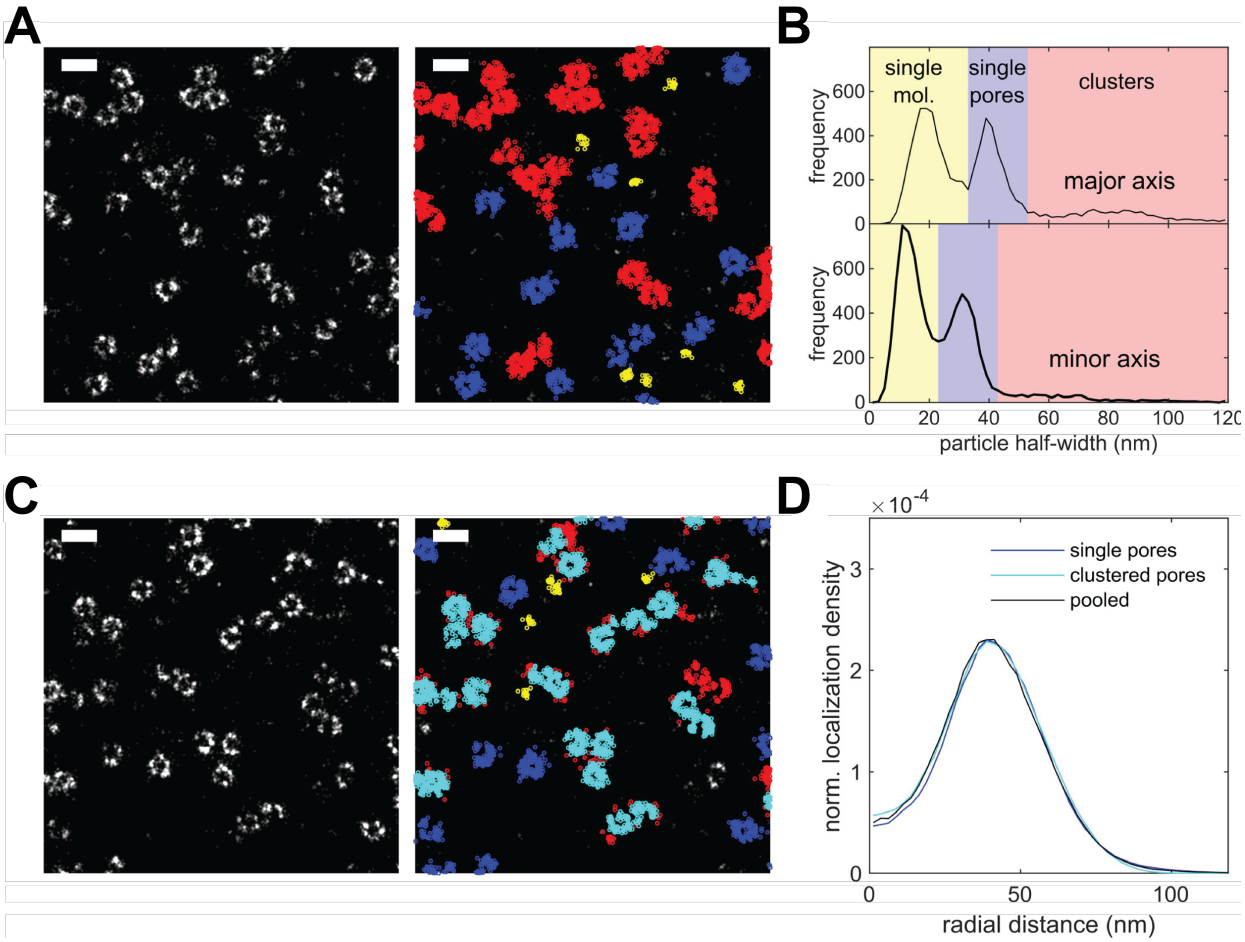


Figure 2.1: Segmentation of NPCs from dSTORM images

A) Nup210 STORM image from a DIV18 torsinA-KO neuron and DBSCAN segmentation. Small single molecules are shown in yellow, individual pores are shown in blue, and clusters of pores are shown in red, selected based on histograms shown in (B). Scale bar = 200nm.

B) Histogram of major and minor axis half-width from DBSCAN segmented particles. First peak (yellow) shows particles with axis dimensions that are too small to be pores and as such are single molecules. Second peak (blue) shows particles with dimensions in the expected range of NPC radii, and are therefore individual NPCs. Particles with major axes larger than the cutoff for individual NPCs and minor axes larger than the cutoff for single molecules are identified as multiple NPCs (red).

C) Nup210 STORM image from a DIV18 WT neuron and DBSCAN segmentation followed by filtering segmentation to identify individual pores within clusters ("clustered pores"). Clustered pores are shown in cyan, overlaid on top of the red clustering segmentation. Particles in clusters that were not selected in the filter segmentation step (particles labeled with red only) were discarded for particle averaging.

D) Plot showing the localization density along the radii of averaged individual pores (based on (A)), clustered pores (based on (C)), and pool of all pores.

Chapter 3 Nuclear Pore Complex Biogenesis is Upregulated during Neuronal Maturation

Parts of this chapter are published in a preprinted manuscript (doi.org/10.1101/2023.04.26.538491).

3.1 Abstract

As lifelong interphase cells, neurons face an array of unique challenges. A key challenge is regulating nuclear pore complex (NPC) biogenesis and localization, the mechanisms of which are largely unknown. Processes critical for neural function, such as synaptogenesis and response to neuronal activity, are dependent on NPC-mediated nucleocytoplasmic transport, and abnormal NPC distribution and function are linked to several neurological diseases, suggesting a particular importance of NPCs in neurons. However, the biogenesis and dynamics of neuronal NPCs remain poorly understood. Here, we identify neuronal maturation as a novel window of active NPC biogenesis. By visualizing NPCs in developing cultured mouse primary cortical neurons using structured illumination microscopy, we find that new NPCs steadily form over approximately two weeks of neuronal maturation, resulting in a twofold increase in total NPC density. Notably, the timescale and degree of NPC upregulation in neurons exceeds previously characterized NPC biogenesis in cells that undergo division. We additionally find that NPCs appear upregulated in maturing neurons derived from induced pluripotent stem cells (iPSCs). Our findings identify a defined physiological neurodevelopmental window of NPC biogenesis that is likely triggered and sustained to meet the metabolic demands of developing neurons.

3.2 Introduction

Nuclear pore complexes (NPCs) are large, evolutionarily conserved structures that serve as the gateway between the nucleus and cytoplasm, allowing passive diffusion of small molecules and facilitating nucleocytosolic transport of proteins and RNA[2,3]. Regulation of NPC biogenesis and function is critical for coordinating information transfer between the nucleus and cytoplasm, allowing cells to dynamically respond to internal and external cues. Neurons are heavily dependent on NPC function; neuronal plasticity requires transport of signaling molecules and transcription factors[69,71,135,136] and mRNA export for local translation is essential for several neurodevelopmental processes[63,65,66,68,137]. Accordingly, NPC defects are present in several nervous system diseases[74–78] and mutations in nucleoporins cause early-onset neurological illness[72,73].

Neurons face a considerable challenge in maintaining proper nuclear function throughout their lifetime. Mitotic cells disassemble and recreate the nucleus with each division, while neurons must manage nuclear pore number and localization within a closed interphase nucleus. Neuronal NPCs exhibit minimal turnover and nucleoporins (Nups) that constitute the NPC are among the longest-lived proteins[61,62], underscoring the unique challenge neurons face in regulating NPC formation and function. Despite the biological and clinical importance of these events, little is understood about neuronal NPC biogenesis. Furthermore, mechanisms underlying NPC number, organization, and dynamics in both neuronal and non-neuronal systems remain elusive.

Mammalian cells utilize two major NPC assembly mechanisms: postmitotic assembly as the fragmented nuclear envelope (NE) reforms following mitosis, and interphase assembly in which NPCs form into an intact nuclear membrane[40]. Interphase NPC assembly proceeds from the nucleoplasmic side and involves budding of the inner nuclear membrane[45], requiring nuclear

import of early, nuclear-facing nucleoporins through existing NPCs formed via the postmitotic assembly mechanism[52]. Factors that trigger NPC formation are unknown, and NPC number is independent of DNA content, nuclear surface area, and nuclear volume[56]. Rather, NPC number may be dependent on transcriptional activity and demand on NPC transport flux[56].

Studies on neuronal NPC biology are extremely limited, in part because neurons are terminally differentiated, unproliferating cells that are challenging to obtain and maintain. Recent advances in *in vitro* neuronal culturing methods significantly lower the barrier for investigating neuronal cell biology in physiological contexts. The rodent primary neuron culture system enables studies on cell-autonomous processes occurring in developing neurons derived from embryonic or postnatal day 0 (P0) pups. The first two weeks of maturing mouse primary cortical neurons are accompanied by increase in proteins critical for synaptogenesis and dendrite development[138], signifying events that may require upregulated nucleocytosolic transport flux. Beyond the scope of rodent neurons, *in vitro* development of neurons derived from human embryonic stem cells (hESCs) or induced pluripotent stem cells (iPSCs) can be achieved by either a dual SMAD inhibition protocol in which neurons differentiate following neural stem cell rosette formation[139] or by expressing neurogenenin-2 for rapid differentiation[119].

Here, we provide an in-depth quantitative analysis of NPC biogenesis in developing cortical mouse primary neurons using confocal and super-resolution microscopy. We show that neuronal maturation is accompanied by a robust, steady upregulation in NPC formation that results in an approximately twofold increase in NPC density in the first three weeks of *in vitro* development. We generate and validate a HaloTag-Nup107 mouse line to probe endogenous NPCs in the context of neuronal maturation. We find that the HaloTag-Nup107 fusion does not exert any toxicity to the animals or the neurons, and that HaloTag-labeled NPCs exhibit excellent

colocalization with antibody-stained Nup153. Super-resolution imaging of single NPCs with HaloTag-Nup107 labeling reflects the same twofold NPC density increase in maturing neurons observed with antibody staining, establishing this new mouse model as a valuable tool in studying endogenous NPC biology. Upregulated NPC formation appears to be a shared feature of maturing neurons across species, since neurons derived from iPSCs using two different methods similarly demonstrate increased nucleoporin intensity over time. Our findings establish neuronal maturation as a novel context of NPC biogenesis in developing neurons, one that exceeds the degree of upregulation and timescale observed in non-neuronal mitotic cells.

3.3 Results

3.3.1 NPC density increases during neuronal maturation

To explore neuronal NPC biogenesis, we used structured illumination microscopy (SIM) to characterize NPC density in cortical primary neurons. Primary neurons from P0 pups were cultured and fixed at days in vitro (DIV) 4, 6, 8, 10, 14, 18, and 24 and labeled with Nup153 and Nup98 antibodies. In immature neurons[138] (i.e., DIV4 and DIV6), both nucleoporins (Nups) appeared sparse. As the neurons matured, the density of Nup153 and Nup98 puncta increased, culminating in a dense yet even distribution of NPCs across the nuclear envelope (DIV18 and DIV24; Figure 3.1A). We developed an image analysis pipeline to identify and localize the peaks of Nup puncta to quantitatively measure Nup density and distances (Figure 3.1B). Peaks from Nup153 and 98 puncta appeared to mostly overlap, suggesting that the antibodies used in this approach labeled NPCs rather than non-NPC pools of nucleoporins. The density of Nup153 and Nup98 puncta gradually increased over two weeks of neuronal maturation from approximately 7 puncta/μm^2 at DIV4 to 14 puncta/μm^2 at DIV24 (Figure 3.1C, D). Nuclear area did not change significantly during this time (Figure 3.2A), indicating that the increased Nup density is due to *de*

novo formation of new NPCs. We used coordinates of identified peaks to calculate the nearest neighbor distance for each punctum. As expected, few puncta at any timepoint measured have a nearest neighbor within 120nm, the diameter of a single NPC[140,141] (Figure 3.2B, C). The percentage of Nup153 and Nup98 puncta with a nearest neighbor within a two-pore diameter distance (240nm) increased with time, while the percentage of puncta with a nearest neighbor far away decreased. Consistent with increasing NPC density, the proportion of Nup puncta with multiple proximal neighbors increased as neurons matured (Figure 3.2D, E). Together, these data demonstrate that NPC biogenesis is upregulated during neuronal maturation.

The acquisition of SIM images and subsequent processing time are not well suited for large-scale analysis of cultured neurons. We therefore pursued the alternative strategy of measuring nuclear rim intensity of NPC components with confocal microscopy to further explore NPC biogenesis. Consistent with our SIM data, there was an approximately twofold increase in nuclear rim intensity of Nup153 and Nup98 between DIV4 and DIV10 (Figure 3.3A-C). Additionally, we used antibodies against FG-Nups (Nups containing Phe-Gly motifs; mab414) and Nup210 (a transmembrane nucleoporin) to assess whether other Nups were similarly upregulated, as would be expected with increased NPC biogenesis. Between DIV4 and DIV10, the nuclear rim intensity of mab414 and Nup210 increased twofold (Figure 3.3D-F), demonstrating upregulated density of multiple NPC components, including those spanning the nuclear basket, inner ring, and transmembrane subunits.

3.3.2 Novel HaloTag-Nup107 knock-in allele enables labeling of endogenous NPC dynamics

To dissect mechanistically how NPC clusters form, we developed a novel tool to track endogenous NPC biogenesis. We generated a knock-in mouse line in which HaloTag[142] is fused to the N-terminus of endogenous Nup107 (Figure 3.4A). Nup107 was chosen as prior literature

demonstrates that N-terminally tagged 3x EGFP-Nup107 maintains normal localization and dynamics[57,143]. We validated this HaloTag-Nup107 (Halo-Nup107) knock-in mouse line using the JF646 HaloTag ligand to label endogenous Nup107 protein in DIV10 cortical primary neurons (Figure 3.4B). We observed a gene dose-dependent increase in fluorescence intensity at the nuclear membrane in neurons derived from *Nup107*$^{+/+}$, *Nup107*$^{KI/+}$, *Nup107*$^{KI/KI}$ mice, indicating that the fusion protein is incorporated into nuclear pores. We further assessed the knock-in by probing the levels of the Nup107-HaloTag fusion protein in P0 cortical lysates. We observed a single band corresponding to Nup107 in *Nup107*$^{+/+}$ lysate, two bands representing both Nup107 and HaloTag-Nup107 in *Nup107*$^{KI/+}$ lysate, and a single band indicative of HaloTag-Nup107 in *Nup107*$^{KI/KI}$ lysate (Figure 3.4C). *Nup107*$^{KI/KI}$ mice were indistinguishable from their WT littermate controls and we observed the expected Mendelian ratios of genotypes from *Nup107*$^{KI/+}$ intercross (Figure 3.4D), indicating that the HaloTag did not exert any toxicity.

We examined the localization and density of HaloTag-Nup107 in developing neurons by labeling DIV4, 10, and 18 *Nup107*$^{KI/KI}$ neurons with the JFX554 HaloTag ligand and staining them with Nup153 antibody (Figure 3.5A). SIM imaging of single NPCs demonstrated an approximately twofold increase in Nup density from DIV4 to DIV18 despite similar nuclear envelope area (Figure 3.5B-D). Nearest neighbor distances of HaloTag-Nup107 puncta decreased throughout neuronal maturation while the number of neighboring puncta within 240nm increased, reflecting the increase in density and decrease in pore-pore distances as neurons mature (Figure 3.5E, F). Overlay of Nup153 peaks with JFX554 puncta and vice versa showed a high level of colocalization (Figure 3.5G, H). These data validate the HaloTag-Nup107 mouse model as a novel tool for studying endogenous NPC dynamics and confirm that maturing neurons exhibit strongly upregulated NPC biogenesis.

3.3.3 NPC increase is observed in maturing induced pluripotent stem cell-derived neurons

To assess whether NPC upregulation during neuronal maturation is also observed in a non-rodent model, we examined NPC density in neurons derived from induced pluripotent stem cells (iPSCs). We first used the dual SMAD inhibition protocol to differentiate iPSCs to cortical neurons via neural progenitor cell rosette formation[139,144]. This protocol results in an almost pure population of cortical neural progenitor cells by Day 15 of differentiation and emergence of first postmitotic cortical deep layer neurons around Day 20[144] (Figure 3.6A). To visualize changes in NPC density, we fixed cells at Days 4, 7, 21, and 34 of differentiation and probed the cells with Nup153 and Nup358 antibodies (Figure 3.6B). In progenitor cells (Days 4 and 7), the nuclear rim intensity of these nucleoporins was generally dim, with Day 7 cells exhibiting lower nucleoporin fluorescence intensity than Day 4 cells. Nucleoporins visibly started to concentrate at the nuclear membrane in Day 21 cells, and nucleoporin intensity was highest in Day 34 cells. Overall, there was a trend of increasing intensities for both Nup153 and Nup358 during neurogenesis and maturation (Figure 3.6C, D).

To explore an alternative method that results in a purer population of functional neurons in a shorter timeframe, we used iPSCs in which differentiation is induced by neurogenin-2 (Ngn2) overexpression upon doxycycline addition. In this system, Map2-positive neurons emerge within one week and synapse formation is observed in the second week following doxycycline induction[119]. We fixed cells at Days 2, 6, and 10 upon doxycycline induction and again found an increasing trend of nuclear rim intensity of Nup153 and Nup358 (Figure 3.7A-C). Nup153 localization in early timepoints was not concentrated at the nuclear membrane, but its recruitment was visible in Day 10 neurons. Nup358 localization in both the nucleoplasm and the nuclear membrane was observed at Days 2 and 6, but clear recruitment to the nuclear membrane was

observed by Day 10. While the neurons we probed using both the dual SMAD inhibition and Ngn2 differentiation are young and still in maturation, these data hint that NPC density increase is conserved between mice and humans.

3.4 Discussion

The data presented in this chapter represent the first in-depth quantitative characterization of neuronal NPC biogenesis. We identify postnatal neuronal maturation as a window of steady, active NPC formation. We develop and characterize a new HaloTag-Nup107 mouse line to probe endogenous NPCs in primary neurons. Experiments to probe NPC biogenesis in neurons of human genetic background suggest that upregulated NPC density is not limited to rodent *in vitro* neurons but may be a common, general feature of neuronal maturation.

A tremendous challenge for post-migratory maturing neurons is meeting the large demand for protein synthesis, including mRNA transport, to supply the many proteins required to acquire characteristic neuronal phenotypes and to integrate into synaptically-connected circuits[138]. Considerable work in non-neuronal cells indicates that increasing NPC number is likely needed to support such metabolic demand[24,56,60], but similar studies of NPC biogenesis have not been performed in neurons. To our knowledge, only one previous study has assessed NPC density during neural development, using freeze-fracture EM on brains from mice at four different ages[59]. Using multiple methods, including using super resolution microscopy with both antibody-dependent and -independent endogenous labeling of Nups, we demonstrate a doubling of NPC density from DIV4 to DIV18. The magnitude of NPC density increase is remarkably similar to the *in vivo* observations reported in the aforementioned EM study[59]. The robust twofold upregulation of neuronal NPC density contrasts with interphase NPC assembly in mitotic cells, which occurs concomitantly with NE expansion and results in little to no increase in NPC density[36,47,48,57,58].

While neuronal NPC biogenesis is sustained over a period of two weeks, interphase NPC assembly in mitotic cells completes on the scale of several hours[36,45,47,48,57,145]. Protein levels are upregulated during the first twenty days of maturing primary cortical neurons, coinciding with synaptogenesis and increasing complexity in neuronal morphology[138]. Based on the data implicating a relationship between cellular activity and NPC number, neuronal NPC biogenesis likely occurs during a prolonged temporal window to accommodate an increased need for nucleocytoplasmic transport during neural development. Although NPC formation in neurons and in interphasic mitotic cells both involve a *de novo* insertion of NPCs in intact nuclear membranes[36,40,45,47,146,147], these differences in assembly timescale and the unique process of neuronal maturation raise the possibility of neuron-specific regulators of NPC biogenesis.

What triggers NPC formation? Studies from G.G. Maul and colleagues suggest that NPC number is independent of DNA content, genome copy number, nuclear surface area, and nuclear volume[24,55,56,60]. Instead, there is a correlation between NPC number and transcriptional activity[56], indicating that increased cellular transcriptional flux and nucleocytosolic transport may necessitate NPC upregulation. In dividing cells, cyclin-dependent kinases (Cdks) may be important for interphase NPC formation, as their inhibition results in fewer nascent NPCs[36]. Whether Cdks play a role in neuronal NPC biogenesis is unknown as is the mechanistic link between Cdks and NPC assembly. Beyond these observations, not much is understood regarding regulation of NPC number and function. Future studies are necessary to understand how cells sense and regulate NPC number and how increased nucleocytosolic transport flux may trigger NPC formation.

Our data suggest that increased NPC formation during neuronal maturation is not limited to the rodent primary cortical neuron system, but also occurs in *in vitro* maturing neurons of human genetic background. Our iPSC-derived neuronal studies show a trend of increasing nucleoporin

intensity at the nuclear membrane over time using two independent methods of differentiation. These data are preliminary, however, and detailed characterization of multiple nucleoporins at different stages with markers for cellular identity is needed to draw definitive conclusions. Furthermore, the neurons we imaged at Day 21 and 34 from the dual SMAD differentiation and Day 10 from the Ngn2-differentiation are still actively maturing, and future studies should include neurons at later timepoints to assess NPCs during neuronal maturation.

A major advance presented in this chapter is the generation and characterization of the HaloTag-Nup107 mouse line. While several cell lines endogenously harboring fluorescent tags fused to nucleoporins have recently been reported[148,149], no such tool exists for studying NPCs in primary cells or in tissue. We show that ubiquitous tagging of HaloTag-Nup107 does not exert any toxicity to the mice and further demonstrate proper localization and incorporation of this fusion protein in neurons. Our use of HaloTag-Nup107 primary neurons to study NPC formation represents one example of how this new system can be used to study physiological phenomena. Similar methods can be used in other cell types derived from this mouse model to study NPC biology in a variety of contexts, especially as this mouse line can be crossed with other lines. Additionally, injection of fluorogenic HaloTag ligands can be used for *in vivo* imaging of NPCs in a range of biological and disease-related contexts.

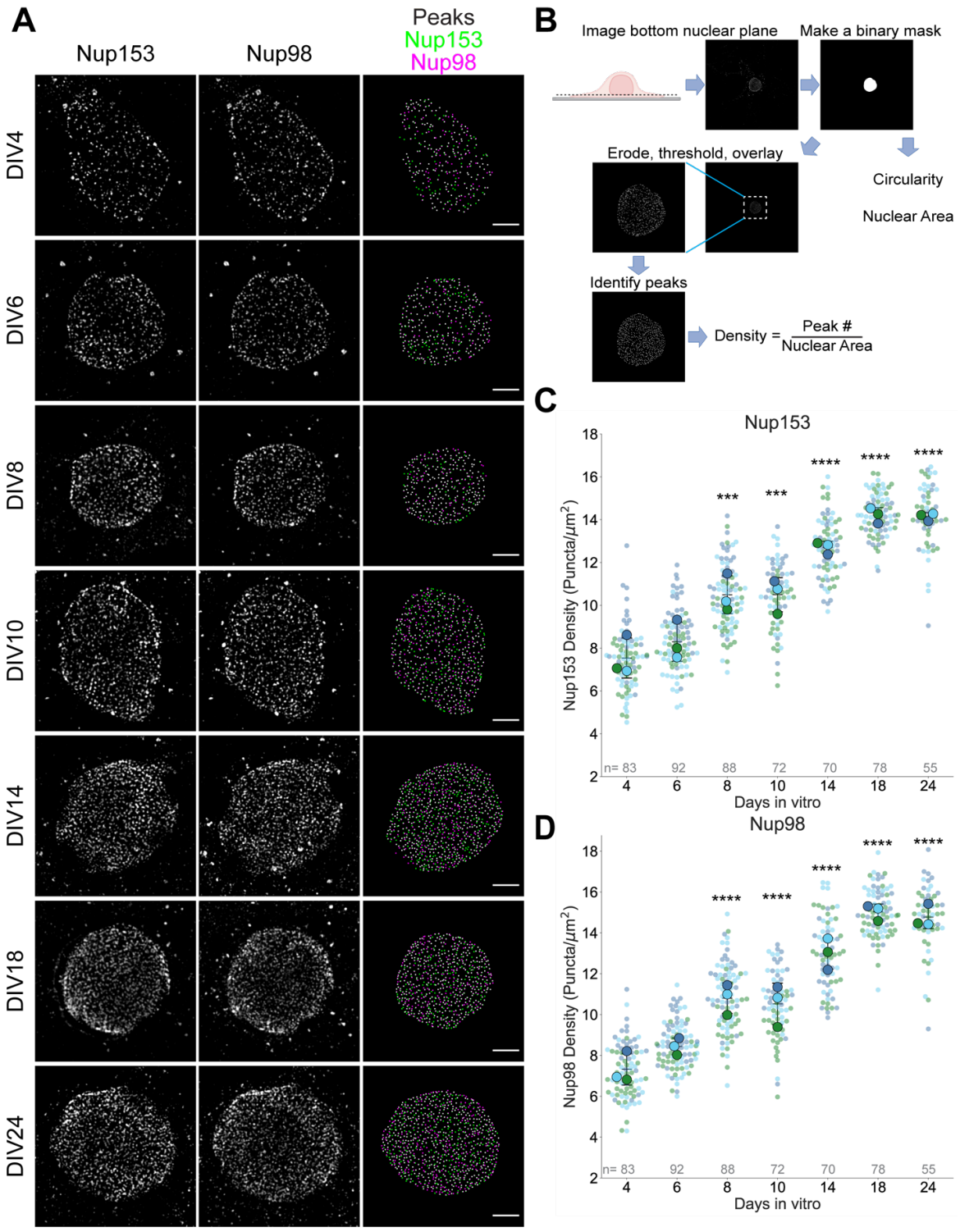


Figure 3.1: Nuclear pore complex biogenesis is upregulated during neuronal maturation

A) SIM images of primary neurons aged DIV4, 6, 8, 10, 14, 18 and 24 labeled with anti-Nup153 and anti-Nup98 antibodies. Peaks column shows peaks identified from Nup153 (green) and Nup98 (magenta) puncta. Scale bar = 2µm.

B) Schematic of image analysis pipeline. The flattest part of the nuclear envelope was imaged. Nuclear ROIs were determined by manually outlining each nucleus. ROIs were eroded to account for nuclear envelope curvature at the edge, then overlayed onto Otsu thresholded images. Local maxima were identified with extended-maxima transform and used to establish peaks corresponding to each Nup.

C) Superplots of Nup153 density (puncta/μm^2) over time in primary neurons. Plots show mean $\pm$ SD, with color coding indicative of biological replicates. Repeated measures one-way ANOVA with Dunnett's multiple comparisons test was performed, with DIV4 as the reference condition. ***P=0.0006, ****P<0.0001. Total number of analyzed nuclei are represented as "n".

D) Superplots of Nup98 density (puncta/μm^2) over time in primary neurons. Repeated measures one-way ANOVA with Dunnett's multiple comparisons test was performed, with DIV4 as the reference condition. ****P<0.0001.

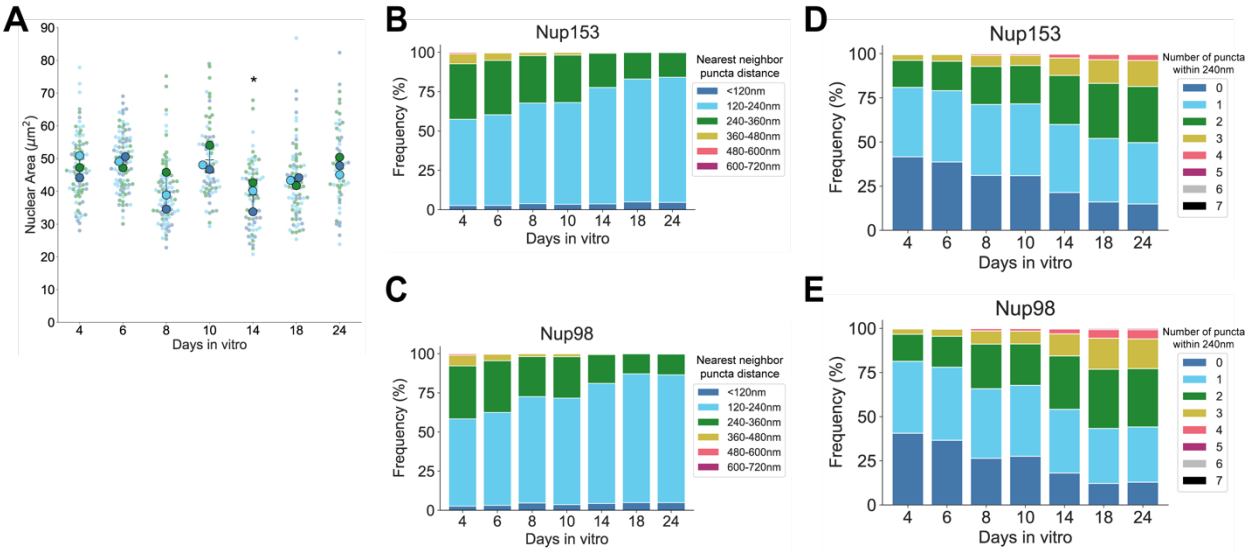


Figure 3.2: Identification and analysis of nucleoporin puncta

A) Superplots of nuclear ROI area as determined by Nup153/Nup98 staining in maturing neurons aged DIV4, 6, 8, 10, 14, 18 and 24. Plots show mean ± SD, with color coding indicative of biological replicates. Repeated measures one-way ANOVA with Dunnett's multiple comparisons test was performed, with DIV4 as the reference condition. Only DIV14 showed statistical significance; *P=0.0331.

B, C) Frequency distribution of nearest neighbor distances of Nup153 (B) and Nup98 (C) puncta. For each Nup153 and Nup98 peak, the distance to its nearest neighbor was calculated. The results from three biological replicates were combined for each timepoint.

D, E) Frequency distribution of Nup153 (D) and Nup98 (E) puncta found within two-pore diameter (240nm) distance. For each identified Nup153 and Nup98 peak, the number of neighboring puncta within a radius of 240nm was calculated. Results from three biological replicates were combined at each timepoint.

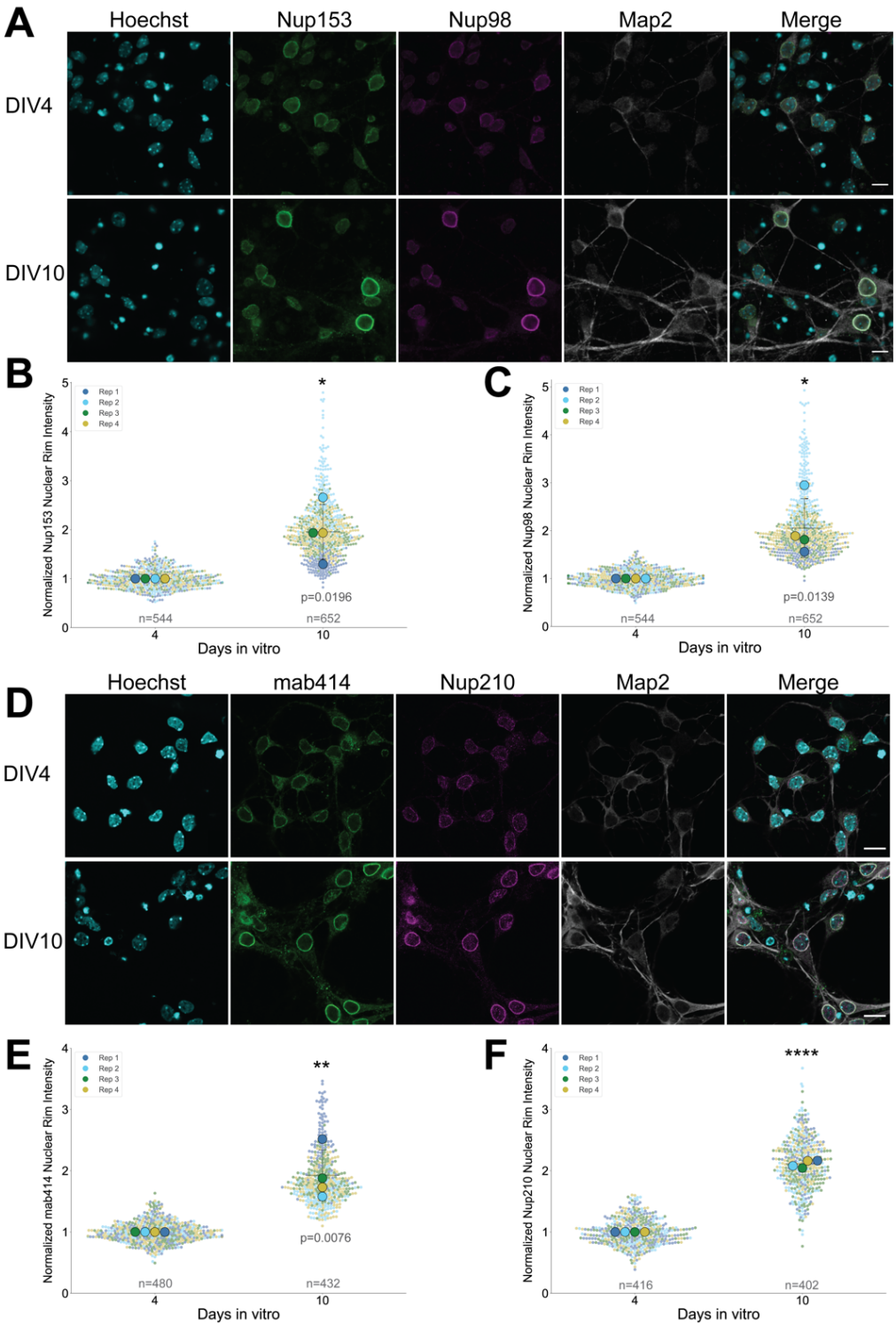


Figure 3.3: Multiple NPC components exhibit density increase during neuronal maturation

A) Confocal images of DIV4 and DIV10 primary neurons labeled with anti-Nup153 and anti-Nup98 antibodies. Scale bar = 10μm.

B, C) Normalized nuclear rim fluorescence intensity of Nup153 and Nup98 in DIV4 and DIV10 primary neurons. Plots show mean ± SD, with color coding indicative of biological replicates. P values were calculated using paired t-test.

D) Confocal images of DIV4 and DIV10 primary neurons labeled with anti-FG nucleoporin (mab414) and anti-Nup210 antibodies. Scale bar = 10μm.

E, F) Normalized nuclear rim fluorescence intensity of FG-Nups (mab414) and Nup210 in DIV4 and DIV10 primary neurons. Plots show mean ± SD, with color coding indicative of biological replicates ****P<0.0001, paired t-test.

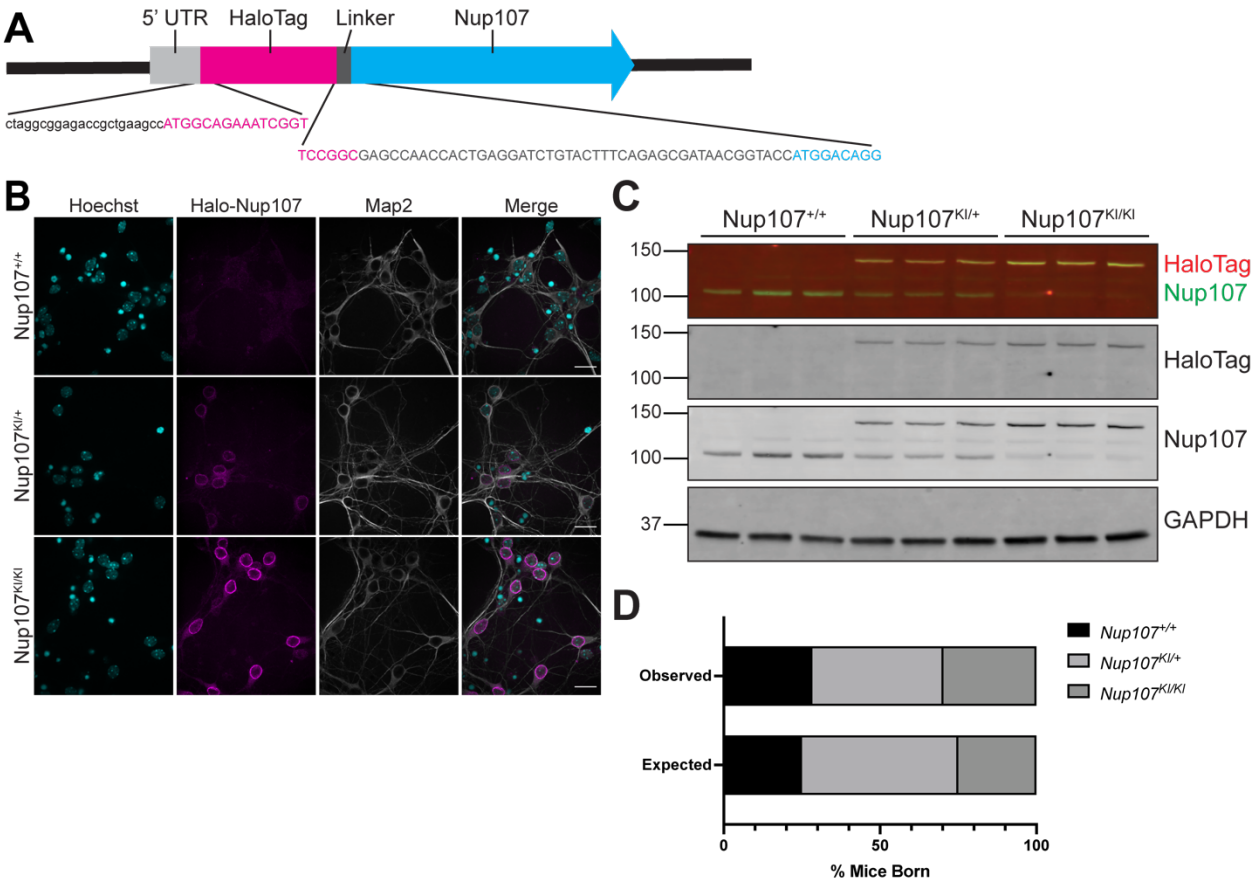


Figure 3.4: Validation of HaloTag-Nup107 mouse line

A) Schematic of HaloTag-Nup107 fusion, including 5' untranslated region (UTR, light grey), HaloTag open reading frame (magenta), flexible linker (dark grey) and Nup107 coding sequence (cyan).

B) Confocal images of DIV10 neurons derived from *Nup107*$^{+/+}$, *Nup107*$^{KI/+}$, and *Nup107*$^{KI/KI}$ mice labeled with JF646 HaloTag ligand. Scale bar = 20µm.

C) Immunoblot of P0 cortical lysates from *Nup107*$^{+/+}$, *Nup107*$^{KI/+}$, and *Nup107*$^{KI/KI}$ mice probed with anti-Nup107 and anti-HaloTag antibodies. GAPDH was blotted as a loading control. Each band represents an independent biological sample (3 animals for each genotype).

D) Distribution of genotypes in litters derived from intercrossing *Nup107*$^{KI/+}$ mice. No deviation from the expected Mendelian ratio was observed (P=0.3729, Chi-squared test). 74 pups from 9 litters were analyzed.

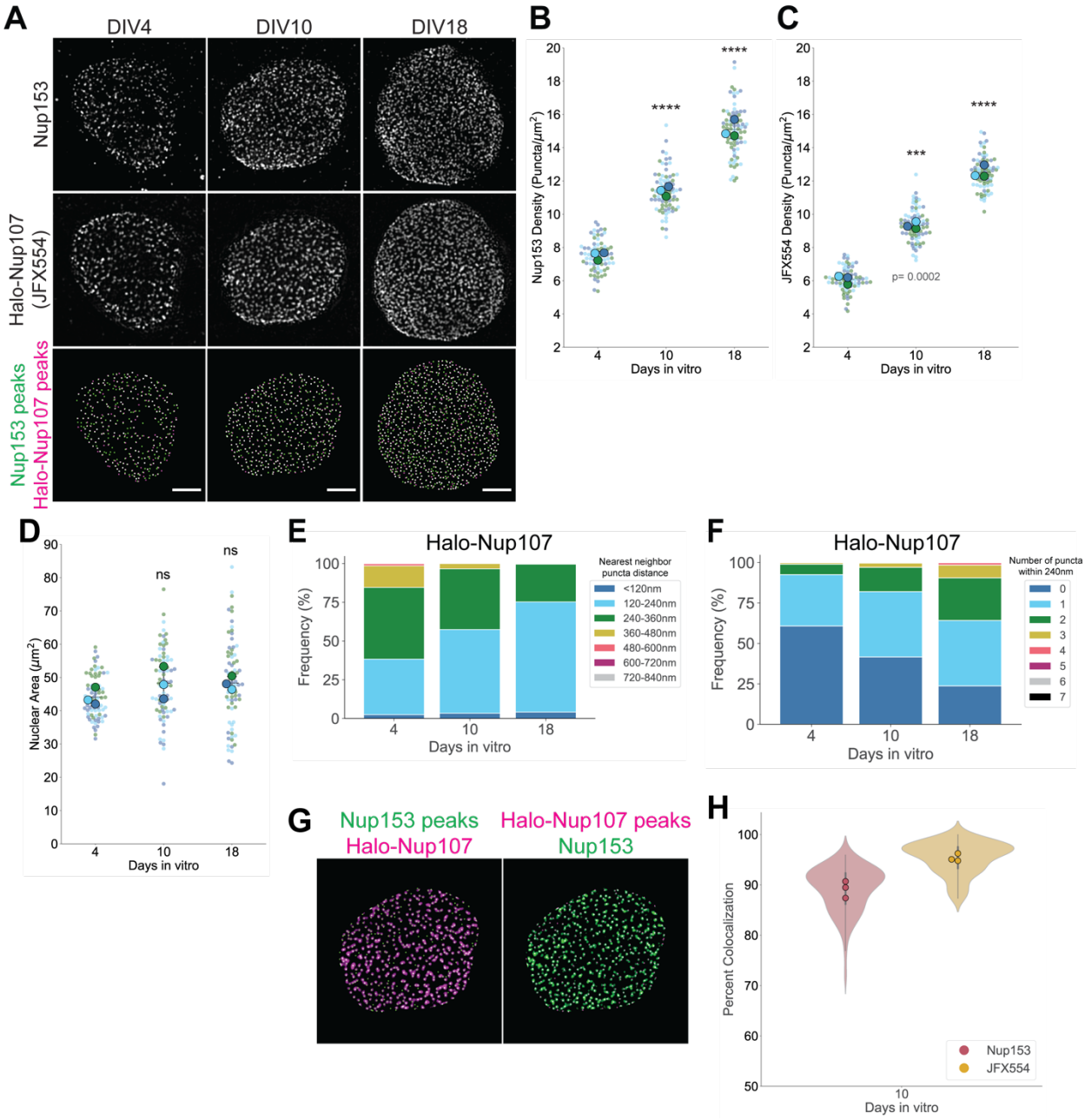


Figure 3.5: Neurons bearing a novel HaloTag-Nup107 knock-in allele demonstrate endogenous NPC upregulation

A) SIM images of *Nup107*$^{KI/KI}$ primary neurons at DIV4, 10, and 18 labeled with JFX554 HaloTag ligand and anti-Nup153 antibody. Scale bar = 2μm.

B, C) Superplots of Nup153 (B) and JFX554 (C) puncta density in primary neurons aged DIV4, 10, 18. Plots show mean ± SD, with color coding indicative of biological replicates. Repeated measures one-way ANOVA with Dunnett's multiple comparisons test was performed, with DIV4 as the reference condition; ****P<0.0001. Number of analyzed nuclei are represented as "n".

D) Superplots of nuclear ROI area from Nup153 and JFX554 SIM images. Plots show mean ± SD, with color coding indicative of biological replicates. ns, not significant; repeated measures one-way ANOVA with Dunnett's multiple comparisons test, with DIV4 as a reference condition.

E) Frequency distribution of nearest neighbor distances of JFX554 puncta. For each JFX554 peak, the distance to its nearest neighbor was calculated. Results from three biological replicates were combined.

F) Frequency distribution of JFX554 puncta within two-pore diameter (240nm) distance. For each JFX554 peak, the number of neighboring puncta within a radius of 240nm was calculated. Results from three biological replicates were combined.

G) Representative image of Nup153 and HaloTag-Nup107 colocalization in DIV10 HaloTag-Nup107 neurons. Identified Nup153 peaks are overlaid with thresholded JFX554 SIM image and vice versa.

H) Violin plot showing the percent of Nup153 and JFX554 puncta that colocalize with JFX554 and Nup153, respectively, in DIV10 neurons. Nup153 colocalization with JFX554 was measured by calculating the % of Nup153 peaks that overlap with thresholded JFX554 puncta. Conversely, JFX554 colocalization with Nup153 was measured by calculating the % of JFX554 peaks that overlap with thresholded Nup153 puncta.

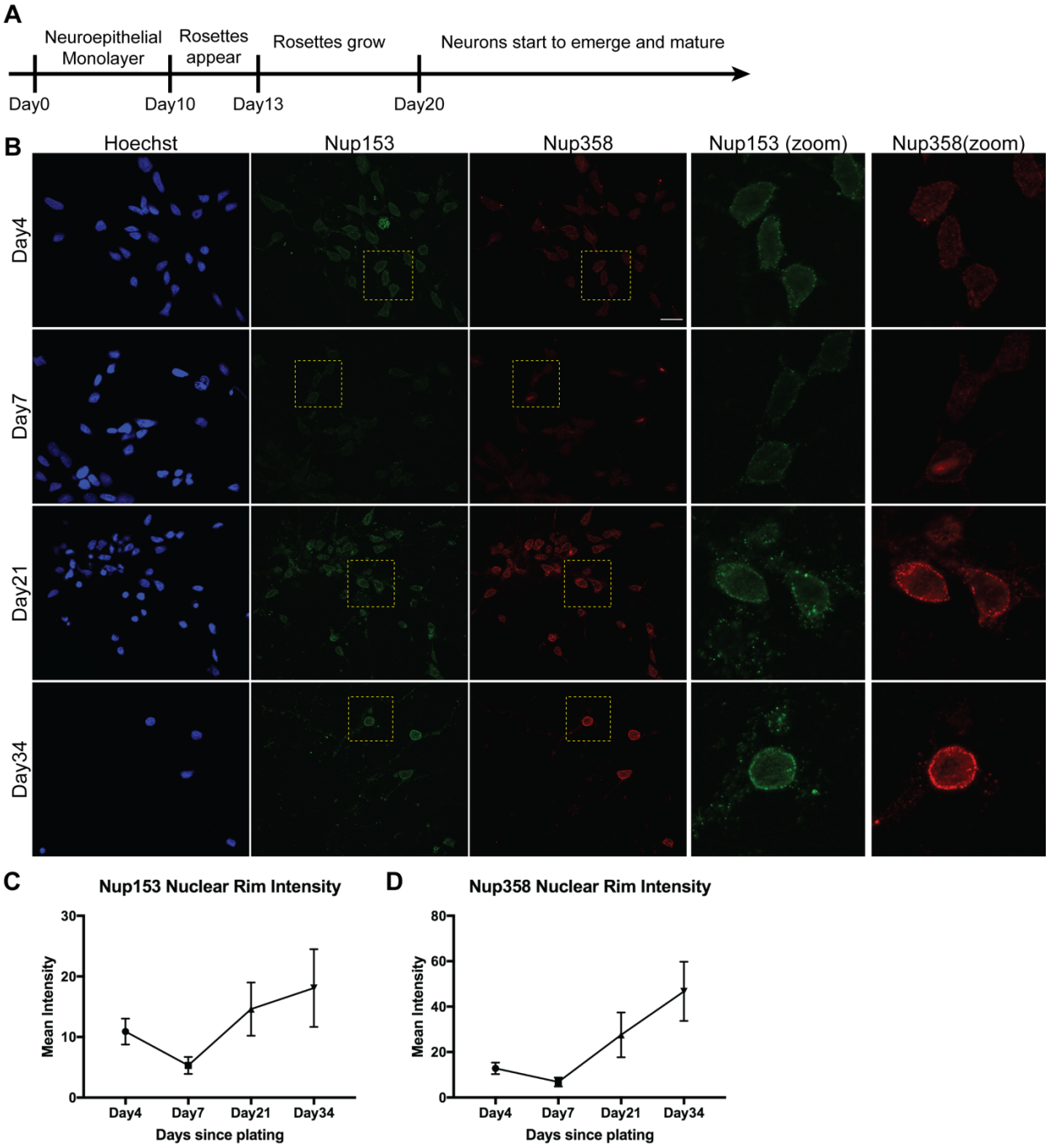


Figure 3.6: NPC nuclear rim intensity increases in neurons differentiated using dual SMAD inhibition

A) Schematic showing timeline and expected cell types during the course of dual SMAD inhibition neuronal differentiation. Neurons start to emerge around Day 20.

B) Apotome images of cells fixed at Days 4, 7, 21, and 34 throughout differentiation. Cells were stained for Hoechst, Nup153, and Nup358 with antibodies. "Zoom" panels show cells outlined in yellow boxes. Scale bar = 20µm.

C, D) Nuclear rim intensity quantitation of Nup153 (C) and Nup358 (D) in differentiating cells. Mean is calculated from the intensities measured from individual cells from one experiment. Error bars represent SD of cells in a single experiment.

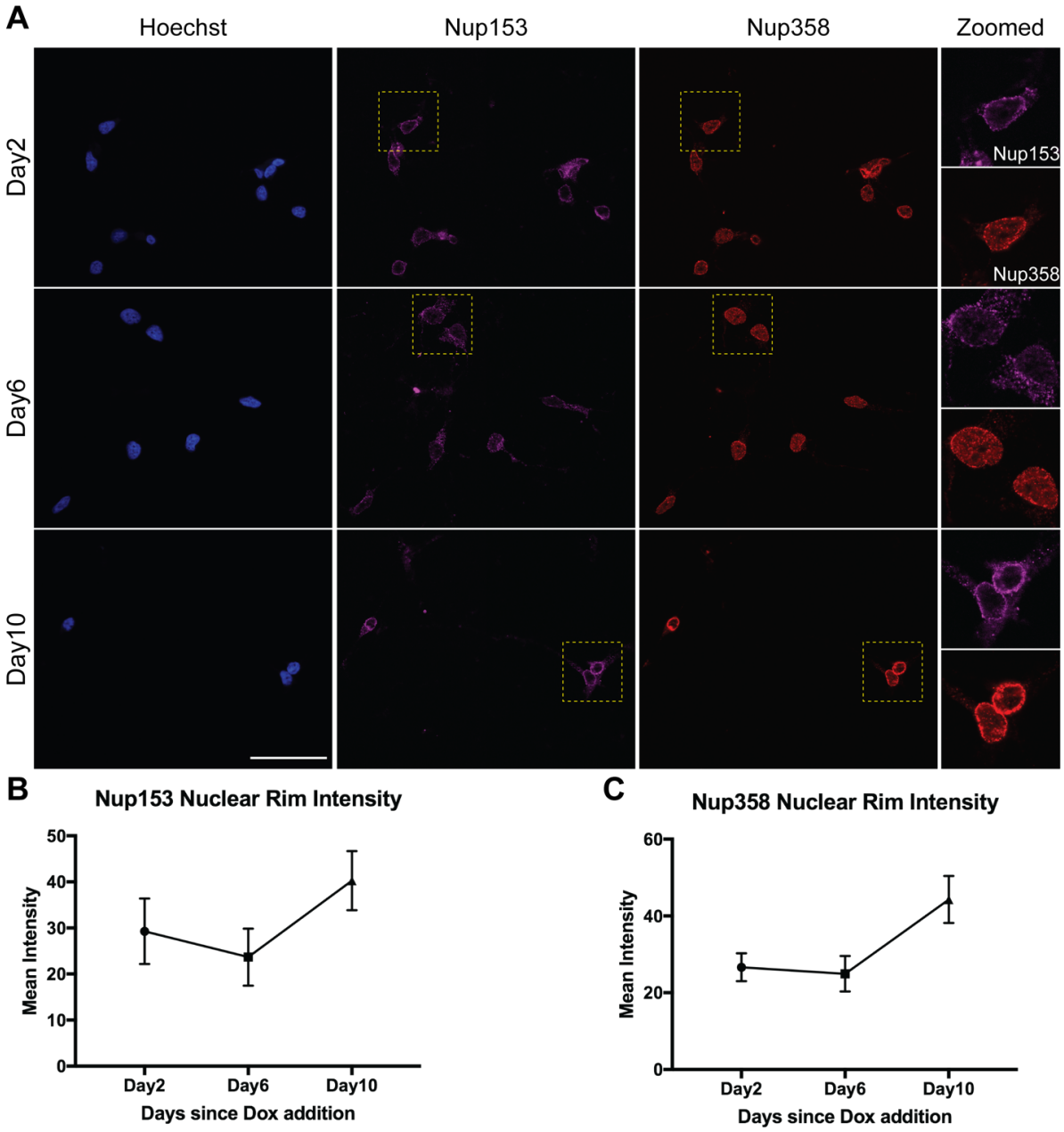


Figure 3.7: NPC nuclear rim intensity increases in neurons differentiated via neurogenin2 overexpression

A) Apotome images of cells fixed at Days 2, 6, and 10 throughout differentiation following doxycycline-mediated neurogenin2 induction. Cells were stained for Hoechst, Nup153, and Nup358 with antibodies. "Zoomed" panels show cells outlined in yellow boxes. Scale bar = 50μm

B, C) Nuclear rim intensity quantitation of Nup153 (B) and Nup358 (C) in differentiating cells. Mean is calculated from the intensities measured from individual cells from one experiment. Error bars represent SD of cells in a single experiment.

Chapter 4 TorsinA is Essential for the Timing and Localization of Neuronal Nuclear Pore Complex Biogenesis

Parts of this chapter are published (doi.org/10.1101/2023.04.26.53849; doi.org/10.1093/hmg/ddx405)

4.1 Abstract

Nuclear pore complexes (NPCs) regulate information transfer between the nucleus and cytoplasm. Abnormal NPC function and distribution are linked to several neurological diseases, but the processes governing NPC biogenesis and spatial organization are poorly understood. Here, we demonstrate that the AAA+ protein torsinA, whose loss of function causes the neurodevelopmental movement disorder DYT-TOR1A (DYT1) dystonia, coordinates neuronal NPC spatial organization without impacting total NPC density. In contrast to wild-type neurons, neurons lacking torsinA develop increasingly mislocalized clusters of NPCs. Using a newly developed HaloTag-Nup107 mouse line, we find that torsinA is essential for correct localization of NPC formation, and that NPC clusters arise due to abnormal proximity of sites of new NPC biogenesis. In the absence of torsinA, the inner nuclear membrane buds excessively at sites of mislocalized, nascent NPCs. These buds are transient, temporarily stalling NPC assembly, but resolve in mature neurons to result in delayed NPC assembly completion. Our work indicates that NPC spatial organization and number are independently regulated, suggests that torsinA is critical

for the normal localization and assembly kinetics of NPCs, and identifies NPC biogenesis as a process vulnerable to neurodevelopmental disease insults.

4.2 Introduction

Regulation of NPC biogenesis and function is essential in neurons. For example, nuclear transport of signaling molecules and transcription factors is required for neuronal plasticity[69,71,135,136], and mRNA export for local translation is critical during neural development[63,65,66,68,137]. Accordingly, aberrant function and distribution of NPCs are observed in several CNS diseases[74–78] and mutations in nucleoporins cause early-onset neurological illness[72,73]. Despite the importance of proper NPC maintenance and function, neuronal NPC biogenesis is poorly understood, and determinants of NPC number and spatial organization in both neuronal and non-neuronal systems are unknown.

TorsinA appears to lie at the intersection of neuronal NPC biogenesis and neurodevelopmental disease. TorsinA is a AAA+ protein that resides in the endoplasmic reticulum (ER)/nuclear envelope (NE) lumen[80,150,84–86,151,152,88,153]. The neurodevelopmental movement disorder DYT-TOR1A (DYT1) dystonia is caused by an in-frame 3-bp deletion in the TOR1A gene that encodes a ΔE-torsinA mutant protein[79,81]. Several observations demonstrate that the NE is an active site of torsinA activity. A "substrate trap" mutant of torsinA primarily localizes to the NE[85,86] and perturbing torsinA levels causes changes in the LINC (linker of nucleoskeleton and cytoskeleton) complex[154,155]. Mislocalization of nuclear membrane proteins is also observed in *C. elegans* germ cells lacking the torsin homolog OOC-5, which additionally exhibit asymmetric plaques of Nups[110].

TorsinA-knockout (KO) or homozygous ΔE mutant mice develop abnormal NE evaginations or "blebs" exclusively in post-migratory maturing neurons[109], establishing ΔE as a loss-of-function (LOF) mutation. Biochemical studies are consistent with a LOF effect of the ΔE mutation[87,90]. NE blebs are inner nuclear membrane (INM) outpouchings that project into the NE lumen. These blebs occur transiently, emerging during early postnatal CNS maturation and subsequently resolving without causing cell death[95,109,156]. Non-neural tissue and mitotic cell lines lacking torsinA do not exhibit NE abnormalities[89,107,111], highlighting the unique requirement for torsinA function in neurons. Indeed, in vivo studies demonstrate that torsinA function is uniquely essential during early postnatal neural development[118], emphasizing the importance of probing torsinA function in this context.

The INM budding characteristic of NE blebs suggests a potential link to interphase NPC assembly. During this process, new NPCs are inserted *de novo* into an intact nuclear membrane via INM budding and subsequent fusion with the outer nuclear membrane (ONM)[40,45,146]. Dissimilar to the budding observed in intermediate stages of normal NPC assembly, NE blebs do not fuse with the ONM and continue to enlarge into the NE lumen. Maturing torsinA-KO neurons also develop mislocalized clusters of nucleoporins which, unlike NE blebs, persist into adulthood in DYT1 mouse models[75,118]. These clusters contain Nup153, an NPC component incorporated during initial steps of biogenesis, but lack the later-recruited cytoplasmic nucleoporin Nup358 (added to the NPC after INM-ONM fusion[45]). The lack of INM-ONM fusion in NE blebs and the absence of Nup358 in nucleoporin clusters suggests that these two phenotypes may be related and implicates a potential role for torsinA in NPC biogenesis. Indeed, mitotic cells lacking multiple torsin protein family members (torsinA, torsinB, torsin2A, torsin3A) develop NE blebs that co-

localize with NPC components and are downregulated by blocking interphase NPC assembly[111,112]. Nucleoporin distribution appears normal in these cells[107,112], however, precluding their use for exploring this striking, disease-relevant phenotype. Little is known about these clusters, including their relationship to NE blebs, whether they contain formed (but mislocalized) NPCs or aggregated nucleoporins, and how they relate to NPC assembly.

Here, we identify a novel role for torsinA in the localization and timing of neuronal NPC biogenesis. In the absence of torsinA, NPC spatial organization, but not total density, is disrupted. Pulse-chase studies in primary neurons derived from HaloTag-Nup107 mice demonstrate that torsinA is essential for the normal localization of nascent NPCs. Abnormal clusters containing mislocalized NPCs arise simultaneously with the emergence of NE blebs in torsinA-KO neurons. Ultrastructural evidence from electron tomography demonstrates that NE blebs form at the sites of NPC biogenesis and represent a stalled intermediate step of NPC assembly. While abnormal NPC clusters persist, NE blebs resolve in mature neurons. Completion of new NPCs is delayed, but not permanently halted, in torsinA-KO neurons, indicating that torsinA is not essential for INM-ONM fusion as previously believed. Our work advances understanding of NPC spatial organization and newly highlights a critical role for torsinA in NPC biogenesis during a discrete developmental window.

4.3 Results

4.3.1 TorsinA is essential for uniform NPC distribution but not upregulation of NPC density

We reported previously that torsinA deletion results in long-lasting abnormal clusters of nucleoporins in neurons[75]. We asked whether neuronal NPC biogenesis is affected in the absence

of torsinA and whether formation of abnormal nucleoporin clusters coincides with increased NPC biogenesis. We fixed maturing WT and torsinA-KO neurons at DIV4, 6, 8, 10, and 14 and labeled NPCs using anti-Nup153 and anti-Nup98 antibodies. At DIV4, Nup153 and Nup98 were sparsely localized in both WT and torsinA-KO neurons such that their distribution was indistinguishable between genotypes (Figure 4.1A, B). While nucleoporin organization remained uniform in maturing WT neurons, DIV6 torsinA-KO neurons exhibited small clusters that multiplied and enlarged over time (Figure 4.1A, B). Mature torsinA-KO neurons displayed strikingly large clusters, contrary to the dense but uniform distribution observed in mature WT neurons. We conducted an autocorrelation analysis to quantitatively characterize changes in nucleoporin spatial correlation across developmental age (Figure 4.2A, B). Autocorrelation analysis conveys two types of information: the density of particles is roughly inversely correlated to the amplitude of the autocorrelation curve, and autocorrelation values indicate dispersion (<1) or clustering (>1). The decreasing amplitude of the autocorrelation curve reflected increasing density over time for both WT and torsinA-KO neurons, while a broadening of the curve for torsinA-KO neurons indicated growing clusters (Figure 4.2A). We normalized autocorrelation to total density at each timepoint to account for amplitude dependence on density. In WT neurons, normalized autocorrelation curves at all timepoints exhibited a dip <1 around 200nm indicating dispersion of nucleoporins at this distance (Figure 4.2B). In contrast, the normalized autocorrelation increased over time for torsinA-KO neurons, reflecting progressively worsening clusters.

While our SIM data demonstrate that nucleoporins form clusters at the nuclear envelope as torsinA-KO neurons mature, they do not address whether nucleoporins are recruited to NPCs or form unstructured aggregates. We therefore asked whether abnormal nucleoporin clusters contain

structures resembling normal NPCs using direct stochastic optical reconstruction microscopy (dSTORM). We labeled DIV10 neurons using a Nup210 antibody because Nup210 subunits are spaced farther apart than those of Nup98 and Nup153, enabling easier detection of individual subunits. WT neurons showed clear, uniformly distributed NPC structures containing central channels (Figure 4.1C). Similar NPC structures containing central channels were observed in torsinA-KO DIV10 neurons but were localized in clusters. We again used autocorrelation to analyze spatial correlation between NPCs. In WT neurons, the autocorrelation value was <1 between 150nm and 400nm, indicating dispersion (Figure 4.2C). In contrast, autocorrelation >1 was observed in torsinA-KO neurons over the same distance range, reflecting clustering. To further analyze spatial organization and structure of individual NPCs, we segmented individual NPCs. Plotting the nearest neighbor distance between centroids of segmented NPCs in WT neurons yielded two distinct peaks, indicating regular spatial organization of NPCs (Figure 4.2D). In torsinA-KO neurons, however, the second peak was absent, reflecting abnormal NPC spacing. We then asked whether WT and torsinA-KO NPCs exhibit structural differences. We aligned and averaged segmented NPCs (Figure 4.1D, see Chapter 2) and calculated their radii (Figure 4.1E). The average WT NPC exhibited a radius of 39nm +/- 0.3nm, while the average KO NPC had a smaller radius of 37.4 +/- 0.2nm. Despite this slight difference in NPC channel, these data clearly indicate that abnormal nucleoporin clusters in torsinA-KO neurons represent aberrantly localized clusters of NPCs rather than unstructured aggregates. Herein we refer to nucleoporin clusters as NPC clusters.

Based on our characterization of the identity of NPC clusters, we calculated NPC density in WT and torsinA-KO neurons from SIM images (Figure 4.1A, B), incorporating puncta

identified from clusters. Despite striking differences in spatial organization, there was no significant difference in average NPC density between WT and torsinA-KO neurons at any age (Figure 4.1F, G; Figure 4.2E, F), indicating that maturing WT and torsinA-KO neurons similarly upregulate NPC biogenesis. The small, statistically insignificant difference in torsinA-KO neuronal NPC density compared to WT at later timepoints is likely due to the difficulty in identifying all NPCs in clusters. We blurred a Nup210 dSTORM torsinA-KO image to simulate SIM resolution (30nm/pixel) and applied our automated peak analysis pipeline to this image. While most NPCs were identified, 2 out of the total 17 NPCs in the field of view were missed by our automated analysis (Figure 4.2G). Based on this comparison, we estimate that NPCs in clusters may be under-counted by ~10%. Nuclear area and overall shape also did not differ significantly between WT and torsinA-KO neurons (Figure 4.2H, I). Consistent with these findings, expansion microscopy to label Nup210 and LaminA/C showed no deformities in the overall nuclear shape of torsinA-KO neurons (Figure 4.2J). Furthermore, abnormal NPC clusters did not correspond to any local folds or dips in the lamin meshwork. Collectively, these data strongly suggest that torsinA is essential for the proper spatial organization, but not total density, of NPCs.

4.3.2 TorsinA-deficient neurons exhibit abnormal nucleocytoplasmic transport

The primary function of NPCs is to mediate nucleocytosolic transport. In addition to serving as a diffusion barrier that selectively allows passive transport of small macromolecules, NPCs facilitate active transport of proteins and RNA via coordination of multiple import and transport receptors (Figure 4.3A). Nup358 (also known as RanBP2) is a part of the NPC cytoplasmic filaments that binds importin-β to import cargos carrying a nuclear localization signal (NLS)[13,157] and plays a role in supporting protein export[158]. To explore whether mislocalized

clusters comprise of functional NPCs, we asked whether this component is normally recruited in maturing torsinA-KO neurons. We probed for DIV10 WT and torsinA-KO neurons with Nup153 and Nup358. As expected, we observed Nup153 clusters in torsinA-KO neurons, but Nup358 was largely absent from these clusters (Figure 4.3B). Furthermore, Nup358 nuclear rim fluorescence intensity was significantly decreased in torsinA-KO neurons compared to control neurons (heterozygous torsinA expression; Figure 4.3C). Nup358 is a late-recruited component during interphase NPC assembly, potentially suggesting that mislocalized NPCs may represent halted or stalled assembly intermediate structures. In agreement with the role of Nup358 in docking nuclear import machinery to NPCs, importin-beta also exhibited decreased localization at the nuclear rim (Figure 4.3D). We next tested whether protein transport is disrupted. We examined the nuclear to cytoplasmic (N/C) ratio of a fluorescent nuclear transport reporter containing a strong nuclear export signal and weaker nuclear localization signal (NLS-mCherry-NES[123]) in WT, heterozygous control, and torsinA-KO primary neurons. While we observed a range of nuclear to cytoplasmic signal distribution, most WT cells exhibited a higher fluorescence intensity in the cytoplasm while torsinA-KO neurons contained a higher ratio of mCherry signal in the nucleus (Figure 4.3E). This observation was reflected in quantitative N/C ratio analysis: on average, torsinA-KO neurons contained higher N/C ratio compared to WT and heterozygous neurons (Figure 4.3F). Together, these data indicate that protein transport is disrupted in DIV10 torsinA-KO neurons, likely by deficient NPC assembly that results in lack of NPC components and transport factors necessary to facilitate transport.

In addition to protein transport, NPCs also mediate RNA translocation, including post-transcriptional mRNA export to the cytoplasm. Since recruitment of Nup358 is deficient in DIV10

torsinA-KO neurons potentially indicating delayed or defective assembly, and Nup358 has a proposed role in recruiting protein factors for mRNA export[20], we hypothesized that mRNA export may also be defective. We visualized mRNAs by probing for PolyA+ RNA with fluorescence in-situ hybridization (FISH) with an oligo dT_{30} probe conjugated to Cy5. Fluorescence signal was largely localized to the cytoplasm and some nuclear compartments likely associated with active transcription. In torsinA-KO neurons, we observed small, bright puncta ("specks") that were not observed in any WT neurons (Figure 4.4A). RNA specks were mostly localized around the nuclear membrane, but occasionally observed in the cytoplasm more than 1μm away from the nucleus. Incubating neurons with RNaseA abolished fluorescence, indicating the specificity of our PolyA+ probe and FISH technique (Figure 4.4B). Surprisingly, overall N/C ratio of PolyA+ fluorescence was normal in torsinA-KO neurons (Figure 4.4C), although these specks were observed in over 60% of neurons lacking torsinA (Figure 4.4D). These results indicate that bulk mRNA export is not impacted, but specific RNA transcripts may be sequestered away in tight membraneless compartments.

4.3.3 Neurons homozygously harboring the disease-relevant ΔE mutation exhibit abnormal NPC clusters

To assess the disease-relevance of the NPC clustering phenotype, we crossed the *Nup107*$^{KI/KI}$ mice with the *Tor1a*$^{+/-}$ and the *Tor1a*$^{+/\Delta E}$ mouse lines[109]. We did not observe any deviations from Mendelian genotypic ratios in *Tor1a*$^{+/-}$;*Nup107*$^{KI/KI}$ intercross (Figure 4.6A). We probed for HaloTag-Nup107 in WT (*Tor1a*$^{+/+}$;*Nup107*$^{KI/KI}$) or torsinA-KO (*Tor1a*$^{-/-}$;*Nup107*$^{KI/KI}$) DIV10 neurons and observed abnormal NPC clusters in torsinA-KO neurons as expected (Figure 4.5A, A'). Abnormal clusters were also observed in DIV10 neurons homozygously harboring the

disease-relevant ΔE allele (torsinA-ΔE/ΔE; Figure 4.5B, B'), further supporting ΔE as a loss of function mutation and demonstrating a clear link between the NPC clustering phenotype and DYT1 pathophysiology. NPCs did not appear clustered in torsinA-ΔE/+ neurons, indicating that heterozygous expression of normal torsinA is sufficient for maintaining NPC distribution and consistent with the low penetrance of the disease in carriers of the ΔE mutation.

4.3.4 Sites of NPC biogenesis are abnormal in torsinA-KO neurons

To elucidate how NPC clusters arise in the absence of torsinA, we performed a pulse-chase experiment using HaloTag-Nup107 neurons to label NPCs formed at different stages of neuronal maturation. Neurons from WT (*Tor1a*$^{+/+}$;*Nup107*$^{KI/KI}$) or torsinA-KO (*Tor1a*$^{-/-}$;*Nup107*$^{KI/KI}$) mice were labeled with JFX554 HaloTag ligand overnight from DIV3 to DIV4 to saturate labeling of all existing Nup107. Following dye washout, some neurons were fixed and the rest were grown in JF646-containing media to label NPCs formed between DIV4 and time of fixation (Figure 4.6B). This pulse-chase labeling approach allowed us to distinguish NPCs formed up to DIV4 from those formed at DIV4-6, DIV4-8, or DIV4-10. We used this approach to test two possible mechanisms of NPC cluster formation: (i) rearrangement of NPCs post-formation, and (ii) improper localization of *de novo* assembling NPCs (Figure 4.6C). If NPCs rearrange into clusters post-formation in torsinA-KO neurons, clustering of both pulse- and chase-labeled NPCs is expected (Figure 4.6C, top). In contrast, if sites of new NPC biogenesis are mislocalized in the absence of torsinA, clustering of exclusively chase-labeled NPCs would be observed (Figure 4.6C, bottom).

Consistent with our previous findings, NPC biogenesis was upregulated in both genotypes and torsinA-KO neurons exhibited clustered NPCs (Figure 4.7A). We used automated image analysis to identify NPCs formed up to DIV4 and those formed subsequently. The density of pulse-

labeled (JFX554) NPCs remained constant over time. In contrast, the density of newly formed NPCs (new JF646; JF646-positive NPCs that do not overlap with JFX554) increased in both WT and torsinA-KO neurons (Figure 4.7B-E), indicating successful pulse-chase labeling. JFX554-labeled NPCs maintain a sparse, dispersed distribution at all timepoints in both genotypes, even in DIV10 torsinA-KO neurons that contain large NPC clusters as observed via Nup153 labeling (Figure 4.8A, C). In WT neurons, NPCs that form after DIV4 localize in empty spaces devoid of previously formed NPCs, preserving an overall uniform pattern of NPC distribution. In contrast, new NPCs that form after DIV4 in torsinA-KO neurons abnormally form in close proximity to one another, creating increasingly large clusters (Figure 4.8B, D). These data support our second proposed mechanism in which mislocalization of newly forming NPCs leads to the development of NPC clusters in torsin-KO neurons. These data suggest that torsinA is an essential factor in determining sites of *de novo* NPC biogenesis. These experiments also demonstrate that in developing neurons, the spatial organization of NPCs is determined by the site of NPC formation rather than by post-formation rearrangement.

4.3.5 NE blebs form at sites of NPC biogenesis

Abnormal NE blebs form selectively in post-migratory neurons in the torsinA-KO nervous system[95,109]. To further probe the potential link between NE bleb formation and NPC biogenesis, we explored the temporal and spatial relationship between these processes. To determine if NE blebs in torsinA-KO primary neurons form concomitantly with NPC biogenesis, we examined the nuclear membrane of WT and torsinA-KO neurons at DIV4 and DIV10 using transmission electron microscopy. We observed NE blebs in torsinA-KO neurons at both DIV4 and DIV10 (Figure 4.9A). Significantly more cells exhibited NE blebs at DIV10 (Figure 4.9B) and bleb

frequency per cell increased dramatically from DIV4 to DIV10 (Figure 4.9C). NPC density increases almost twofold and abnormal NPC clusters emerge during this same period (DIV4–10), demonstrating a temporal link between these processes.

We next explored whether NE blebs and NPC clusters overlap spatially. One possibility is that areas of the NE with blebs are not suitable for NPC formation. Alternatively, colocalization of NPCs and NE blebs would support a mechanistic link between these processes. We tested these possibilities by generating 3D volumes of the WT and torsinA-KO DIV10 neuronal nuclear envelopes using intermediate high voltage scanning transmission electron microscopy (STEM) and multi-tilt electron tomography (Video 1). We observed NE blebs both as isolated entities and in clusters of several blebs enclosed within a single stretch of the outer nuclear membrane (Video 1, Figure 4.10A). In all cases, blebs connected to the nuclear membrane via pore channels (Figure 4.9D, E, Video 2) and we did not observe any NPC clusters between NE blebs. We did not observe any examples of vesicles reminiscent of large ribonucleoprotein granules reported in torsin mutant *Drosophila* cells[102]. Projection of all KO pores (regular and bleb-associated) clearly showed clustered distribution similar to SIM images of mature torsinA-KO neurons (Figure 4.10B). Considered together, the temporal and spatial connection between NE bleb and NPC formation support the hypothesis that NE blebs form at the sites of nascent NPCs in torsinA-KO neurons.

4.3.6 Bleb-associated NPCs exhibit narrow channel size

The 3D volumes also allowed us to analyze the dimensions of NPCs from WT and torsinA-KO neurons (Figure 4.10C). On average, the diameter of a pore in WT neurons was 80nm. Regular (not bleb-associated) pores in torsinA-KO neurons were slightly narrower, at 74.6nm, and bleb-associated KO pores were even smaller (69.8nm). These data are consistent with our dSTORM

data and additionally demonstrate that even normal appearing NPCs in torsinA-KO neurons may not be able to dilate to the same degree as WT NPCs. We also found that the central plugs of bleb-associated pores facing the nucleoplasm are more electron dense compared to the plugs of regular pores, even within a single torsinA-KO neuron (Figure 4.10D). While the identity of these central plugs is unclear, they appear similar to plugs observed in immature NPCs[24,45].

4.3.7 NE blebs resolve as neurons continue to mature

NE blebs are transient in vivo, resolving without causing cell death[95,156]. We therefore explored whether blebs are also transient in torsinA-KO primary neurons. We examined the nuclear membrane of DIV10 and DIV18 WT and torsinA-KO neurons since our NPC density characterization suggests that NPC density may begin to plateau by DIV18. Both the prevalence and frequency of NE blebs decreased significantly between DIV10 and DIV18 in torsinA-KO neurons (Figure 4.11A-C). In addition, we observed regions of the NE with multiple adjacent complete NPCs marked by fused INM and ONM in DIV18 torsinA-KO neurons (Figure 4.11A, last panel).

4.3.8 Completion of NPC assembly is delayed in torsinA-KO neurons

We hypothesized that NPC assembly resumes and completes upon the resolution of NE blebs. To test this hypothesis and assess the NPC assembly state over time in torsinA-KO neurons, we labeled early- and late-recruited components, Nup153 and Nup358 respectively, at DIV10 and DIV18. At DIV10, Nup153 nuclear rim fluorescence intensity was similar between torsinA-KO and WT neurons, but Nup358 localization was reduced in torsinA-KO neurons (Figure 4.12A, B). These data are consistent with our previous report[75] and indicate that NPCs are stalled at an

intermediate state in the absence of torsinA at this timepoint. At DIV18, however, Nup358 was successfully recruited to NPC clusters marked by Nup153 and the fluorescence intensity was restored (Figure 4.12C, D). We also validated this finding at single-NPC resolution using SIM (Figure 4.13A). Nup358 was sparsely distributed and failed to localize to clusters containing Nup153 in DIV10 torsinA-KO neurons. By DIV18, however, Nup358 exhibited clustered localization that overlapped with Nup153-positive clusters. Such a delay in NPC assembly completion was not observed in WT neurons, as most NPCs were labeled with both Nup153 and Nup358 at DIV10. Notably, NPCs remained clustered in DIV18 torsinA-KO neurons as observed by dSTORM and analyzed using autocorrelation (Figure 4.13B, C). These data indicate that torsinA is not required for fusion of the inner and outer nuclear membranes during interphase NPC assembly in neurons, as loss of torsinA causes delayed, rather than permanently halted, NPC biogenesis.

4.4 Discussion

Our work establishes that torsinA is essential for the normal assembly kinetics and localization of interphase NPC biogenesis in neurons (Figure 4.14A, B). We find that NPC biogenesis is strongly and steadily upregulated during neuronal maturation even in the absence of torsinA, and that in torsinA-KO neurons, nascent NPCs localize abnormally into persisting, tightly packed clusters. In contrast to the aberrant spatial organization, the onset of NPC formation and total NPC density remain normal, suggesting that NPC number and NPC localization are governed by distinct mechanisms. We demonstrate directly using STEM tomography that inner nuclear membrane blebs in torsinA-KO neurons represent stalled intermediates of NPC assembly. Unlike the NPC clusters, however, these blebs resolve over time and allow NPC assembly to resume,

resulting in delayed completion of NPC biogenesis. Considered together, our findings newly identify NPC upregulation as an important feature of neuronal maturation and provide insight into the poorly understood process of NPC spatial organization.

Our quantitative NPC distribution analyses demonstrate that WT NPCs are evenly dispersed at all timepoints assessed, suggesting the presence of a mechanism to maintain NPC spacing. Evenly dispersed NPCs have been observed in other cell types via EM studies[159], but the mechanism that maintains NPC spatial organization is unknown. Our dSTORM studies clearly show that the nucleoporin clusters identified in confocal and SIM imaging contain NPCs with central pore channels, indicating a role for torsinA in neuronal NPC organization. Our data further suggest that independent pathways regulate NPC number and spatial organization: despite their mislocalization, the initiation of NPC assembly is unaffected as nucleoporins spanning multiple NPC subcomplexes are present in clusters (Nup153, Nup98, Nup210, and Nup107) and total NPC density is similar between WT and torsinA-KO neurons at all timepoints.

The pulse-chase studies of endogenous HaloTag-Nup107 demonstrate that torsinA loss disrupts the normal sites of NPC biogenesis. In maturing torsinA-KO neurons, NPCs form abnormally close to one another, implicating torsinA as a determinant of nascent NPC localization in neurons. We considered the possibility of NPC redistribution into clusters in the absence of torsinA since post-formation NPC rearrangement is observed in yeast[32,160], and lamins, which are believed to anchor NPCs, appear abnormally shaped in some torsinA-KO neurons[75]. We find no evidence to support NPC redistribution into clusters; NPCs marked in immature torsinA-KO neurons are normally distributed and remain so throughout neuronal maturation. Most of these normally distributed NPCs are likely formed via a postmitotic NPC assembly mechanism prior to

terminal neuronal differentiation, since torsinA loss does not cause NPC abnormalities in mitotic cells[107,111]. Indeed, interphase NPC assembly requires functional NPC transport[161,162,52], and these normally distributed NPCs likely facilitate neuronal NPC biogenesis. Remarkably, these NPCs are not degraded during neuronal maturation as shown by our pulse-chase study, reflecting the long half-life of Nup107[57,143] and lack of neuronal NPC turnover[61,62].

How might torsinA ensure that nascent NPCs are properly localized? One possibility is that NPC formation requires a specific lipid microenvironment that is maintained by torsinA. The inner nuclear membrane (INM) is a metabolically active entity that can sense lipids[163–168]. The *Drosophila* torsin ortholog dTor maintains lipid homeostasis at the nuclear membrane[105–107], and torsinA plays a role in mammalian hepatic lipid metabolism[108]. While no difference in lipids were found in mitotic cells lacking torsins[111], NPC clustering is not observed in these nonneuronal cells. Future studies may reveal neural-specific spatial anomalies of specific lipids or lipid-binding proteins related to aberrant NPC localization. Another possibility is that torsinA may have a structural role in ensuring even distribution of INM proteins required for NPC assembly. Identification of torsinA interacting proteins in future studies will guide mechanistic studies on how torsinA participates in the proper localization of NPC biogenesis.

Our dSTORM and STEM data demonstrate that the central channel of the average NPC in DIV10 torsinA-KO neurons is slightly but significantly narrower than the average WT NPC. Interphase NPC assembly involves lateral dilation of the budding NPC prior to INM and ONM fusion[40,45,146], suggesting that the smaller central channel of these NPCs may reflect stalled assembly intermediates that have not yet fully dilated. Consistent with this possibility, our EM data reveal that NE blebs emerge concurrently with upregulated NPC biogenesis and spatially

correlate with mislocalized NPCs. These findings are similar to previous reports of NE blebs colocalizing with NPC components in mitotic cells lacking multiple torsin paralogs[111]. We additionally observe dense central plugs on the nucleoplasmic side of NE-bleb associated NPCs. These electron-dense plugs appear similar to plugs reported in newly forming pores[24,45] and potentially represent unique machinery present in intermediate NPC structures.

Prior observations suggested that neuronal torsinA or torsins in mitotic cells may be involved in the INM-ONM fusion step of interphase NPC assembly. Chief among these observations is that Nup358, a cytoplasmic NPC component, is not recruited to Nup153-positive clusters in DIV10 torsinA-KO neurons[75] or in interphase-formed NPCs in torsin-deficient mitotic cells[112]. Data from mitotic cells lacking torsins have also been used to support the hypothesis that NE blebs are a consequence of defective NPC assembly[112,113,115,169]. We demonstrate that torsinA is dispensable for INM-ONM fusion and that NPC biogenesis is delayed, rather than permanently halted, in the absence of torsinA. While DIV10 torsinA-KO neurons exhibit numerous NE blebs, these blebs resolve as the neurons mature, similar to the disappearance of blebs during CNS maturation *in vivo*[95]. NE bleb resolution is accompanied by the resumption of NPC assembly, as Nup358 is present in Nup153-positive NPC clusters in DIV18 torsinA-KO neurons. This contrasts sharply with findings in mitotic cells lacking multiple torsin paralogs[111–113], in which completion of NPC assembly is not observed, possibly due to the difference in timescale of assembly between the cell types. Based on these new observations, we propose that NE blebs contribute to delayed NPC biogenesis by posing a physical barrier to the continuation of NPC assembly. The origin of NE blebs remains unclear. One possibility is that excessive INM budding occurs during NPC biogenesis in torsinA-KO neurons due to lipid environments unconducive to INM-ONM fusion.

In this scenario, torsinA may play no direct role in NPC assembly, abnormalities of which may be a bystander effect of torsinA-related lipid defects[105–107]. NE blebs may resolve through correction of lipid composition via NE-ER junctions.

How might NPC abnormalities caused by torsinA deletion contribute to neural dysfunction? NPC function is compromised in maturing torsinA-KO neurons as demonstrated by lack of Nup358 and importin-β recruitment and abnormal protein nucleocytoplasmic transport. Additionally, the accumulation of perinuclear RNA specks raises the possibility of transcriptomic defects. While we did not examine transport in neurons harboring the disease-causing ΔE mutation, cholinergic motor neurons differentiated from DYT1 patient fibroblasts exhibit abnormal RNA and protein transport[170]. Our STEM data indicate that even NPCs not associated with blebs in torsinA-KO neurons are smaller than WT NPCs, raising the intriguing possibility that full dilation of the NPC channel may be restricted regardless of assembly state. A persistently narrow channel size could limit the size of molecules that are able to diffuse through the NPCs. Such differences may negatively impact nucleocytoplasmic transport-dependent neural functions such as synaptic plasticity[69,71,135,136], dysfunction of which is linked to the clinical manifestation of dystonia[171,172]. Delayed NPC assembly in maturing neurons may interfere with transport of locally translated RNA critical for neurodevelopmental processes such as dendritic outgrowth, axonal guidance and synaptogenesis[63,65,66,68,137], which is altered in torsinA-KO[173] and torsinA-ΔE knock-in brains[174–177]. Lastly, nucleoporins, including Nup153 and Nup98, physically interact with the genome and influence transcription[25–28,178]. NPC mislocalization may therefore lead to transcriptomic changes by altering the chromatin landscape.

TorsinA plays a unique and essential role during neural development. Neuronal torsinA levels are high during early postnatal development and decrease over subsequent weeks[95]. Deletion of torsinA from neural progenitors causes significant behavioral and neuropathological effects[114], while eliminating torsinA in adult mice does not cause any phenotypes[118]. Conversely, restoring torsinA levels in juvenile, but not adult mice lacking torsinA, prevents such phenotypes, highlighting a critical window of torsinA function[118,179]. Our findings establish NPC biogenesis as a key molecular event of this neurodevelopmental critical period and raise the possibility that NPC-related processes may underlie additional critical periods in normal development as well as early- and late-onset neurological disorders.

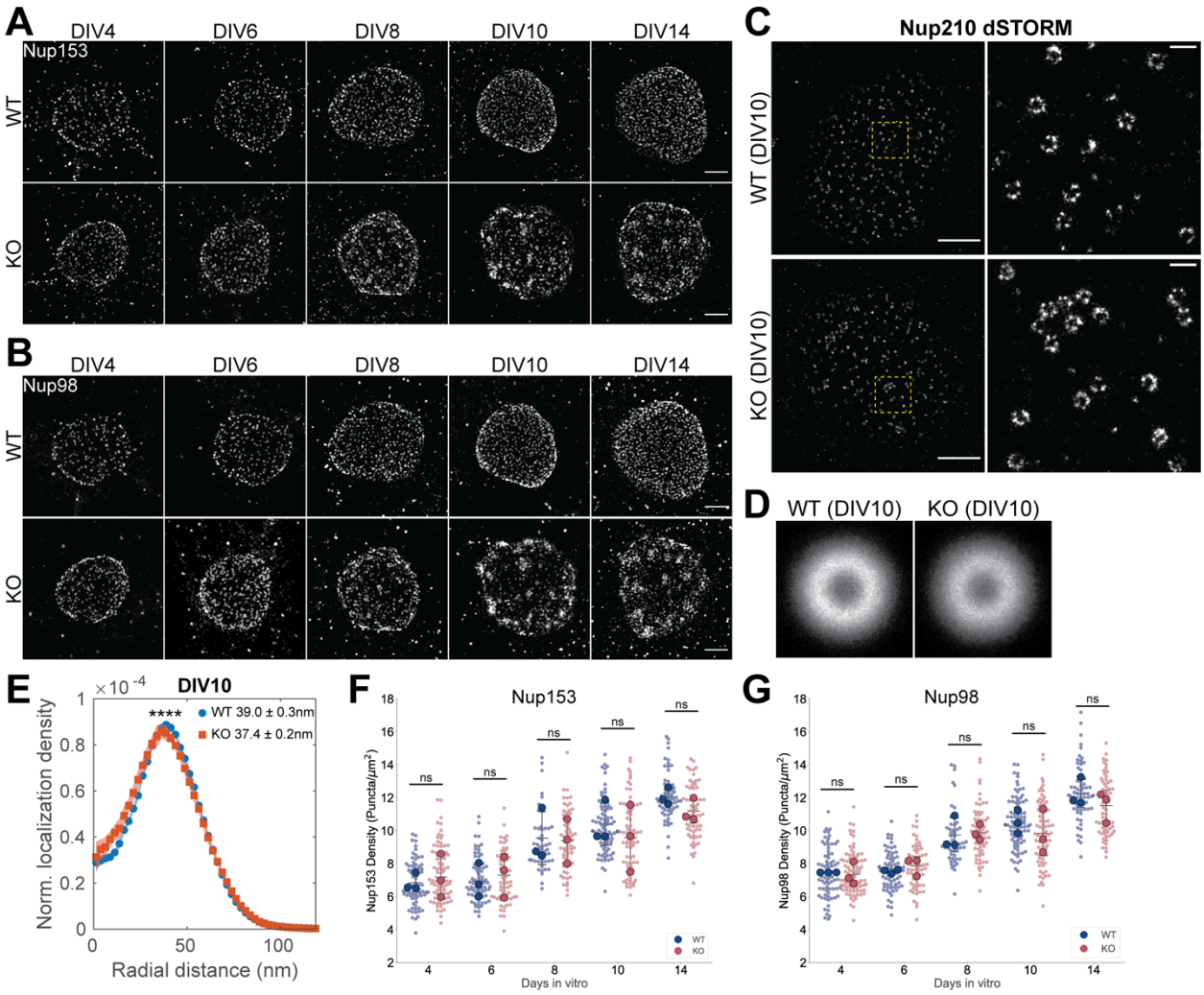


Figure 4.1: TorsinA is essential for uniform NPC distribution but not upregulation of NPC biogenesis

A, B) SIM images of WT and torsinA-KO primary neurons aged DIV4, 6, 8, 10, and 14 labeled with anti-Nup153 (A) and anti-Nup98 (B) antibodies. Scale bar = 2μm.

C) dSTORM images of Nup210-labeled NPCs in DIV10 WT and torsinA-KO neurons. Scale bar = 2nm. Right panels show zoomed in view of boxed regions. Scale bar of right panels = 200nm.

D) Averaged aligned DIV10 WT and torsinA-KO pores.

E) Normalized localization density along radial distance in averaged WT and KO pores. Plots show mean ± SEM from eight bootstrapping rounds with 250 randomly selected pores each. ****P<0.0001.

F, G) Nup153 (F) and Nup98 (G) density (puncta/μm^2) in maturing primary neurons. Plots show mean ± SD. Timepoints from each replicate were matched and repeated measures two-way

ANOVA with Sidak's multiple comparisons test was performed to compare means between genotypes. ns, not significant.

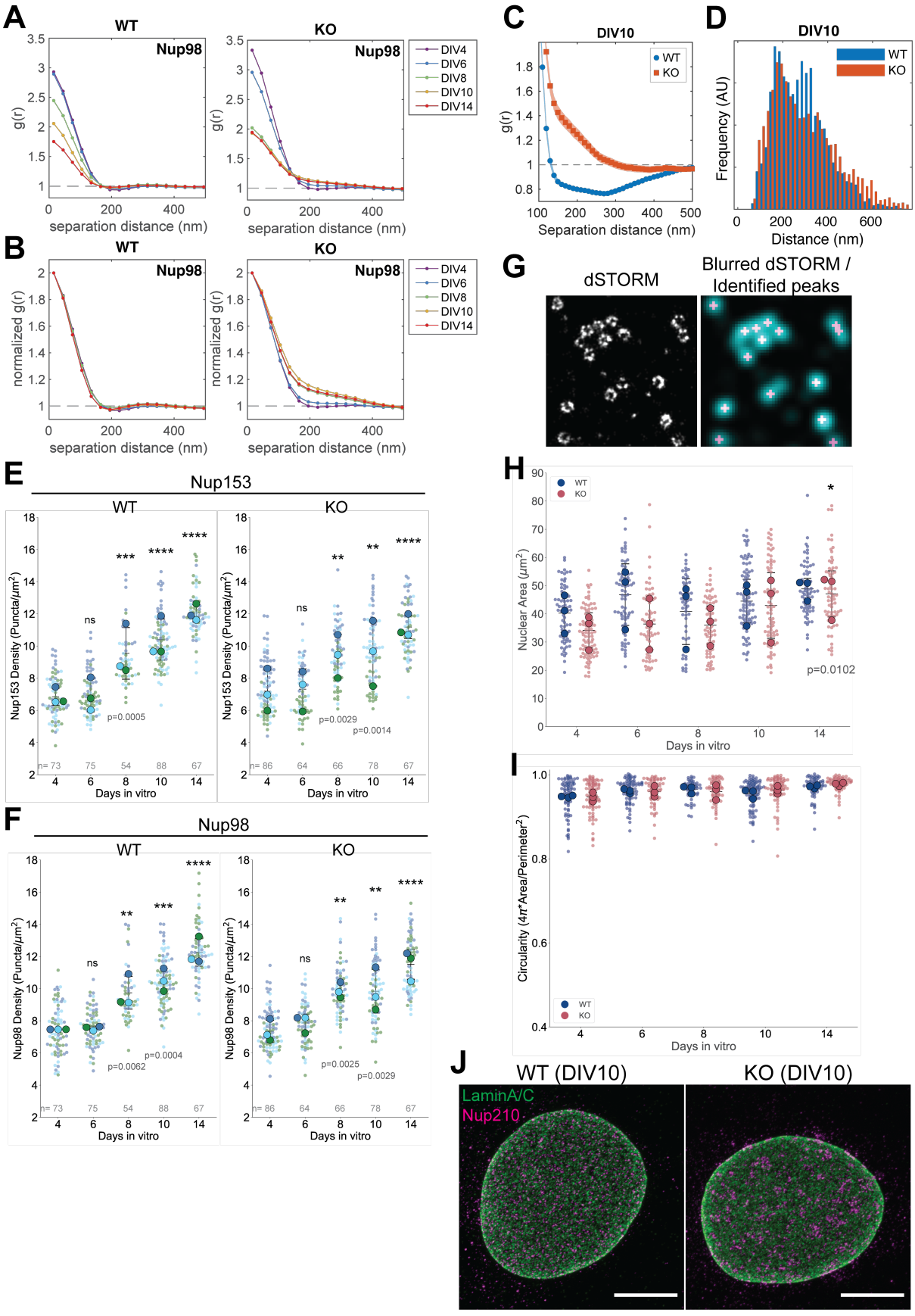

A
WT
KO
Nup98
g(r)
separation distance (nm)
DIV4
DIV6
DIV8
DIV10
DIV14
B
normalized g(r)
C
DIV10
WT
KO
Separation distance (nm)
D
Frequency (AU)
Distance (nm)
G
dSTORM
Blurred dSTORM / Identified peaks
E
Nup153
Nup153 Density (Puncta/μm²)
Days in vitro
p=0.0005
p=0.0029
p=0.0014
F
Nup98
Nup98 Density (Puncta/μm²)
p=0.0062
p=0.0004
p=0.0025
p=0.0029
H
Nuclear Area (μm²)
p=0.0102
I
Circularity (4π*Area/Perimeter²)
J
WT (DIV10)
KO (DIV10)
LaminA/C
Nup210

Figure 4.2: Comparison of WT and torsinA-KO neuronal NPC spatial organization and nuclear morphology

A) Autocorrelation plot of WT and torsinA-KO neurons calculated from Nup98 WT and torsinA-KO SIM images.
B) Normalized autocorrelation plot of WT and torsinA-KO neurons calculated from Nup98 WT and torsinA-KO SIM images. Autocorrelations were normalized to account for amplitude dependency on NPC density.
C) Autocorrelation plot of DIV10 WT and torsinA-KO neurons calculated from Nup210 dSTORM images.
D) Nearest neighbor distance of segmented DIV10 WT and torsinA-KO NPC centroids.
E, F) WT and torsinA-KO Nup153 (E) and Nup98 (F) puncta density in maturing primary neurons aged DIV4, 6, 8, 10, 14. Plots show mean $\pm$ SD, with color coding indicative of biological replicates. Timepoints from the same biological replicate were matched. ns, non-significant; ****P<0.0001; repeated measures two-way ANOVA with Dunnett's multiple comparisons test, using DIV4 as a reference.
G) dSTORM image of Nup210 image and the same image blurred to 30nm/px resolution to imitate what a SIM image would look like. Crosshairs mark peaks identified by applying the SIM analysis pipeline to the blurred image. 17 NPCs are identifiable in the dSTORM image; 15 NPCs are identified in the blurred image.
H) Nuclear area of WT and torsinA-KO neurons calculated from manually drawn ROIs from SIM images. Plots show mean $\pm$ SD. Repeated measures two-way ANOVA with Sidak's multiple comparisons test was used to compare genotypes at each timepoint, and no comparisons reached statistical significance. Repeated measures two-way ANOVA with Dunnett's multiple comparisons test was used to compare all timepoints to DIV4 within each genotype.
I) Nuclear ROI circularity of WT and torsinA-KO neurons calculated from manually drawn ROIs from SIM images. Plots show mean $\pm$ SD. Repeated measures two-way ANOVA with Sidak's multiple comparisons test was used to compare genotypes at each timepoint. No statistical significance was detected.
J) Expansion microscopy of DIV10 WT and torsinA-KO neurons labeled with Nup210 and Lamin A/C antibodies. Scale bar = 20μm.

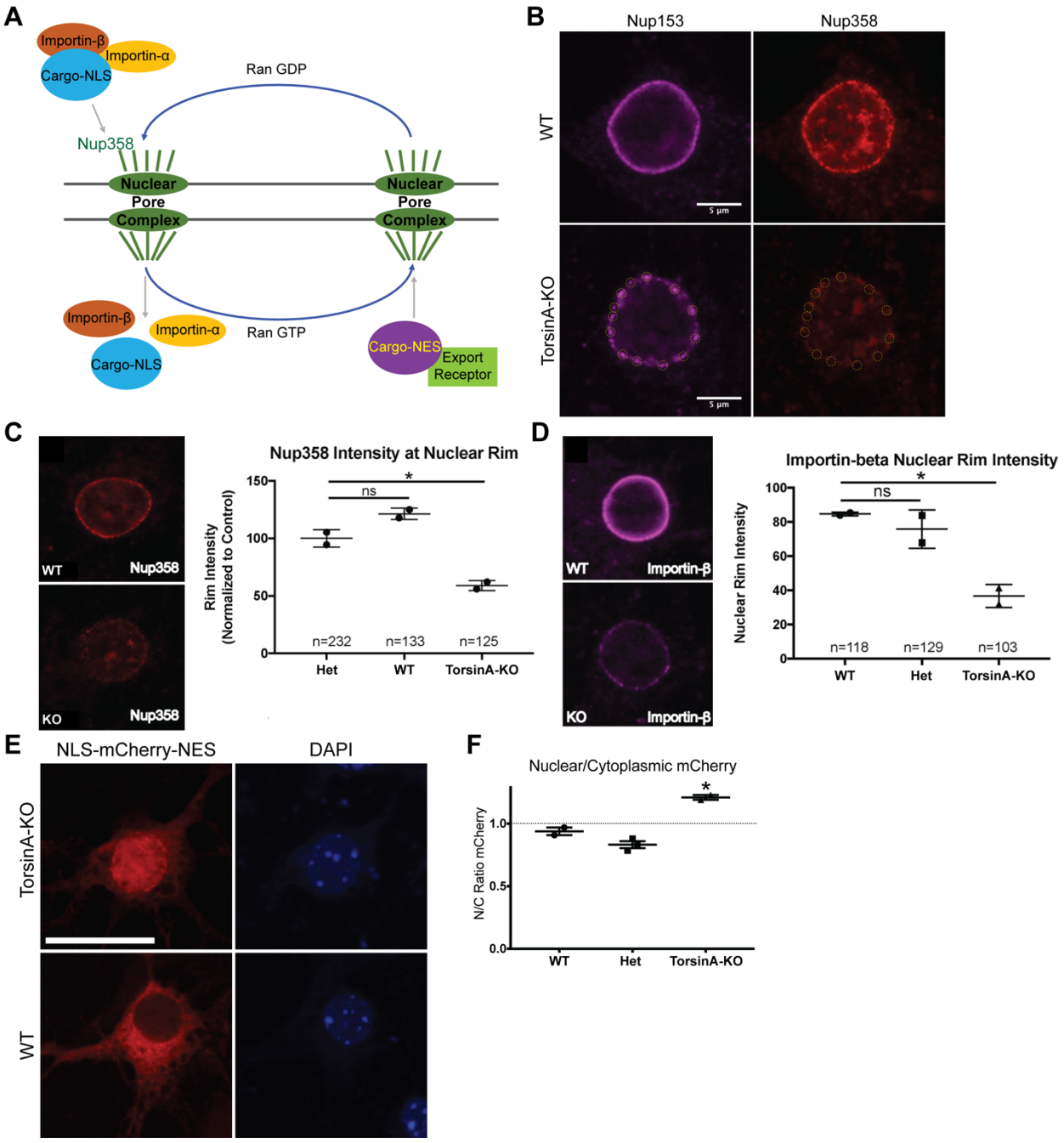


Figure 4.3: TorsinA-KO neurons exhibit deficient recruitment of transport components and abnormal protein transport

A) Simplified schematic of protein import and export facilitated by NPCs. Protein cargo carrying a nuclear localization signal (NLS) is recognized by importin-α and importin-β. Nup358 mediates docking of the cargo-importin complex and cargo is imported into the nucleus. In the

nucleoplasm, importins and cargo dissociate through a mechanism involving Ran-GTP. For export to the cytoplasm, export receptors and Ran-GTP bind a cargo carrying a nuclear export signal (NES). Upon translocation to the cytoplasm, Ran-GTP is hydrolyzed to Ran-GDP, releasing the export receptor and the cargo.

B) DIV10 WT and torsinA-KO neurons labeled with Nup153 and Nup358 antibodies. Circles on torsinA-KO images denote areas of Nup153 clusters.

C) DIV10 WT, torsinA-Het, and torsinA-KO neurons were labeled with Nup358 antibody and nuclear rim intensity was measured. Only WT and torsinA-KO images are shown as examples. Nuclear rim intensity was normalized to Het control. "n" denotes total cells analyzed. Plots show mean $\pm$ SD. Unpaired t-test was used to determine significance, *P<0.05; ns= not significant.

D) DIV10 WT, torsinA-Het, and torsinA-KO neurons were labeled with importin-β antibody and nuclear rim intensity was measured. Only WT and torsinA-KO images are shown as examples. "n" denotes total cells analyzed. Plots show mean $\pm$ SD. Unpaired t-test was used to determine significance, *P<0.05; ns= not significant.

E) NLS-mCherry-NES and DAPI immunofluorescence in DIV8 WT and torsinA-KO neurons. Scale bar = 20μm.

F) Nuclear to cytoplasmic ratio of mCherry immunofluorescence in WT, torsinA-Het, and torsinA-KO DIV8 neurons. Plots show mean $\pm$ SEM.

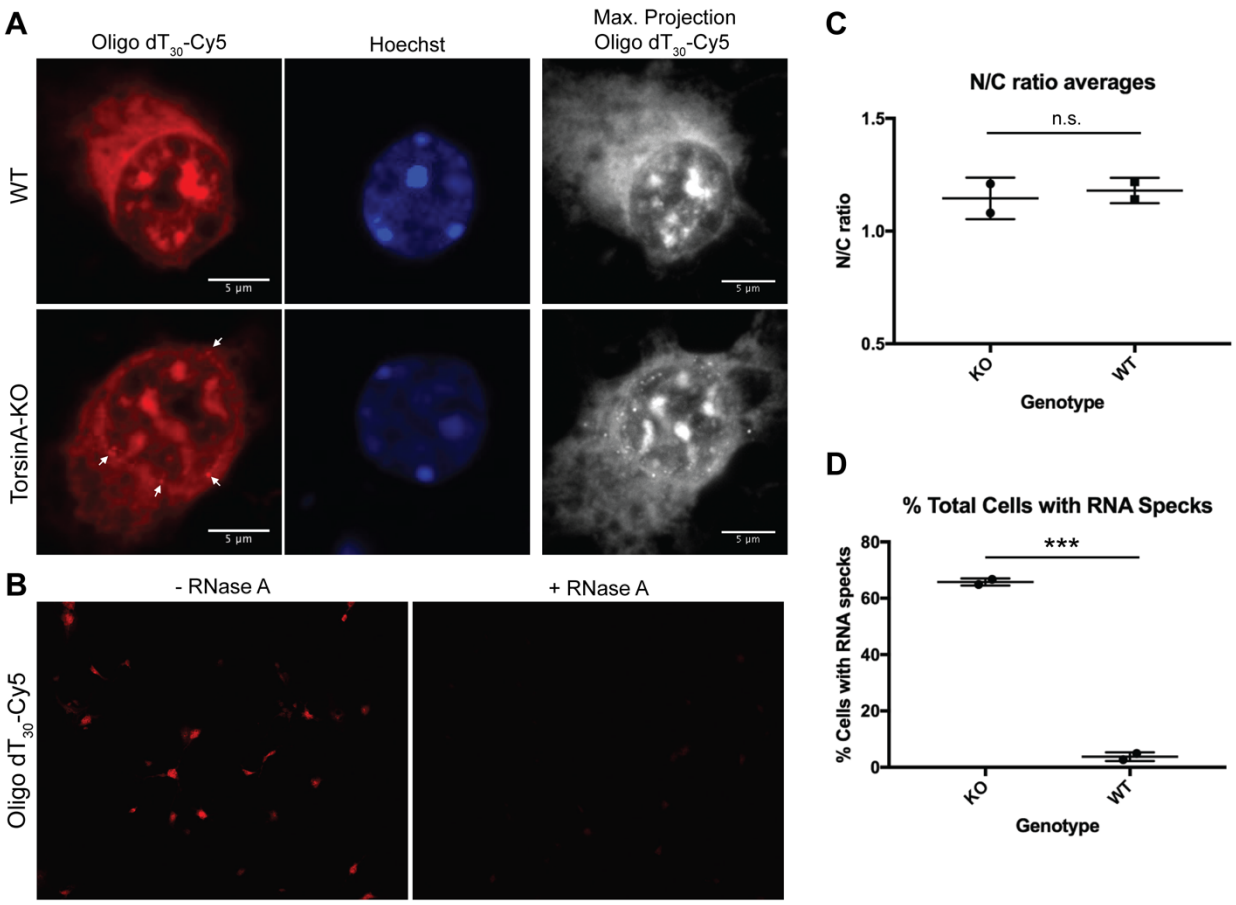


Figure 4.4: TorsinA-KO neurons exhibit perinuclear PolyA+ RNA puncta

A) DIV10 WT and torsinA-KO neurons probed for PolyA+ RNA by conducting fluorescence in-situ hybridization (FISH) with an oligo dT_{30}-Cy5 probe. For each genotype, the first two panels show a single optical slice. Rightmost panels show a maximum intensity projection.
B) Validation of PolyA+ RNA FISH by treating neurons with or without RNaseA.
C) Nuclear to cytoplasmic ratio of DIV10 torsinA-KO and WT neurons shown in (A). Plots show mean $\pm$ SD. Unpaired t-test was used; no significance was detected.
D) % of cells with RNA specks in DIV10 torsinA-KO and WT neurons. % of cells with the phenotype were quantitated in a blinded analysis. Plots show mean $\pm$ SD and points correspond to biological replicates. Unpaired t-test was used, ***$P<0.001$.

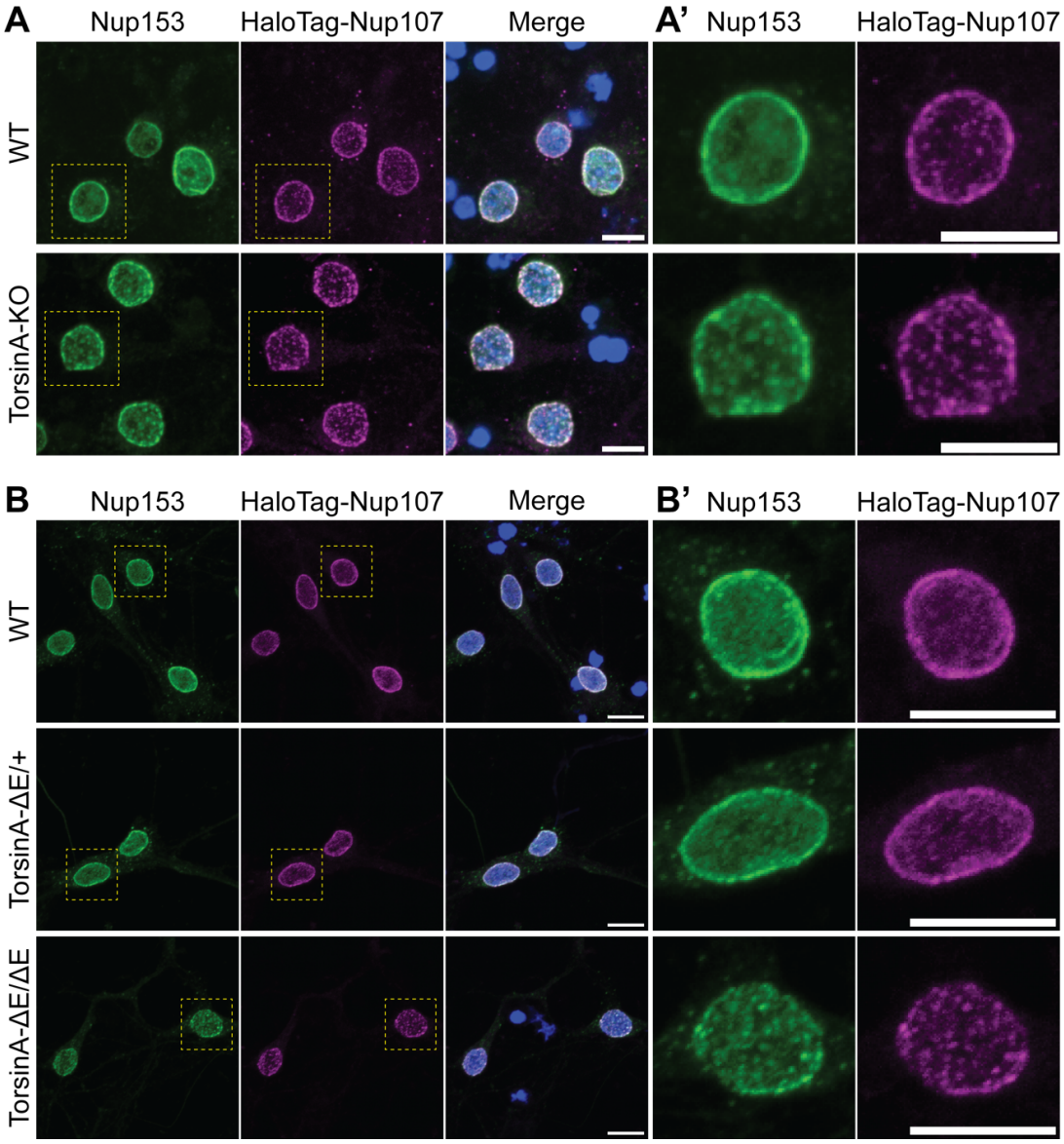


Figure 4.5: Neurons homozygously harboring the disease-relevant ΔE mutation exhibit abnormal clusters

A) Confocal z-stack maximum intensity projection of DIV10 WT and torsinA-KO neurons expressing HaloTag-Nup107. Nup107 was labeled with JF646 HaloTag ligand and cells were probed with anti-Nup153 antibody post-fixation. Merge panel shows Hoechst (blue), JF646 (magenta), and Nup153 (green). Scale bar = 10μm. (A') Zoomed-in view of cells outlined by yellow boxes in (A). Scale bar = 10μm.

B) Confocal z-stack maximum intensity projection of DIV10 WT and torsinA-ΔE/ΔE neurons expressing HaloTag-Nup107. Nup107 was labeled with JFX554 HaloTag ligand and cells were probed with anti-Nup153 antibody post-fixation. Scale bar = 10μm. Merge panel shows

Hoechst (blue), JFX554 (magenta), and Nup153 (green). (B') Zoomed-in view of cells outlined by yellow boxes in (B). Scale bar = 10μm.

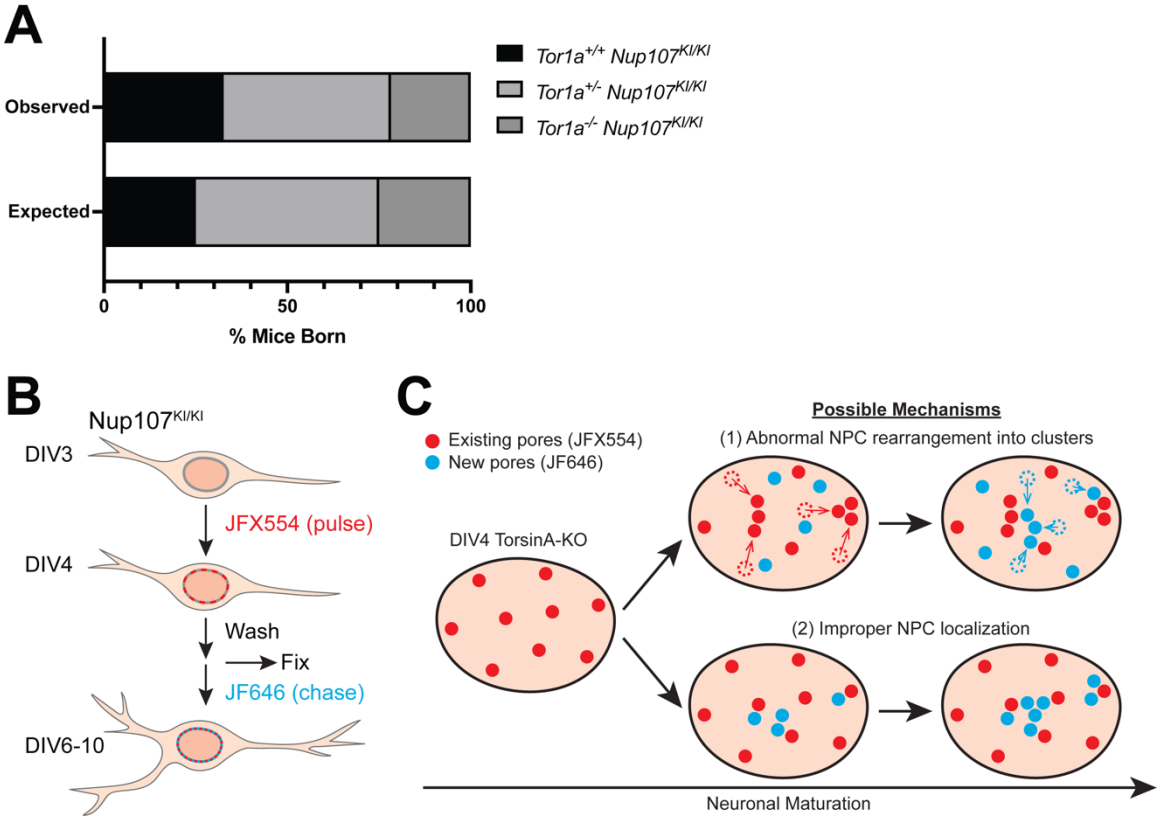


Figure 4.6: Setting up NPC pulse-chase using neurons harboring HaloTag-Nup107 allele

A) Distribution of genotypes in litters derived from intercrossing *Tor1a*$^{+/-}$*; Nup107*$^{KI/KI}$ mice. All genotypes were born at the expected Mendelian ratio (P=0.4880, Chi-squared test). 46 pups from 6 litters were analyzed.

B) Schematic of HaloTag pulse-chase experiment.

C) Diagram of potential mechanisms for NPC clustering in torsinA-KO neurons. In (1), NPCs redistribute after formation, leading to clusters of existing and newly formed NPCs. In (2), sites of NPC biogenesis are mislocalized and clusters exclusively contain new NPCs. Red circles represent existing NPCs (pulse; JFX554). Blue circles represent new NPCs (chase; JF646).

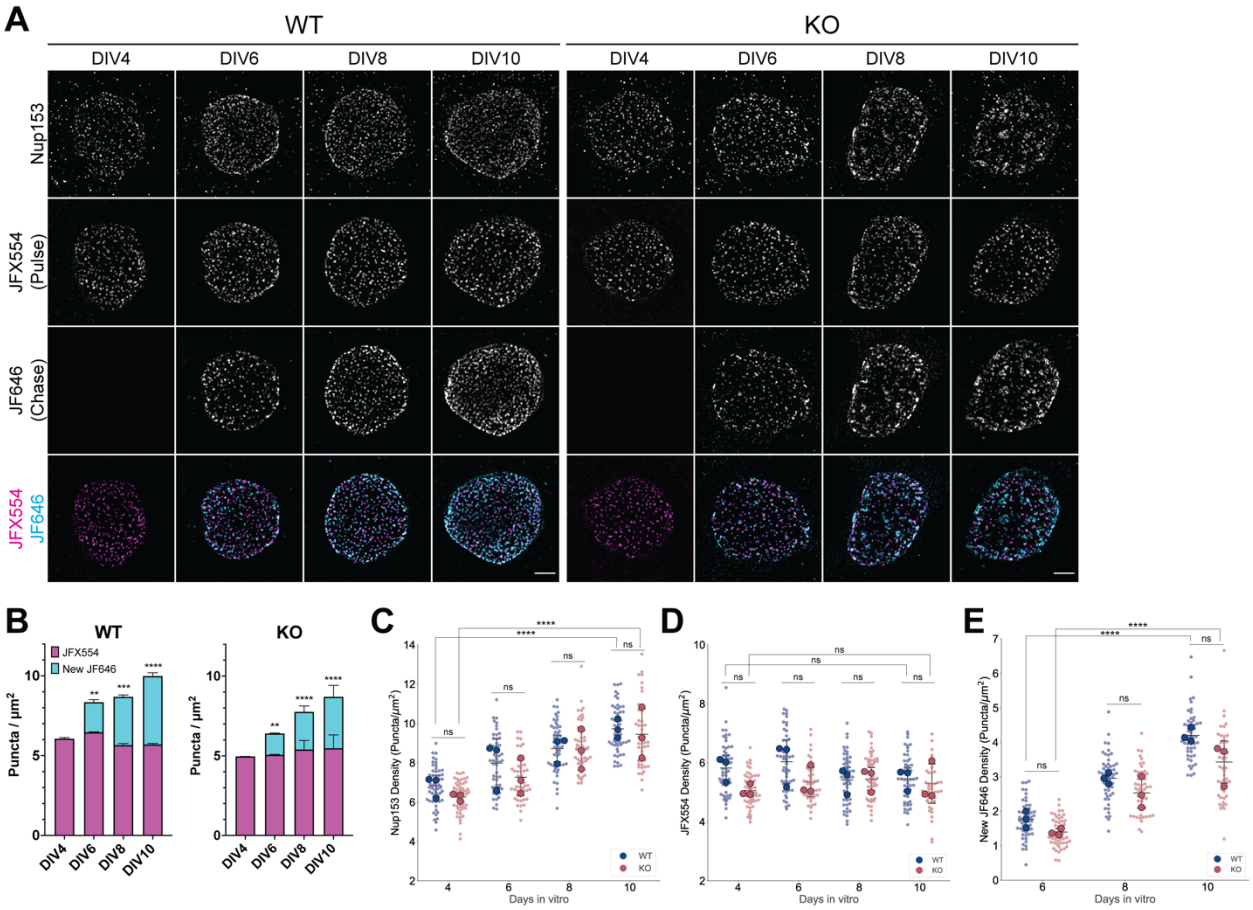


Figure 4.7: Sites of NPC biogenesis are abnormal in torsinA-KO neurons

A) HaloTag pulse-chase SIM images of WT and torsinA-KO neurons. Neurons were stained with anti-Nup153 antibody post-fixation to label the total NPC population. Scale bar = 2µm.

B) Density of JFX554 puncta and new JF646 puncta in DIV 4, 6, 8, and 10 WT and torsinA-KO HaloTag-Nup107 neurons. Plots show mean ± SD. Using DIV4 values as a reference, repeated measures two-way ANOVA with Dunnett's test was performed. **P<0.01, ***P<0.001, ****P<0.0001.

C, D, E) Superplots of Nup153 (C), JFX554 (D), and new JF646 (E) puncta density in maturing WT and torsinA-KO primary neurons aged DIV4, 6, 8, 10. Plots show mean ± SD. Repeated measures two-way ANOVA with Sidak's multiple comparisons test was used to compare genotypes at each timepoint, and no comparisons reached statistical significance. Repeated measures two-way ANOVA with Dunnett's multiple comparisons test was used to compare all timepoints to DIV4, with ****P<0.0001.

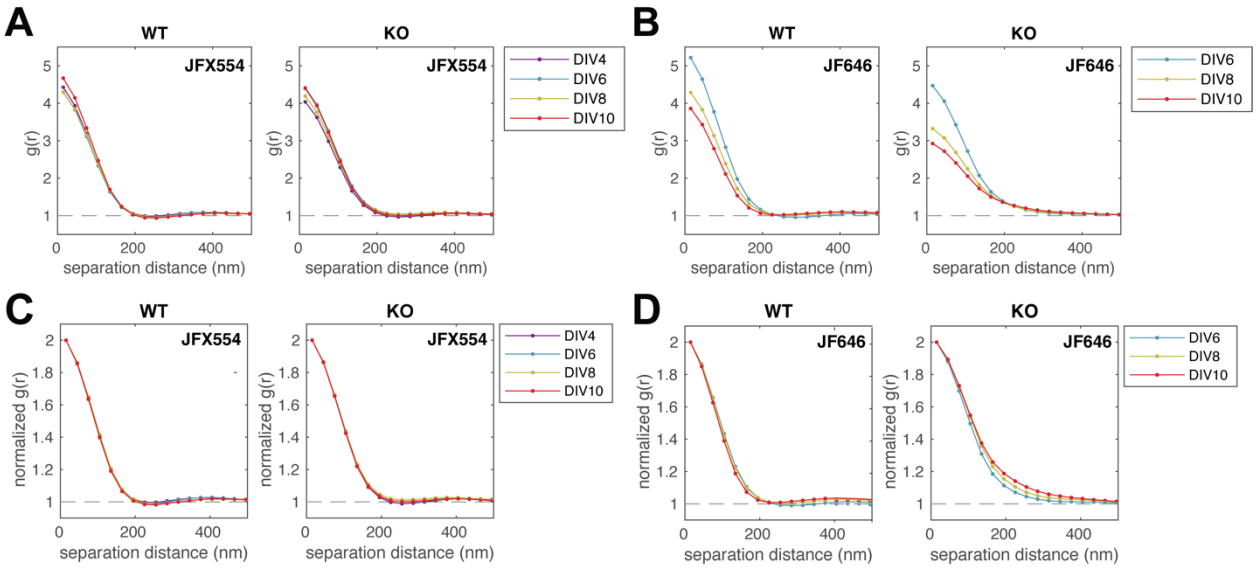


Figure 4.8: NPC spatial distribution analysis from pulse-chase study

A) Autocorrelation of JFX554 images over 0-500nm separation distance. Similar starting amplitudes reflect constant JFX554 density.

B) Autocorrelation of JF646 images over 0-500nm separation distance. Decreasing starting amplitudes over neuronal maturation reflect increasing JF646 density. Broadening of the curve in torsinA-KO neurons indicates spatial correlation of NPCs over larger distances.

C) Normalized autocorrelation of JFX554 SIM images over 0-500nm separation distance. Autocorrelation values <1 around 200nm in both WT and torsinA-KO neurons reflect nonrandom uniform distribution of JFX554-labeled NPCs.

D) Normalized autocorrelation of JF646 SIM images over 0-500nm separation distance. Autocorrelation values >1 in torsinA-KO neurons reflect clustering of NPCs labeled with JF646.

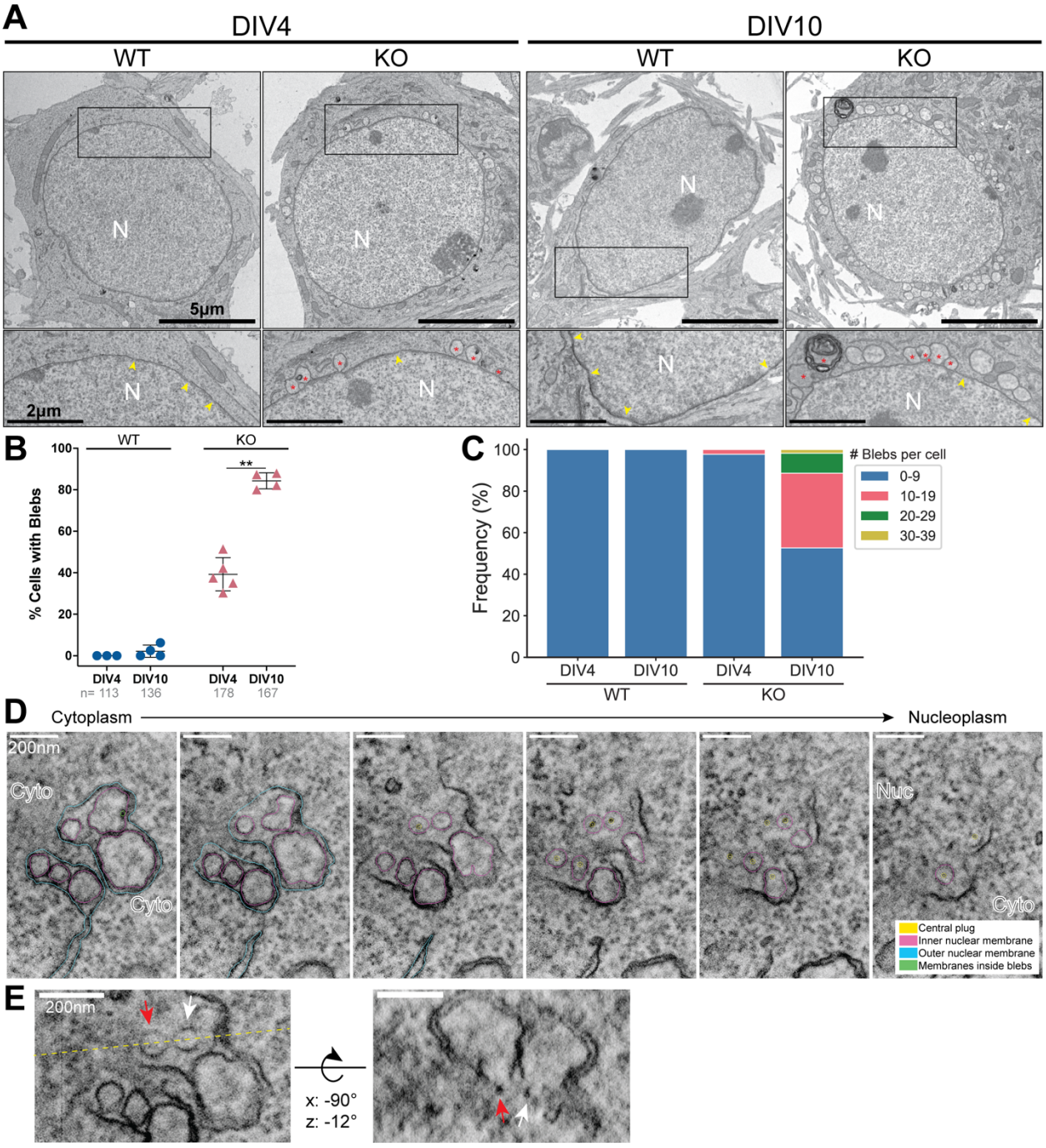


Figure 4.9: NE blebs spatially and temporally coincide with NPC biogenesis

A) Transmission electron microscopy (TEM) images of WT and torsinA-KO neurons at DIV4 and DIV10. N=nucleus. Fully-formed NPCs are marked with yellow arrowheads. NE blebs identified by blinded analysis are marked with red asterisks. Scale bar = 5µm for the top row, 2µm for inset.

B) Quantitation of TEM images. Each point represents the % of cells with at least one NE bleb from each biological replicate. n shows the total number of cells analyzed across all replicates. **P=0.0043, paired t-test.
C) Frequency of NE blebs per cell from all replicates.
D) Slices from a DIV10 torsinA-KO tomogram overlayed with segmented contours of the outer nuclear membrane (cyan), inner nuclear membrane (magenta), membranes inside blebs (green), and central plug of pores (yellow).
E) Rotated view of tomogram in (D) to show an XY view intersecting the center of two blebs at the yellow dashed line. Red and white arrows label pores with central plugs. The rotated view (right) demonstrates that these pores form the base of each bleb.

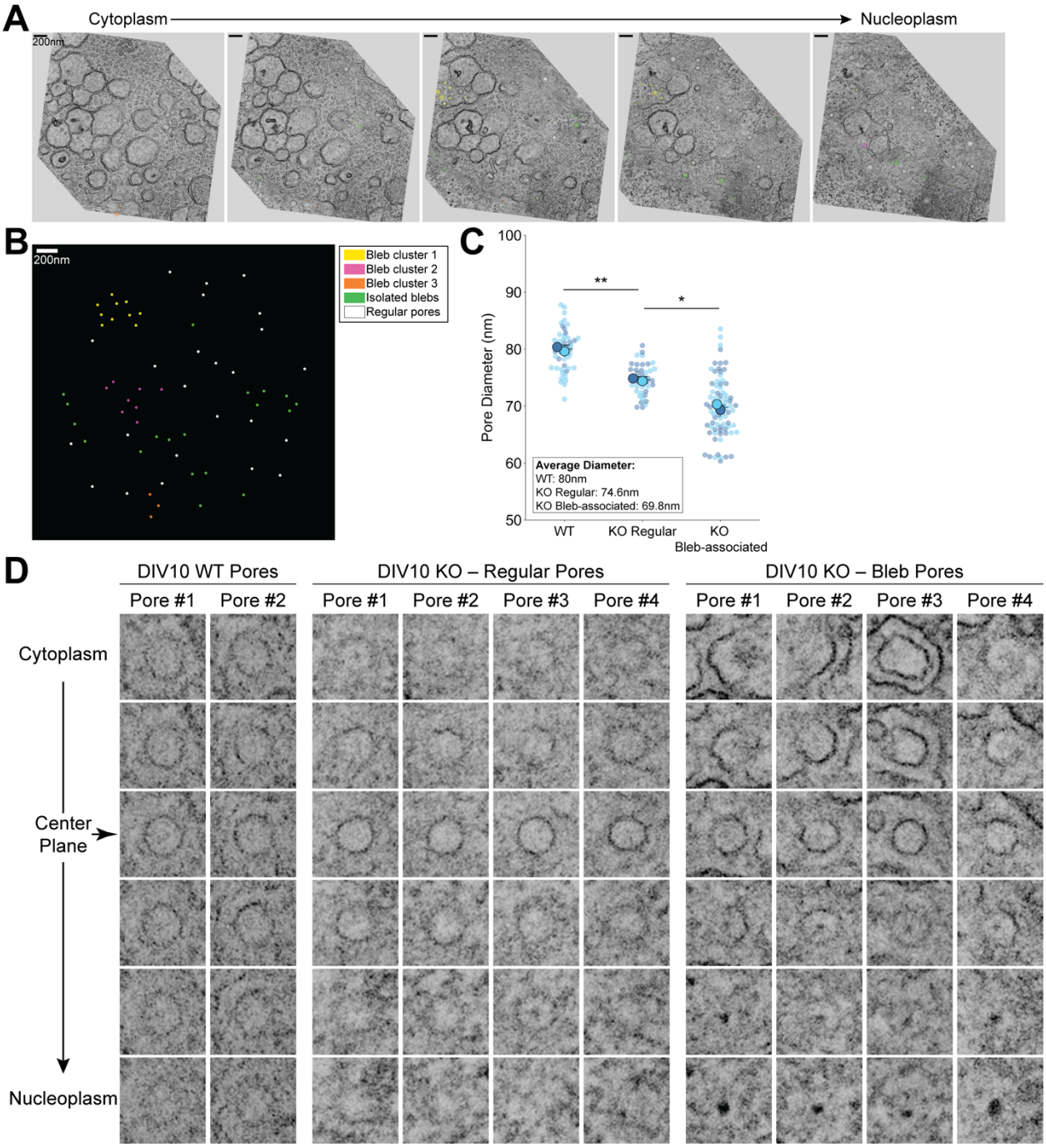


Figure 4.10: Bleb-associated pores are narrow and exhibit nucleoplasmic central plugs

A) Slices from a DIV10 torsinA-KO tomogram oriented as an en-face view of the neuronal nuclear membrane. NPCs localized to clusters of blebs, isolated blebs, or regular NPCs without blebs are marked by color-coded spheres centered around the middle plane of the pore channel, denoted by larger circles.

B) Projection of all marked pores from the tomogram shown in (A).

C) Superplot of WT, KO regular (non bleb-associated), and KO bleb-associated pore diameter (nm). Plots show mean ± SD, with color coding indicative of biological replicates. Swarmplot of individual pore diameters (small points) is overlayed with the mean of pore diameters for each biological replicate (larger points). Pores from two WT and two torsinA-KO tomograms were analyzed. KO regular and bleb-associated pores were identified from the same torsinA-KO tomograms. *P=0.0128, **P=0.0068; unpaired t-test.

D) Slices showing individual pores from DIV10 WT and torsinA-KO tomograms. Regular and bleb-associated torsinA-KO pores were sampled from the same tomogram. From top to bottom, the slices progress from the cytoplasmic side of the pore channel towards the nucleoplasm. Center plane of the pore channel is marked with a horizontal arrow.

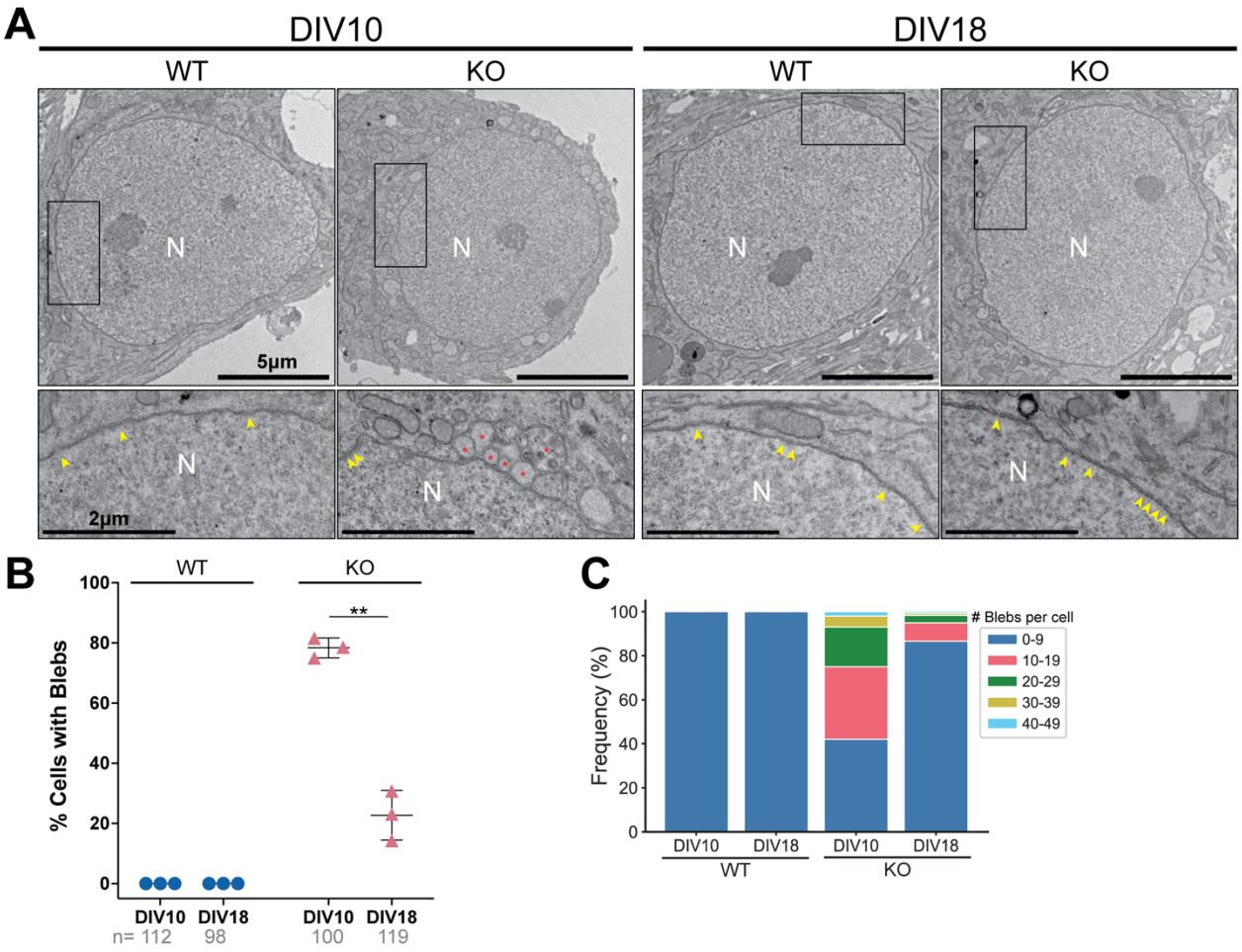


Figure 4.11: NE blebs resolve as neurons continue to mature

A) TEM images of WT and torsinA-KO neurons at DIV10 and DIV18. N=nucleus. Fully formed NPCs are marked with yellow arrowheads. NE blebs identified in blinded analysis are marked with red asterisks. Scale bar= 5µm for the top row, 2µm for inset.

B) Quantitation of TEM images. Each point represents the % of cells with at least one NE bleb from each of 3 biological replicates. n shows the total number of cells that were analyzed across all replicates. **P=0.006; paired t-test.

C) Frequency of NE blebs per cell from all replicates.

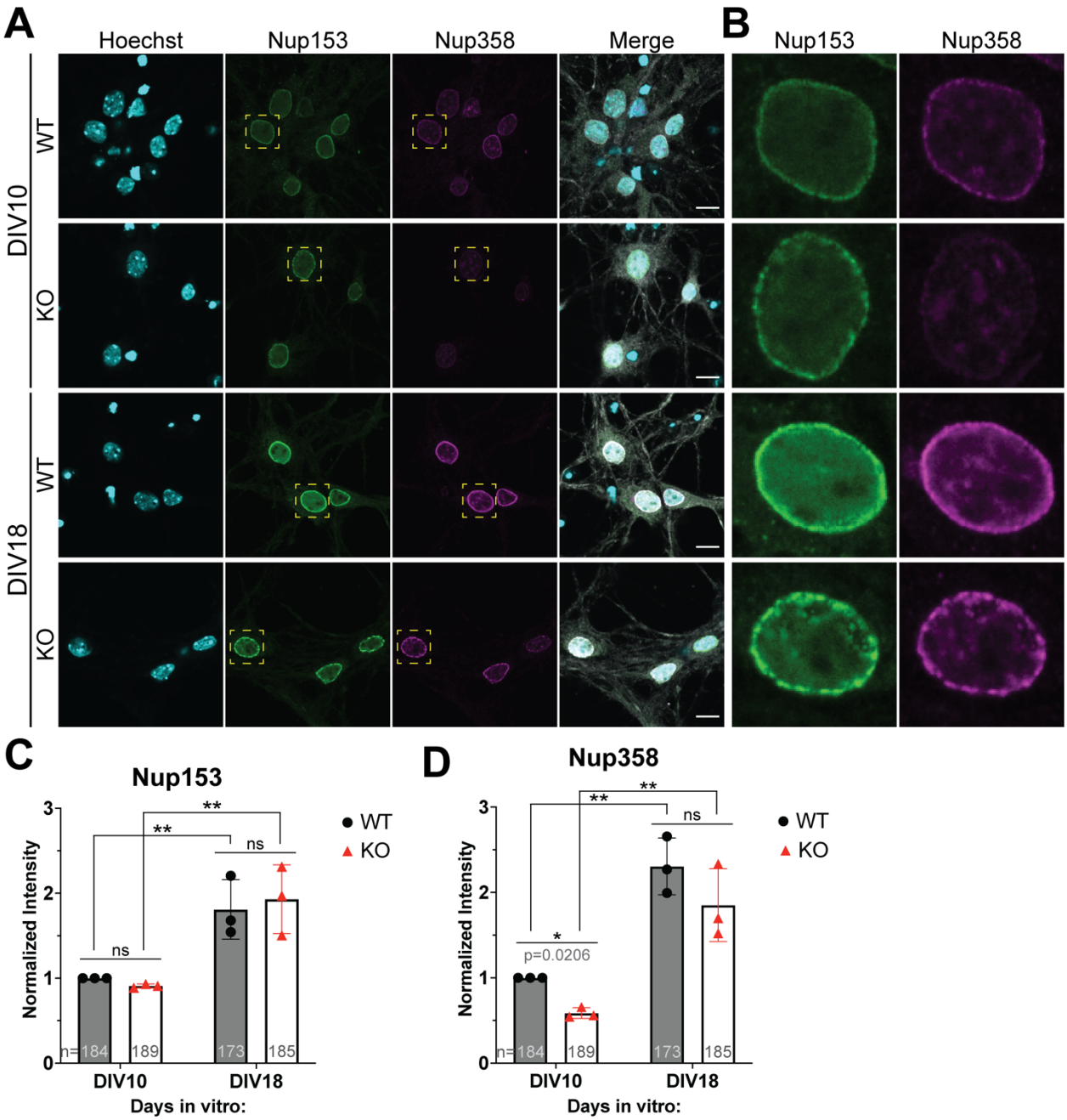


Figure 4.12: NPC assembly completes following NE bleb resolution

A) Confocal images of DIV10 and DIV18 WT and torsinA-KO neurons labeled with Hoechst, Nup153, Nup358, and Map2 (shown in merge). Scale bar = 10μm.
B) Zoomed in view of Nup153 and Nup358 channels of nuclei marked with yellow boxes in (A).
C, D) Normalized Nup153 (C) and Nup358 (D) nuclear rim intensity of DIV10 and DIV18 WT and torsinA-KO primary neurons. ns, not significant; **P <0.01, repeated measures two-way ANOVA with Sidak's multiple comparisons test.

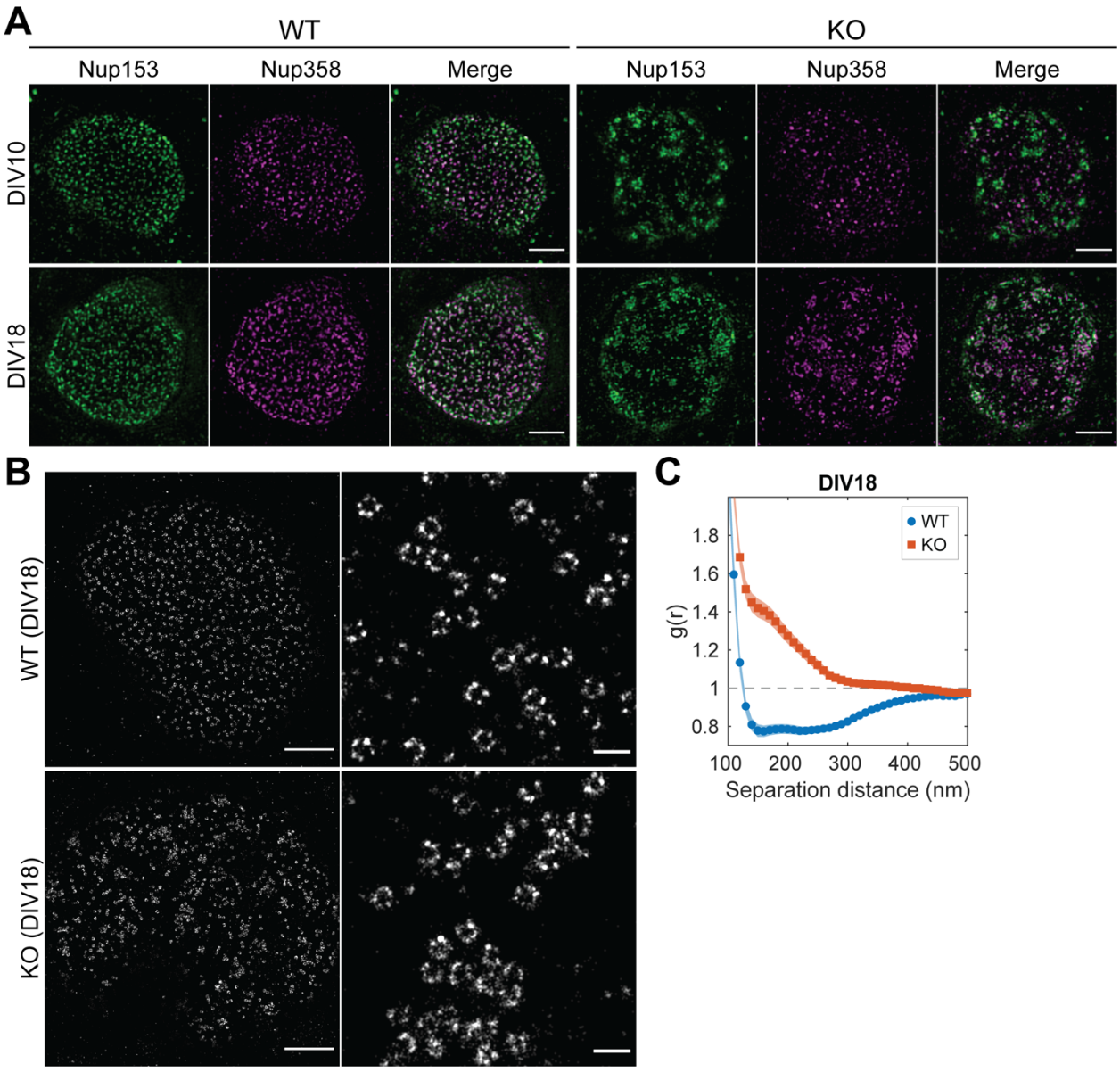


Figure 4.13: Nup358 is recruited to persisting NPC clusters in DIV18 torsinA-KO neurons

A) SIM images of DIV10 and DIV18 WT and torsinA-KO neurons labeled with Nup153 and Nup358 antibodies. Scale bar = 2µm.
B) dSTORM images of Nup210 in DIV18 WT and torsinA-KO neurons. Scale bar = 2nm. Right panels show zoomed in view. Scale bar for right panels = 200nm.
C) Autocorrelation plot of DIV18 WT and torsinA-KO neurons, determined from Nup210 dSTORM images. 18 WT and 17 KO cells from 3 biological replicates were analyzed.

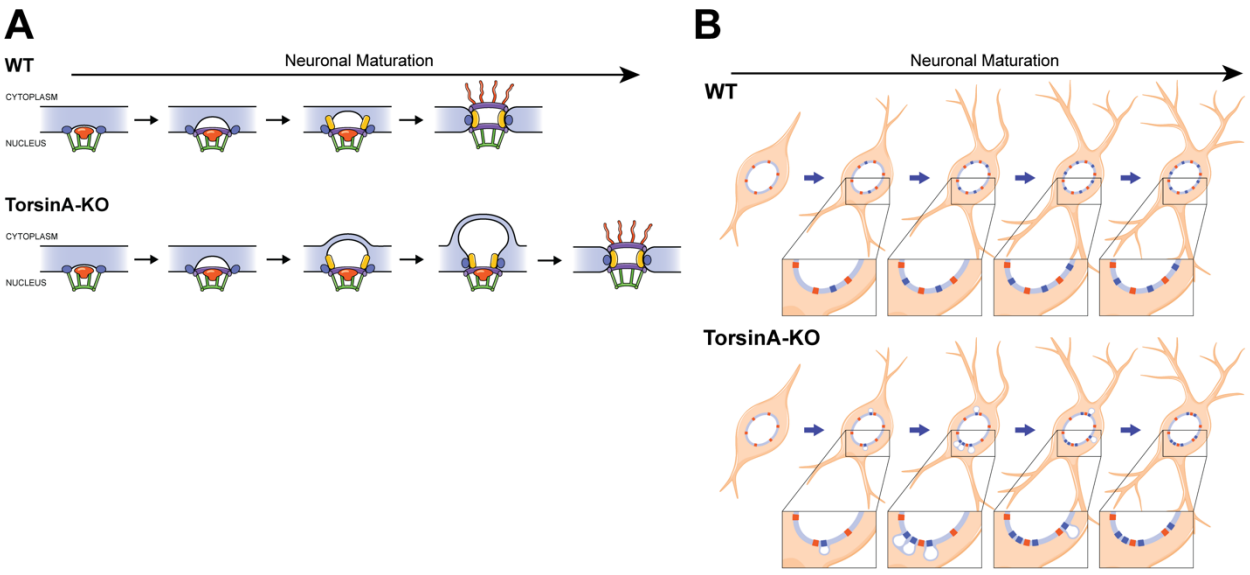


Figure 4.14: Summary of the effects of torsinA loss on NPC spatial organization and dynamics

A) Model of interphase NPC assembly in WT and torsinA-KO neurons. Onset of NPC assembly is not affected by torsinA deletion. Nuclear basket, inner ring, and transmembrane nucleoporins are recruited to the *de novo* NPC as the INM starts to bud. Instead of the normal INM-ONM fusion found in WT neurons, excessive INM extrusion causes NE blebs to emerge and enlarge in torsinA-KO neurons. These blebs stall torsinA-KO NPCs at an intermediate stage while WT NPC assembly completes. As torsinA-KO neurons continue to mature, NE blebs resolve and INM-ONM fusion occurs. Completion of NPC biogenesis is delayed in torsinA-KO neurons.

B) Model of NPC localization in maturing WT (top) and torsinA-KO (bottom) neurons. In WT neurons, newly forming NPCs (blue) localize to empty spaces between existing NPCs (red), thereby maintaining uniform spatial organization. In maturing torsinA-KO neurons, newly forming NPCs (blue) localize abnormally close to each other or to existing NPCs (red), causing aberrant clusters. NPC biogenesis is upregulated in both genotypes and total NPC number is not affected by the absence of torsinA.

Videos can be found at this link:
https://github.com/suminkim/NPC_NE_measurements/tree/main/Movies

Video 1

3D volumetric tomogram of torsinA-KO DIV10 nuclear membrane. Movie starts from the cytoplasm and progresses towards the nucleoplasm. Pores occurring where clusters of blebs, single isolated blebs, or regular NPCs connect to the nuclear membrane are color-coded and annotated.

Video 2

3D volume of the torsinA-KO DIV10 tomogram shown in Figure 4.8D. Inner nuclear membrane (magenta), outer nuclear membrane (cyan), membranes inside the blebs (green), and central plugs of pores (yellow) are segmented.

Chapter 5 Assessing the Critical Temporal Window of TorsinA Function in Developing Neurons

5.1 Abstract

DYT-TOR1A (DYT1) dystonia is a neurodevelopmental movement disorder caused by a loss-of-function mutation in the gene *TOR1A* encoding the protein torsinA. DYT1 manifests early in life, and carriers of the disease-causing mutation who are symptom-free by mid-20s are unlikely to develop the disease, demonstrating the importance of torsinA function during a critical developmental window. The molecular events underlying this temporal requirement for torsinA function is unknown. Based on our identification of upregulated nuclear pore complex (NPC) formation during in maturing neurons, we sought to explore the impact of modulating torsinA levels in discrete temporal windows on NPC biogenesis. We used primary neurons derived from a mouse model in which torsinA expression can be controlled with a tetO promoter. We were unable to induce torsinA expression during neuronal maturation, and suppression of torsinA levels in late-maturing neurons was ineffective, suggesting a poorly understood age-dependent epigenetic mechanism governing neuronal tetO-Tor1a expression. Depletion of torsinA in early maturing neurons derived from pups expressing normal torsinA proved effective, and we found that loss of torsinA exclusively during *in vitro* neuronal maturation is sufficient to cause abnormal NPC cluster formation. These findings indicate that NPC abnormalities observed in mature neurons lacking torsinA arise exclusively during neuronal maturation. Our studies also suggest that locus-specific epigenetic modulators of TetO-based transcription must be considered in future studies to alter torsinA levels in cultured neurons.

5.2 Introduction

DYT1-TOR1A (DYT1) dystonia is a movement disorder caused by a mutation in the *TOR1A* gene that leads to a single glutamic acid residue deletion (ΔE) in the AAA+ protein torsinA[79]. DYT1 is incompletely penetrant, with only approximately 30% of carriers developing symptoms[180,181]. Symptom onset occurs in childhood-adolescence, typically between 6-12 years of age. Notably, carriers of the ΔE disease mutation that do not develop symptoms until the age of 26 remain symptom-free for life[82], suggesting the existence of a critical period of vulnerability to torsinA loss of function. Critical periods are discrete windows during which the developing nervous system is susceptible to insults that can disrupt neural function long term. During critical periods, the developing CNS may be receptive to therapeutics that are otherwise not effective. The molecular events underlying critical periods, including that of DYT1 pathophysiology, remain unknown.

Critical periods have been examined in both healthy development and in neurodevelopmental diseases[179]. The visual system is a well-studied example of a critical period in normal development: visual deprivation in young animals causes persisting visual dysfunction whereas the same deprivation in adult animals has little effect[182]. Critical periods have also been examined in Angelman syndrome, which is caused by dysfunction of the protein Ube3a, and SYNGAP-1 (synaptic Ras GTPase-activating protein 1)-related intellectual disability[183,184]. In both contexts, deletion of the disease-relevant proteins in an early developmental window results in deficits that are not observed by deletion of the same proteins in adulthood. More recently, critical period of CNS vulnerability to torsinA loss-of-function (LOF) was examined using a mouse model that enables spatiotemporal control of torsinA expression[118]. Embryonic knockdown of torsinA in forebrain inhibitory and cholinergic neurons causes dystonia-like behavioral and

neuropathological phenotypes while torsinA knockdown in adult mice has no apparent abnormalities. Neurons without torsinA expression from E0 also appear to exhibit abnormal NPC clustering that is not observed in adult knockdown of torsinA. Aberrant motor phenotypes in juvenile mice lacking torsinA expression were rescued by restoring torsinA expression, but torsinA restoration in adult mice with stable symptoms had no effect. These studies establish that torsinA function is uniquely required in an early neurodevelopmental critical period and that circuit maturation and neural function past this window are independent of torsinA.

Here, we explore whether nuclear pore complex (NPC) biogenesis underlies the critical period of torsinA function. We derive and culture primary neurons from genetically engineered mice that enable tetracycline operator (tetO)-mediated temporal control of torsinA expression. Inducing torsinA expression in *in vitro* maturing neurons proved challenging, as was suppressing torsinA levels in mature neurons. We depleted torsinA in early maturing neurons derived from pups expressing normal torsinA and found that suppressing torsinA exclusively during the window of active NPC biogenesis causes abnormal NPC localization. These findings indicate that NPC abnormalities observed in mature neurons lacking torsinA arise exclusively during early postnatal neuronal maturation, suggesting that the NPC biogenesis is a discrete developmental period that requires torsinA function. Our studies also suggest that epigenetic regulation of the tetO locus must be considered in future studies to manipulate torsinA levels in cultured neurons.

5.3 Results

5.3.1 A TetO-Tor1a mouse line to modulate torsinA expression

To explore the impact of modulating torsinA modulation in distinct temporal windows, we established a mouse line in which torsinA expression can be induced or suppressed by addition or withdrawal of a tetracycline. A tetracycline operator (tetO) was inserted upstream of the

endogenous *Tor1a* locus to create mice harboring an endogenous tetO-Tor1a allele[118,185]. Expression of a tetracycline-controlled transcriptional silencer (tTS) in combination with the tetO-Tor1a system allows for modulation of torsinA expression. In the absence of a tetracycline, *Tor1a* expression is blocked due to tTS binding to tetO (Figure 5.1A, top). Addition of a tetracycline such as doxycycline results in sequestration of tTS away from tetO, enabling *Tor1a* expression (Figure 5.1A, bottom). We tested whether torsinA expression can be modulated with this system as expected. We prepared cortical lysates from P0 pups homozygously harboring the tetO-Tor1a alleles and expressing tTS from cages with regular chow or doxycycline chow and analyzed torsinA levels by western blot. As expected, P0 pups from breeders on doxycycline chow expressed torsinA while pups bred on regular chow did not (Figure 5.1B). This validates that *in vivo*, our tetO-Tor1a/tTS system allows for doxycycline-dependent torsinA induction, similar to previous reports[118].

5.3.2 TorsinA expression cannot be induced in maturing primary neurons

To assess the link between torsinA and NPC biogenesis in early- and late-maturing neurons, we sought to compare the effects of torsinA expression during and past the window of active NPC formation. We attempted to induce torsinA expression in cultured primary cortical neurons derived from pups born to tetO-Tor1a breeders on regular chow (not expressing torsinA). We isolated neurons from tetO/+ (heterozygous tetO-Tor1a; without tTS), tetO/+ tTS (heterozygous tetO-Tor1a; with tTS), and tetO/tetO tTS (homozygous tetO-Tor1a; with tTS) mice and grew the neurons in regular media or media containing 2μg/mL doxycycline. We harvested neurons at DIV10 and assessed torsinA levels by western blotting. As expected, tetO/+ and tetO/+ tTS neurons grown in regular media expressed torsinA while tetO/tetO tTS neurons did not. However, the presence of doxycycline for 10 days in culture did not have an impact on torsinA

expression. No increase in the torsinA expression was observed in tetO/+ tTS neurons grown in doxycycline-containing media, and torsinA expression was absent in tetO/tetO tTS neurons regardless of doxycycline (Figure 5.2A). We asked whether the lack of torsinA induction is post-transcriptional or due to transcriptional inhibition. We conducted qRT-PCR analyses of tetO/tetO tTS and tetO/+ tTS DIV10 neurons, with WT (*Tor1a*$^{+/+}$) and torsinA-KO (*Tor1a*$^{-/-}$) neurons from DIV4 and DIV10 as controls (Figure 5.2B, C). We conducted these experiments twice, using different RNA isolation methods to ensure our findings are reproducible. TorsinA transcript expression was robust in WT neurons and undetectable in torsinA-KO neurons (Figures 5.2B, C). WT neurons expressed higher levels of torsinA transcripts at DIV10 compared to DIV4, contrary to what may be expected from decreasing torsinA protein levels in the developing mouse brain[95]. The two RNA isolation methods yielded slightly different results for DIV10 tetO/+ tTS neurons grown in regular media: using RNeasy RNA isolation, torsinA transcript levels in tetO/+ tTS were approximately half of that of WT DIV10 neurons (Figure 5.2B); with the Direct-zol isolation, similar or higher levels of transcripts was observed in tetO/+ tTS neurons compared to WT (Figure 5.2C). As expected, low levels of torsinA transcripts were observed in tetO/tetO tTS neurons grown in regular media in both methods. Doxycycline had no impact in tetO/+ tTS and tetO/tetO tTS neuronal torsinA transcript levels, suggesting that tetO-mediated transcription is inhibited regardless of tTS regulation. Consistent with lack of torsinA induction in maturing cultured primary neurons, NPC clustering was observed in tetO/tetO tTS neurons, and perinuclear Ub-K48 accumulation, which is also present in DIV10 torsinA-KO neurons,[75] was additionally observed (Figure 5.2D). The proportion of tetO/tetO tTS cells exhibiting these abnormal phenotypes was similar regardless of the presence of doxycycline (Figure 5.2E, F), further demonstrating that 10 days of doxycycline treatment in maturing primary neurons is not sufficient to induce torsinA

expression. These data suggest that a poorly understood epigenetic mechanism may be inhibiting transcription activation of the tetO-Tor1a locus in cultured primary neurons.

5.3.3 Loss of torsinA exclusively in maturing neurons causes abnormal NPC clustering

We next explored whether torsinA expression could be suppressed in maturing cultured primary neurons derived from pups with torsinA expression (cages with doxycycline chow). We isolated neurons from +/+ tTS, tetO/+ tTS, and tetO/tetO tTS pups with torsinA expression (validated in Figure 5.1B). Neurons were either grown in media with doxycycline to maintain torsinA levels or in regular media to suppress torsinA expression until DIV10. Gene dose-dependent reduction in torsinA levels was observed: modest reduction in torsinA band intensity was observed in tetO/+ tTS neurons in regular media, and torsinA expression was completely abolished in tetO/tetO tTS neurons grown in regular media (Figure 5.3A). As expected, doxycycline had no effect on torsinA expression in +/+ tTS controls that do not harbor a tetO-Tor1a allele. Based on our previous characterization of NPC biogenesis upregulation starting DIV4 in maturing neurons (Chapter 3) and NPC abnormalities arising between DIV4 and DIV10 in torsinA-KO neurons (Chapter 4), we asked whether torsinA levels are sufficiently suppressed by DIV4 in the absence of doxycycline. Western blot analysis showed that the majority of torsinA is indeed degraded by DIV4, consistent with a previously reported half-life of 80h for torsinA[186] (Figure 5.3B). These data demonstrate that torsinA can be suppressed in early maturing neurons by withdrawing doxycycline and indicate the suitability of this system to examine the role of torsinA on NPC biogenesis in maturing neurons.

We hypothesized that DIV10 tetO/tetO tTS neurons grown in normal media would exhibit abnormal NPC clusters since torsinA is mostly degraded by DIV4, when active NPC assembly appears to begin. We again isolated tetO/+ tTS and tetO/tetO tTS neurons from doxycycline fed

P0 pups and grew them in media with or without doxycycline. Neurons were subsequently fixed at DIV10 and labeled with Nup210 or Nup153 antibodies. Confocal imaging demonstrated clear NPC clustering in tetO/tetO tTS neurons grown in regular media (Figure 5.3C-E). None of the other conditions, including tetO/+ tTS neurons in regular media (torsinA heterozygous expression) and tetO/tetO tTS neurons in doxycycline media (torsinA expression maintained) exhibited clustering. These data demonstrate that loss of torsinA exclusively during upregulated NPC formation results in abnormally distributed NPCs and suggest that NPC biogenesis may be a process that specifically requires torsinA function in a discrete temporal window.

5.3.4 TorsinA suppression is ineffective later maturing neurons

To further examine whether NPC biogenesis is a critical window of torsinA function, we sought to address whether deletion of torsinA in mature neurons affects NPC distribution. We hypothesized that knockdown of torsinA would have little to no effect past the window of active NPC formation. Since four days of doxycycline withdrawal from DIV0 to DIV4 was sufficient to significantly reduce torsinA levels (Figure 5.3B), we expected that starting doxycycline withdrawal at DIV14 would reduce torsinA levels by DIV18, when NPC formation appears to plateau (Chapter 3). We isolated and grew tetO/+ tTS and tetO/tetO tTS neurons from pups on doxycycline chow and maintained cultures in doxycycline media until DIV14, at which point half of the cultures were switched to regular media. Surprisingly, removal of doxycycline from DIV14 to DIV24 did not result in reduction in torsinA protein levels (Figure 5.4A). To test whether earlier doxycycline withdrawal may lead to more efficient torsinA knockdown, we started doxycycline removal at DIV10 and assessed torsinA levels at DIV20. TorsinA levels remained normal in both genotypes (Figure 5.4B), similar to the results of DIV14-24 withdrawal. We validated that the lack of torsinA reduction is not due to residual doxycycline in the media by adding an additional wash

step before switching to regular media on DIV10, and still observed no effect on torsinA levels (Figure 5.4C). qRT-PCR revealed a slight reduction in torsinA transcript levels in tetO/+ tTS and tetO/tetO tTS grown in regular media from DIV10 to DIV20, indicating that doxycycline withdrawal did inhibit transcription to a small degree (Figure 5.4D). Based on the estimated 80h torsinA half-life, this transcriptional inhibition was likely not sufficient to significantly reduce torsinA protein levels. Together, these data indicate that modulating torsinA levels with the tetO-Tor1a system is time-dependent, with much more inefficient transcriptional inhibition in mature neurons (DIV10 or DIV14) compared to neurons that are freshly isolated (DIV0).

5.4 Discussion

These studies are the first to examine whether the upregulated NPC biogenesis is a molecular event underlying the critical period of torsinA function. Our results demonstrate that loss of torsinA between DIV4 and DIV10, during which active NPC formation occurs, is sufficient to cause aberrant NPC distribution. This finding is consistent with the role of torsinA in determining nascent NPC localization demonstrated in the previous chapter. We additionally report the time-dependency of modulating torsinA expression using the tetO/tTS system. These data suggest that consideration of epigenetic regulation of the tetO promoter may be required in future studies to more acutely induce or inhibit torsinA expression.

The tetO-Tor1a system has been used successfully in *in vivo* studies to modulate torsinA expression[118]. Mice in which torsinA is absent in forebrain inhibitory neurons starting at E0 (embryonic day 0) develop abnormal motor phenotypes, but deletion of torsinA in the same neurons during adulthood by withdrawing doxycycline from P70-P250 has no effect, establishing an early developmental critical window of torsinA function[118]. The same critical period also represents a potential window of therapeutics, since restoring torsinA levels with doxycycline

chow from P21 to P70 resolves motor phenotypes (which emerge around P14) whereas these deficits persist if torsinA is induced between P70 and P250. Suppression or induction of torsinA in these studies were conducted over several weeks, in stark contrast to our 10-day doxycycline addition or withdrawal in neuron cultures. The lack of torsinA induction by growing neurons in doxycycline media from DIV0 to DIV10 indicates two possibilities that are not mutually exclusive: 1) tTS-independent epigenetic silencing of the tetO promoter in cultured neurons and 2) insufficient duration of doxycycline treatment. Synthetic Tet promoters have been reported to be susceptible to epigenetic silencing[187,188] such as methylation[189]. Targeted demethylation of the Tet promoter has been shown to allow reactivation of expression[189] and may aid efficient induction of torsinA in the tetO-Tor1a system. Given successful torsinA induction in P21-P70 doxycycline-fed mice without any epigenetic modifiers[118], it may be possible to induce torsinA expression by continuing to grow neurons in doxycycline media past DIV10. However, this approach is likely unsuitable to elucidate the temporal requirement of torsinA in NPC biogenesis, as the time required to induce torsinA expression may be longer than the duration of active NPC formation.

Our data suggest a clear time-dependence on efficiency of torsinA suppression. TorsinA knockdown with doxycycline withdrawal starting at DIV0 was efficient and resulted in significant depletion by DIV4. However, attempts to reduce torsinA expression starting at DIV10 or DIV14 proved ineffective. Although we did not observe any visible changes in torisnA protein levels upon DIV10-20 doxycycline withdrawal, our qRT-PCR data indicate that torsinA transcript levels are somewhat reduced. Given the estimated 80h half-life of torsinA, it is possible that significant depletion of torsinA protein may be achieved by maintaining neurons in regular media for a longer duration.

Our torsinA knockdown experiment in early-maturing neurons (DIV0–10) clearly demonstrate that NPC abnormalities arise exclusively during neuronal maturation, supporting the findings in Chapter 4. These neurons were isolated from torsinA-expressing pups and a low level of torsinA expression is still observed at DIV4, excluding any possibility that the absence of torsinA during embryonic development or in the first four days of *in vitro* maturation contributes to aberrant NPC distribution. This finding is also consistent with normal NPC distribution observed in DIV4 torsinA-KO neurons, indicating that mechanisms that lead to normal NPCs present in DIV4 are independent of torsinA. Although suppression of torsinA past the window of NPC biogenesis is necessary to conclude whether torsinA is exclusively required during active neuronal NPC formation, our results clearly demonstrate that torsinA deletion exclusively between DIV4 and DIV10 leads to abnormal NPC localization, highlighting the critical function of torsinA during active neuronal NPC biogenesis.

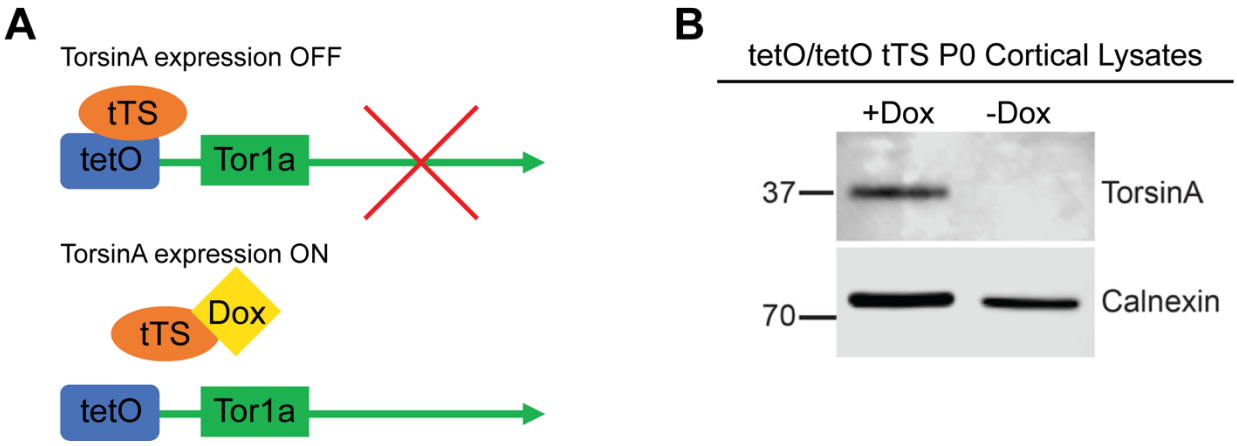


Figure 5.1: Validation of tetO-Tor1a system

A) Schematic of the tetO-Tor1a system with tTS. tTS binds tetO and suppresses Tor1a expression. Addition of doxycycline sequesters tTS from the tetO promoter and allows for Tor1a expression.

B) Western blot of torsinA levels in the cortex of P0 tetO/tetO tTS pups born in cages with torsinA expression (doxycycline chow; +Dox), or torsinA suppression (regular chow; -Dox). Calnexin is shown as the loading control.

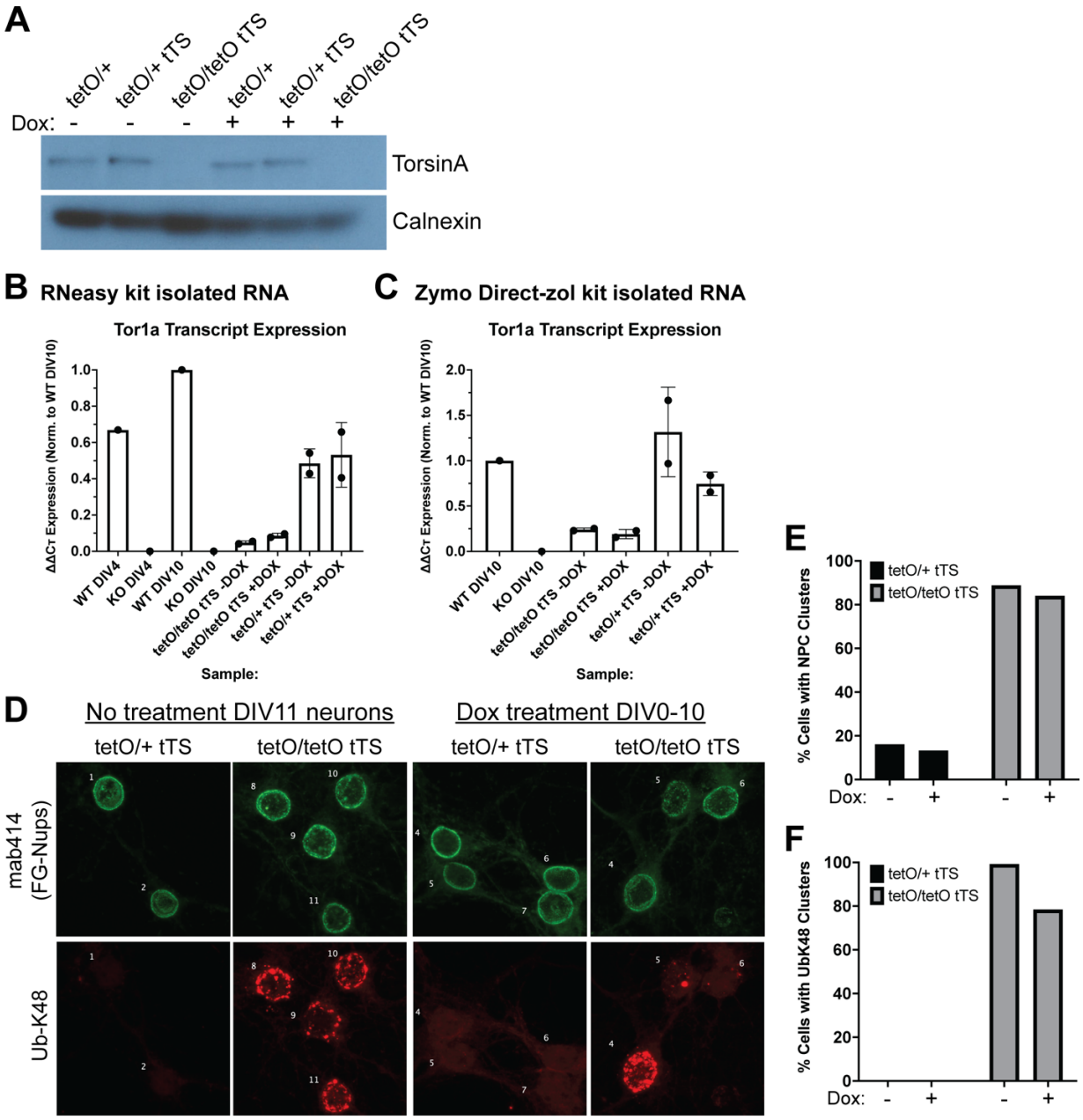


Figure 5.2: Doxycycline treatment does not induce torsinA expression in maturing primary neurons

A) Western blot of torsinA levels in DIV10 neurons with or without doxycycline from DIV0. Neurons were derived from pups born in cages with regular chow (suppressed tetO-Tor1a expression). Calnexin is shown as the loading control.

B, C) qRT-PCR of Tor1a transcript levels using RNA isolated with two different kits (B, RNeasy kit; C, Direct-zol kit). Fold change was calculated by normalizing to full torsinA expression (WT DIV10 neurons). Each point represents an independent biological sample.

D) Confocal images of primary neurons labeled with mab414 (FG-Nups) and Ub-K48 antibodies. All neurons were derived from pups born in cages with regular chow.

E, F) Quantitation of % of cells with NPC clusters (E) and Ub-K48 clusters (F) based on the confocal images. The mean of cells from one biological sample is shown.

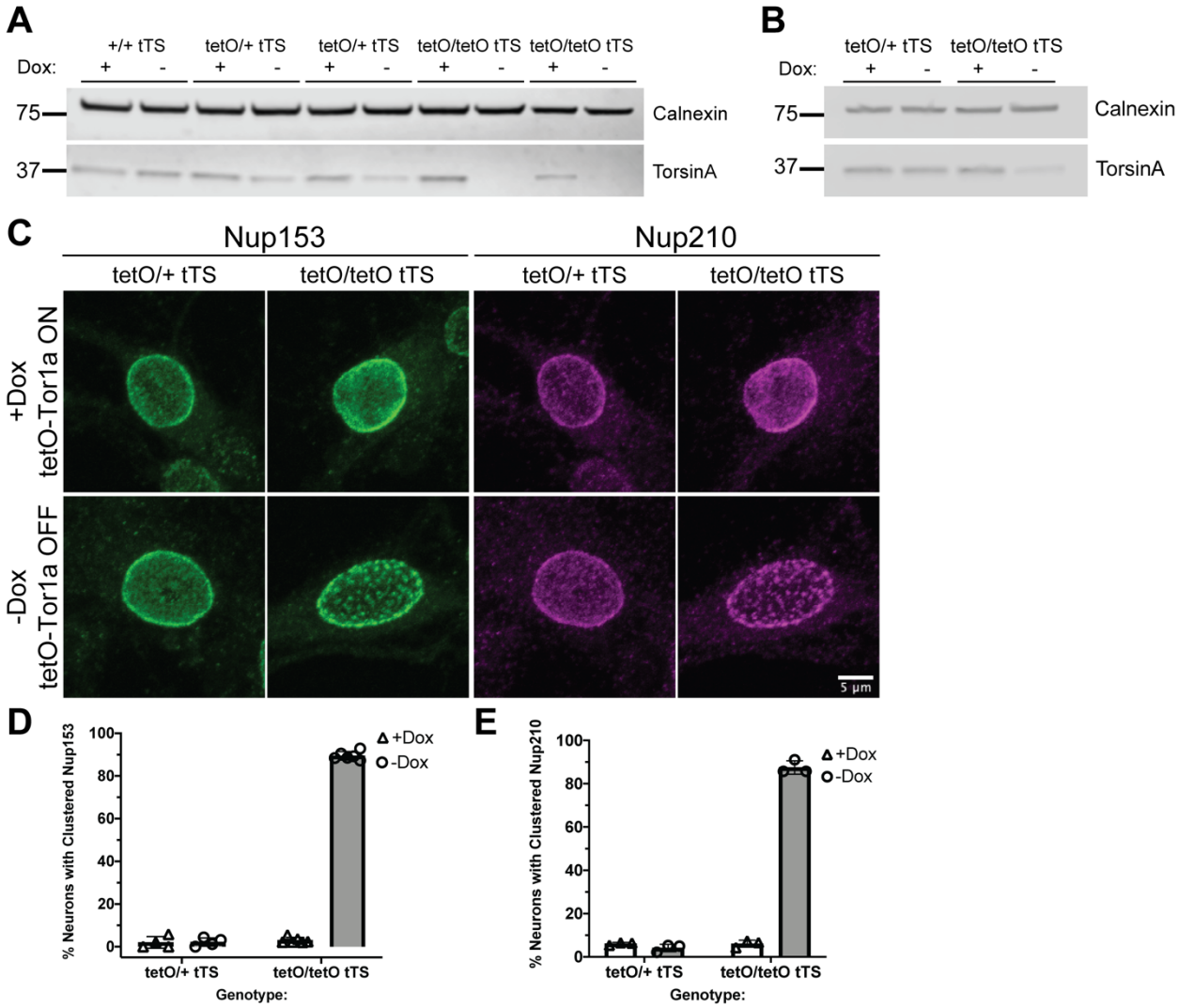


Figure 5.3: Loss of torsinA exclusively during neuronal maturation causes abnormal NPC clustering

A) Western blot of torsinA levels in DIV10 neurons with or without doxycycline beginning DIV0. Neurons were derived from pups born in cages with doxycycline chow (active tetO-Tor1a expression). Calnexin is shown as the loading control. Withdrawing doxycycline between DIV0-10 results in loss of torsinA expression.

B) Western blot of torsinA levels in DIV4 neurons with or without doxycycline beginning DIV0. Neurons were derived from pups born in cages with doxycycline chow (active tetO-Tor1a expression). Calnexin is shown as the loading control. TorsinA expression is significantly decreased in four days of doxycycline withdrawal.

C) Confocal images of primary neurons labeled with Nup153 and Nup210 antibodies. All neurons were derived from pups born in cages with Doxycycline chow, and were growing in media with or without doxycycline between DIV0-10.

D, E) Quantitation of % of cells with Nup153 clusters (D) and Nup210 clusters (E) based on the confocal images. N=3 or 4 animals per condition; each point represents an independent biological replicate. Error bars represent SD between the replicates.

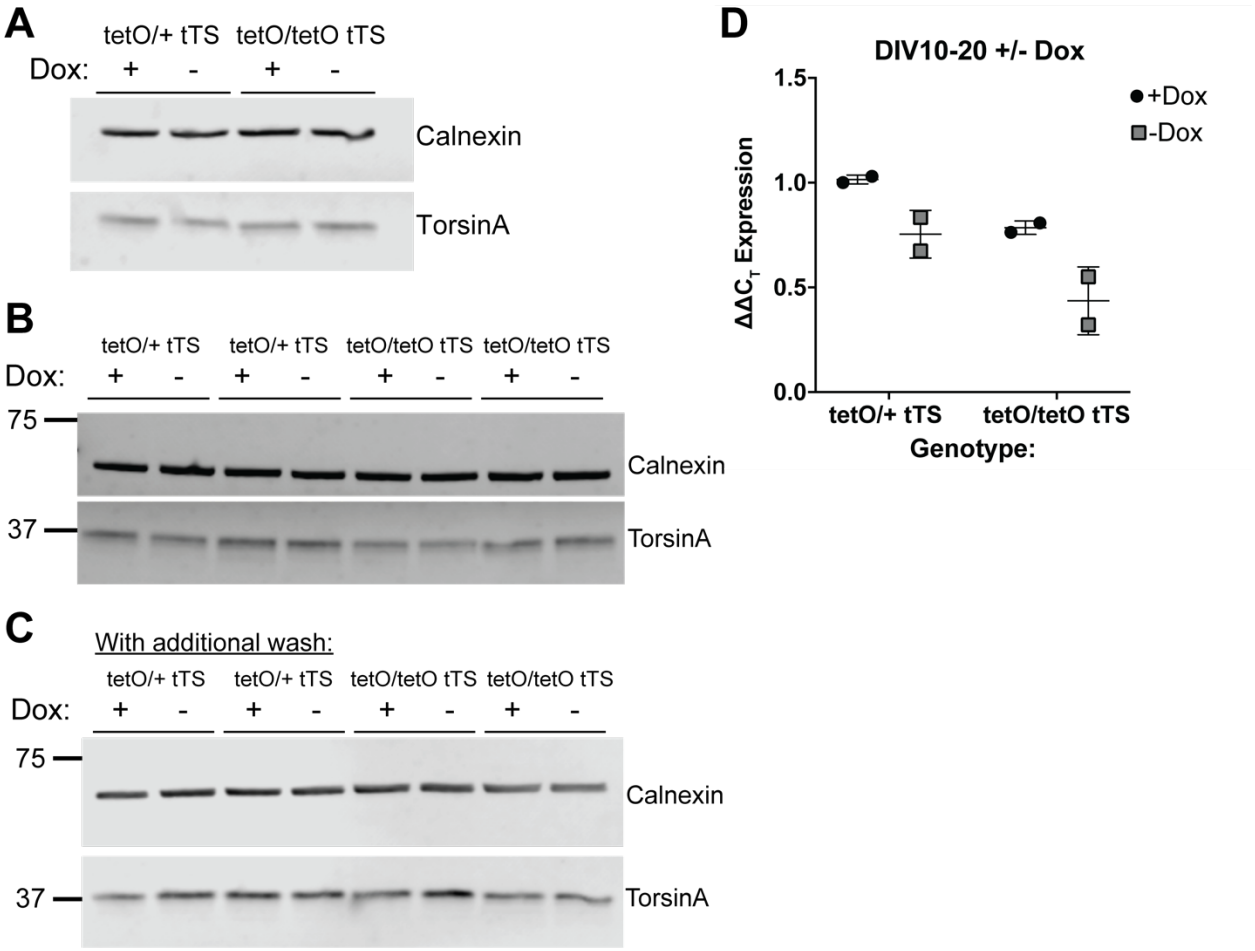


Figure 5.4: Removal of doxycycline in mature primary neurons is not sufficient to knock down torsinA expression

A) Western blot of torsinA levels in DIV24 neurons with or without doxycycline from DIV14. Neurons were derived from pups born in cages with regular chow and grown in media containing doxycycline until DIV14, when half of the wells containing neurons were switched to regular media.

B, C) Western blot of torsinA levels in DIV20 neurons with or without doxycycline from DIV10. Neurons were derived from pups born in cages with doxycycline chow (active tetO-Tor1a expression) and grown in media containing doxycycline until DIV10. (B), neurons were immediately switched to regular media; (C), residual doxycycline was washed out prior to incubation in regular media. Calnexin is shown as the loading control.

D) qRT-PCR of Tor1a transcript levels in neurons grown with or without doxycycline between DIV10-20. Neurons were derived from pups in doxycycline cages and grown in doxycycline-containing media until DIV10. Fold change was calculated by normalizing to torsinA transcript levels in DIV20 tetO/+ tTS neurons grown in doxycycline-containing media. Each point represents an independent biological replicate.

Chapter 6 Discussion and Future Directions

Since their initial observation in 1950[190], our understanding of nuclear pore complexes (NPCs) has greatly improved with the advancement of new technology. Yet, many fundamental questions regarding their regulation, function, and dynamics remain. A growing number of reports implicating NPC abnormalities in neurological diseases[72–76,78,133] highlight the particular importance of NPCs in neurons. Using a combination of mouse models and modern imaging and *in vitro* culturing techniques, the studies presented in this thesis identify neuronal maturation as a new, previously uncharacterized context of physiological NPC biogenesis. Neuronal NPC formation is explored in depth in the context of a neurodevelopmental disease, DYT-TOR1A (DYT1) dystonia, which is caused by torsinA dysfunction in a distinct critical neurodevelopmental window. Our work demonstrates that torsinA coordinates nascent NPC localization, identifying for the first time a single, non-nucleoporin determinant of NPC spatial organization. These data also suggest that neuronal NPC biogenesis is a process that may represent a unique vulnerability to insult during neuronal maturation.

This chapter discusses remaining questions pertaining to NPC regulation, spatial organization, and dynamics in the context of fundamental cell biology and DYT1 pathophysiology. Potential approaches to address these questions are discussed.

6.1 Regulation of NPC number

How NPC number is regulated is largely unknown despite a series of studies in the 1970s and 1980s to examine correlations between basic cellular processes and NPC density. These

studies found no correlation between NPC number and genome size, nuclear size, and nuclear surface area[56,60]. Inhibiting DNA replication and ribosomal synthesis did not impact nuclear growth or NPC formation in interphase HeLa cells[55]. NPC number decreases concomitantly with reduced RNA synthesis in differentiating chick erythroblasts[56], and phytohemagglutinin-activated lymphocytes upregulate NPC density along with increased DNA and RNA synthesis[48], correlating NPC number with demand on nucleocytosolic transport. Since protein levels are increased during early neuronal maturation[138], the robust increase in total NPC density observed in our studies is likely triggered to support increased demand on nuclear transport. Indeed, NPC density decreases in adult mouse cortex past the period of synaptogenesis and circuit formation[59]. Still, future studies to modulate the demand on NPC transport flux by modulating transcriptional activity and protein transport are necessary to begin to explore how NPC number is regulated. Transcription may be modulated using exogenous DNA or by activation with hormones, and optogenetically controlled translocation of overexpressed proteins could be used to alter protein transport flux. If NPC number is indeed dependent on transcription, exploring chromatin reorganization may offer a mechanistic explanation as the chromatin interacts with elements at the nuclear periphery such as lamins[191,192] and NPC nuclear basket subunits[25,28], which also interact with transcription machinery[22]. Additionally, kinases may be involved in the NPC upregulation pathway since Cyclin-dependent kinase (Cdk) 1/2 inhibition blocks nascent NPC formation in interphase HeLa cells[36] and the nuclear basket nucleoporin Tpr may serve as a scaffold to the extracellular signal-regulated kinase (ERK) to regulate NPC number[193]. Some NPC components may also be involved in NPC density regulation, as in the aforementioned example of Tpr[193] or the membrane-associated Ndc1[194]. Experiments involving pharmacological treatment are likely easiest carried out in a dividing cell line treated with a cell cycle blocker to facilitate observations during interphase. One

caveat, however, is that total NPC density only minimally increases during interphase since NPC formation is accompanied by NE expansion. Cell-specificity of any identified factors should additionally be considered.

Our quantitative characterization of active neuronal NPC biogenesis provides a framework for future experiments to probe the relationship between molecular events inherent to neural development and NPC number. Several questions remain, such as whether NPC formation is induced to support the metabolic demands of processes such as synaptogenesis, neurite outgrowth, and circuit formation. Studies on NPC density in neurons with modulated synaptogenesis or activity may begin to address these questions. Conversely, analyzing the impact of physically blocking the pore central channel or inhibiting NPC transport on neurodevelopmental processes (synaptogenesis, branching, neuronal activity, etc.) could begin to address the unique functional importance of NPCs in early postnatal maturing neurons.

6.2 Determinants of NPC localization

Considerable electron microscopy work to visualize NPCs in mammalian and nonmammalian cells clearly demonstrate that NPC spatial organization is nonrandom[24,195]. Yet, how NPC distribution is determined and maintained is unknown. We observed striking, dense central plugs on the nucleoplasmic side of NE-bleb associated NPCs in torsinA-KO neurons. Similar dense plugs have been observed in newly forming pores during intermediate stages of assembly[24,45], suggesting that these plugs may represent unique machinery present in actively forming NPCs. Close inspection of these plugs hints at physical connections to the NPC basket structure, and their positioning in the nucleoplasm raises a possibility that these interact with the nuclear lamina. One speculation is that these plugs associate with the lamins and mark sites of future NPC formation; another is that these plugs are recruited soon after NPC assembly begins,

either to stabilize the nascent NPC during formation or for a localization-independent role in aiding assembly. Electron tomography studies to visualize these plugs and their associated structures in greater detail at different timepoints will shed light on the identity and function of these plugs, including their potential role in determining NPC localization.

Our data demonstrate for the first time that NPC number and spatial organization are distinctly regulated, since torsinA deletion impacts NPC localization without altering total density. It is unclear how the absence of torsinA leads to mislocalized sites of NPC biogenesis. Since torsinA resides in the NE lumen, we speculate that disrupted NPC sites are likely an indirect effect of torsinA loss. TorsinA may be critical for spatially organizing INM proteins involved in early NPC assembly; in torsinA-KO neurons, these proteins may be mislocalized and subsequently initiate NPC formation in aberrant sites. Alternatively, torsinA deletion may cause lipid abnormalities that disrupt sites of NPC biogenesis. Based on previous reports linking torsinA/torsins to lipid metabolism[105–107], we favor the possibility that NPC formation occurs in specific lipid microenvironments that are maintained by or dependent upon torsinA. Dual-labeling of NPCs with lipid sensors targeted to the nucleoplasm[163,166] could start to address whether there exists a link between defined lipid microenvironments and NPC localization.

While our findings indicate that the upstream signaling pathway leading to NPC increase is independent from factors that maintain NPC spacing, they do not rule out the possibility that shared factors may participate in both NPC upregulation and localization. For instance, a protein at the inner nuclear membrane (INM) could be the final component of the NPC upregulation pathway while simultaneously marking the site of nascent NPC formation. Based on the reports linking kinases to NPC formation[36,193], lipid-associated kinases at the INM could potentially serve such a role. Since little is known regarding NPC regulation, an imaging-based screening approach

(with a chemical library or a CRISPRi / siRNA library) could help identify candidate pathways and/or proteins that associate with torsinA to determine NPC localization. Knocking out or inhibiting the function of a protein that is involved in both NPC upregulation and localization as mentioned above, however, would result in blocked NPC upregulation and mask any role the protein may have in nascent NPC localization.

6.3 Impact of aberrant NPC biogenesis on torsinA-KO neuronal function

Our findings clearly demonstrate that NPC localization and assembly kinetics are disrupted in maturing neurons lacking torsinA. Abnormal NPC clusters are observed in neurons endogenously expressing the disease-relevant ΔE mutation, supporting the clinical relevance of aberrant NPC phenotypes. We show that excessive INM budding during NPC assembly causes NPCs to stall at a dysfunctional, incomplete stage, resulting in a temporal window during which torsinA-KO neurons have fewer functional pores compared to WT. Consistent with these data, DIV8 torsinA-KO neurons exhibit abnormal protein transport[75]. Overall RNA transport does not appear impacted, but the presence of abnormal PolyA+ puncta suggest that a subset of RNA transcripts may be abnormally localized. Future studies to understand the components that comprise these puncta are necessary to understand how they relate to torsinA loss and impact neuronal function. Furthermore, nuclear-cytoplasmic fractionation RNA-seq or single molecule FISH experiments to identify which transcripts are mislocalized would provide insights on the functional abnormalities that arise due to delayed NPC assembly.

Disrupted NPC transport in a discrete period during neuronal development may be sufficient to cause persisting neural dysfunction. Synaptogenesis, neurite outgrowth, and axonal guidance are all developmental processes that require locally translated mRNA[63,65,66,68,137], and synaptic plasticity depends on import of signaling molecules such as transcription

factors[69,71,135,136]. The finding that non-bleb associated NPCs in torsinA-KO neurons are narrower than normal NPCs suggests that the size barrier of passive diffusion across NPCs may be altered. This change may disrupt the localization of smaller proteins as well as actively transported larger molecules. Future studies using optogenetically-controlled fluorescent reporters would allow for quantitative determinations of protein import and export, individually, in torsinA mutant neurons. These investigations should be conducted in both maturing (DIV10) and mature (DIV18 or older) neurons to address whether any abnormalities identified at DIV10 resolve following NPC completion in torsinA-KO neurons. Fluorescent dextran molecules of varying sizes can be used to understand the impact of torsinA deletion on passive diffusion across NPCs. These studies should be combined with structural studies in mature neurons to address whether the narrow NPC channel size is a persisting defect. Importantly, identified abnormalities in torsinA-KO cells could then be examined in cells bearing the DYT1 genotype to further test relevance to disease pathophysiology.

Unlike the transient NE blebs and associated delay in NPC assembly, aberrant NPC clusters persist in mature torsinA-KO neurons in culture and in P70 mice[75]. Mislocalized NPCs may alter 3D chromatin organization and thereby impact gene regulation. NPCs are believed to spatiotemporally coordinate gene expression and allow facilitated transport of the nascent transcript. This gene gating hypothesis[196] is supported by electron micrographs that show heterochromatin lining the nuclear periphery except in regions near NPCs[24], and proposes that alternating heterochromatic and euchromatic regions are organized by the nonrandom spacing of NPCs. In particular, Nup153 and Nup98, which are clustered in torsinA-KO neurons, interact with chromatin and transcription machineries[25–28,178]. Approaches such as ATAC-Seq to assess open chromatin regions or CUT&RUN with an antibody to determine specific DNA regions that differentially associate with a Nup would address whether NPC spatial organization impacts

genome organization and advance our understanding of how torsinA dysfunction disrupts neuronal function.

6.4 The emergence and disappearance of NE blebs

NE blebs were first identified in relation to torsinA in mice lacking torsinA or expressing the dysfunctional ΔE/ΔE disease mutant[109]. In animal models, NE blebs emerge exclusively in post-migratory neurons during early postnatal development and resolve over time without causing cell death[95,109,156]. The morphology of NE blebs is reminiscent of two structures that have previously been published: abnormal NE herniations associated with defective NPC assembly in *S. cerevisiae* lacking Nups or ESCRT components[29,34,35], or nuclear egress of mega-mRNP granules[102,197]. We rule out nuclear egress of mega-mRNP granules as we did not observe any vesicles and all blebs clearly connected to the nuclear membrane via a pore. Our data instead support a model in which NE blebs form due to excessive INM budding during NPC assembly.

Is NE bleb formation related to aberrant NPC localization? Although the blebs observed in yeast cells correspond to defective NPCs that accumulate in clusters, these NPCs are likely mislocalized post-formation to facilitate clearance via the vacuole[34,35]. In contrast, NE blebs observed in torsinA-KO neurons are mislocalized from assembly onset and appear stable at site of formation. They are not degraded, but rather continue to assemble once blebs resolve. Mitotic cell lines lacking multiple torsin paralogs develop NE blebs related to stalled NPC assembly but do not exhibit abnormal NPC localization[107,112]. These observations indicate that blebs can form when NPC assembly is defective or stalled regardless of localization. However, it is still possible that abnormal NPC distribution and NE blebs arise due to a shared underlying defect caused by torsinA loss, such as altered lipid composition or protein distribution as discussed in section 6.2.

Similar to the reports in *in vivo* studies, NE blebs are transient *in vitro*, forming during active NPC biogenesis (DIV4–10) and disappearing as neurons continue to mature. How these blebs emerge and resolve over time are unknown. Since the outer nuclear membrane (ONM) is contiguous with the ER membrane, the extraneous membranes that contribute to bleb formation are likely derived from the ER and directed to the INM via fused INM-ONM sites at existing NPCs. One possibility is that these lipids are directed to the INM to correct abnormal lipid composition. Once the membrane homeostasis is restored, the lipids can then be absorbed back to the ER, resulting in bleb disappearance. However, it is difficult to imagine why blebs would form in yeast Nup deletion mutants since depletion of individual NPC components is not likely to cause lipid abnormalities. This discrepancy may be explained if the bleb composition is different in these yeast cells compared to torsinA-KO neurons or torsin deleted mitotic cells. Indeed, the electron density inside the blebs appear more uniform in yeast compared to what we observe in torsinA-KO neurons, which often contain membranous structures. An alternate scenario for NE bleb formation is that there may be a physical, uncharacterized machinery to drive INM budding that continues to be active when NPC subunits are not recruited in a timely manner.

We speculate that there may be developmentally dependent upregulation of proteins at the nuclear membrane that help resolve blebs. One candidate is torsinB, which has conserved functions with torsinA and whose expression increases in neural development in WT brain[95]. Interestingly, overexpressing torsinA or torsinB also causes NE blebbing[89], potentially due to sequestration of all LAP1/LULL1 and indicating that homeostasis of torsin protein levels is critical for NE integrity. Upregulation of other proteins or quality control pathways in maturing neurons may also help resolve NE blebs. ESCRT proteins surveil the NE and may play a role in this process[34,198], although no difference in CHMP4B distribution or levels are observed in torsinA-KO neurons

(data not shown). Another possibility is that the bleb membranes are absorbed into the ER while the proteins that accumulate in the blebs are degraded via a quality control pathway mediated by chaperones inside the blebs[113,115]. Our STEM data show several ONM-ER junctions at NE bleb clusters. Electron tomography studies to characterize whether blebs are significantly enriched for NE-ER junctions will provide insight into whether the ER membrane is involved in the emergence and disappearance of NE blebs.

6.5 Neuronal NPC biogenesis as a critical period

Our studies clearly demonstrate that neuronal maturation accompanies robust NPC biogenesis and provide compelling evidence that upregulated NPC formation underlies the critical period of vulnerability to torsinA dysfunction. *In vivo* characterization of NPC number indicates that NPC density plateaus and decreases in adult mice[59]. Our NPC density analysis suggests that active NPC formation may begin to plateau around DIV18, although at least one more timepoint is necessary to conclude whether similar the NPC densities measured at DIV18 and DIV24 reflects a true plateau. A valuable follow-up study based on our quantitative map of neuronal NPC formation would be to explore whether NPC biogenesis itself represents a critical period: Is NPC biogenesis limited to a neurodevelopmental window, or can new NPCs form in older neurons? These questions can be addressed using the novel HaloTag-Nup107 mouse line, which allows the use of HaloPROTAC[199] to quickly degrade HaloTag-Nup107 and destabilize NPCs. Exploring whether immature and mature neurons exhibit differences in the ability to generate new NPCs upon acute degradation of existing NPCs would address whether NPC formation itself is limited to a critical developmental window. If NPC assembly can be induced in mature neurons, treating mature torsinA-KO neurons with HaloPROTAC could then address whether NPC formation past the window of physiological neuronal maturation is still dependent on torsinA. These studies

would not only advance our understanding on the temporal requirement of torsinA function but also may be relevant for other neurological diseases in which NPCs are affected if new, functional NPC formation can indeed be induced in fully mature neurons.

6.6 Closing thoughts

Our studies newly identify early postnatal neuronal maturation as a physiological context of upregulated NPC biogenesis. Using a combination of multiple imaging approaches and quantitative analysis methods, we demonstrate that NPCs are normally evenly organized and that their spatial distribution is determined by the site of NPC assembly. In the absence of torsinA, nascent NPCs are mislocalized and form in abnormal, closely packed clusters. Simultaneously, the inner nuclear membrane excessively buds instead of fusing with the outer nuclear membrane, forming NE blebs and temporarily stalling NPC assembly. These aberrant processes result in persisting mislocalized NPC clusters and delayed NPC assembly completion, likely causing long-term defects in neuronal function. Disrupted NPC biogenesis represents the earliest phenotype related to torsinA loss or dysfunction, with NE blebs arising downstream. Our work advances the fundamental understanding of NPC biology by demonstrating that torsinA is a determinant of nascent NPC localization in neurons and providing the first evidence that NPC number and spatial organization are distinctly regulated. The unexpected involvement of torsinA in NPC localization demonstrates the power of human disease to point us to novel and important cell biological mechanisms that would otherwise be missed. These data provide a detailed quantitative map of neuronal NPC biogenesis for the first time and introduce a variety of methods and tools, including the newly generated HaloTag-Nup107 mouse line, for future studies in physiological and disease-relevant contexts. This work raises several questions for future studies, such as the mechanisms determining NPC number and localization, the precise nature of protein- and RNA-related defects

in torsinA-KO neurons, and how NE blebs are resolved. The techniques, methods, and tools used presented in thesis work and discussed in this section will help guide these future investigations.

Bibliography

1. Lin, D. H. *et al.* Architecture of the symmetric core of the nuclear pore. *Science* **352**, aaf1015–aaf1015 (2016).
2. Knockenhauer, K. E. & Schwartz, T. U. The Nuclear Pore Complex as a Flexible and Dynamic Gate. *Cell* **164**, 1162–1171 (2016).
3. Beck, M. & Hurt, E. The nuclear pore complex: understanding its function through structural insight. *Nature Reviews Molecular Cell Biology* **18**, 73–89 (2016).
4. Strambio-De-Castillia, C., Niepel, M. & Rout, M. P. The nuclear pore complex: bridging nuclear transport and gene regulation. *Nat Rev Mol Cell Biol* **11**, 490–501 (2010).
5. Mosalaganti, S. *et al.* AI-based structure prediction empowers integrative structural analysis of human nuclear pores. *Science* **376**, eabm9506 (2022).
6. Kerr, A. R. & Schirmer, E. C. FG repeats facilitate integral protein trafficking to the inner nuclear membrane. *Communicative & integrative biology* **4**, 557–9 (2011).
7. Ibáñez de Opakua, A. *et al.* Molecular interactions of FG nucleoporin repeats at high resolution. *Nat. Chem.* **14**, 1278–1285 (2022).
8. Ghavami, A., van der Giessen, E. & Onck, P. R. Energetics of Transport through the Nuclear Pore Complex. *PLOS ONE* **11**, e0148876 (2016).
9. Timney, B. L. *et al.* Simple rules for passive diffusion through the nuclear pore complex. *Journal of Cell Biology* **215**, 57–76 (2016).
10. Moore, M. S. Ran and nuclear transport. *Journal of Biological Chemistry* **273**, 22857–22860 (1998).
11. Dasso, M. The Ran GTPase: Theme and variations. *Current Biology* **12**, (2002).
12. Yudin, D. & Fainzilber, M. Ran on tracks - cytoplasmic roles for a nuclear regulator. *Journal of Cell Science* **122**, 587–593 (2009).
13. Hamada, M. *et al.* Ran-dependent docking of importin-β to RanBP2/Nup358 filaments is essential for protein import and cell viability. *The Journal of Cell Biology* **194**, (2011).
14. Kapinos, L. E., Huang, B., Rencurel, C. & Lim, R. Y. H. Karyopherins regulate nuclear pore complex barrier and transport function. *The Journal of cell biology* jcb.201702092 (2017) doi:10.1083/jcb.201702092.
15. Paci, G., Caria, J. & Lemke, E. A. Cargo transport through the nuclear pore complex at a glance. *Journal of Cell Science* **134**, jcs247874 (2021).
16. Ren, M., Drivas, G., D'Eustachio, P. & Rush, M. G. Ran/TC4: A small nuclear GTP-binding protein that regulates DNA synthesis. *Journal of Cell Biology* **120**, 313–323 (1993).
17. Görlich, D. *et al.* Two different subunits of importin cooperate to recognize nuclear localization signals and bind them to the nuclear envelope. *Current Biology* **5**, 383–392 (1995).
18. Wickramasinghe, V. O. & Laskey, R. A. Control of mammalian gene expression by selective mRNA export. *Nature Publishing Group* **16**, (2015).
19. Terry, L. J. & Wente, S. R. Nuclear mRNA export requires specific FG nucleoporins for translocation through the nuclear pore complex. *Journal of Cell Biology* **178**, 1121–1132 (2007).

20. Forler, D. *et al.* RanBP2/Nup358 provides a major binding site for NXF1-p15 dimers at the nuclear pore complex and functions in nuclear mRNA export. *Molecular and cellular biology* **24**, 1155–1167 (2004).
21. Umlauf, D. *et al.* The human TREX-2 complex is stably associated with the nuclear pore basket. *Journal of Cell Science* **126**, 2656–2667 (2013).
22. Schneider, M. *et al.* The Nuclear Pore-Associated TREX-2 Complex Employs Mediator to Regulate Gene Expression. *Cell* **162**, 1016–1028 (2015).
23. Hautbergue, G. M., Hung, M.-L., Golovanov, A. P., Lian, L.-Y. & Wilson, S. A. Mutually exclusive interactions drive handover of mRNA from export adaptors to TAP. *Proceedings of the National Academy of Sciences* **105**, 5154–5159 (2008).
24. Maul, G. G., Price, J. W. & Lieberman, M. W. Formation and Distribution of Nuclear Pore Complexes in Interphase. *Journal of Cell Biology* **51**, 405–418 (1971).
25. Capelson, M. *et al.* Chromatin-Bound Nuclear Pore Components Regulate Gene Expression in Higher Eukaryotes. *Cell* **140**, 372–383 (2010).
26. Ibarra, A. & Hetzer, M. W. Nuclear pore proteins and the control of genome functions. *Genes Dev.* **29**, 337–349 (2015).
27. Sun, J., Shi, Y. & Yildirim, E. The Nuclear Pore Complex in Cell Type-Specific Chromatin Structure and Gene Regulation. *Trends in Genetics* **35**, 579–588 (2019).
28. Kadota, S. *et al.* Nucleoporin 153 links nuclear pore complex to chromatin architecture by mediating CTCF and cohesin binding. *Nat Commun* **11**, 2606 (2020).
29. Wente, S. R. & Blobel, G. A temperature-sensitive NUP116 null mutant forms a nuclear envelope seal over the yeast nuclear pore complex thereby blocking nucleocytoplasmic traffic. *Journal of Cell Biology* **123**, 275–284 (1993).
30. Wente, S. R. & Blobel, G. NUP145 encodes a novel yeast glycine-leucine-phenylalanine-glycine (GLFG) nucleoporin required for nuclear envelope structure. *J Cell Biol* **125**, 955–969 (1994).
31. Aitchison, J. D., Blobel, G. & Rout, M. P. Nup120p: a yeast nucleoporin required for NPC distribution and mRNA transport. *J Cell Biol* **131**, 1659–1675 (1995).
32. Belgareh, N. & Doye, V. Dynamics of Nuclear Pore Distribution in Nucleoporin Mutant Yeast Cells. *J Cell Biol* **136**, 747–759 (1997).
33. Chadrin, A. *et al.* Pom33, a novel transmembrane nucleoporin required for proper nuclear pore complex distribution. *Journal of Cell Biology* **189**, 795–811 (2010).
34. Webster, B. M., Colombi, P., Jäger, J. & Lusk, C. P. Surveillance of Nuclear Pore Complex Assembly by ESCRT-III/Vps4. *Cell* **159**, 388–401 (2014).
35. Lord, C. L. & Wente, S. R. Nuclear envelope–vacuole contacts mitigate nuclear pore complex assembly stress. *Journal of Cell Biology* **219**, e202001165 (2020).
36. Maeshima, K. *et al.* Nuclear pore formation but not nuclear growth is governed by cyclin-dependent kinases (Cdks) during interphase. *Nat Struct Mol Biol* **17**, 1065–1071 (2010).
37. Kittisopikul, M. *et al.* Computational analyses reveal spatial relationships between nuclear pore complexes and specific lamins. *Journal of Cell Biology* **220**, e202007082 (2021).
38. Laurell, E. *et al.* Phosphorylation of Nup98 by Multiple Kinases Is Crucial for NPC Disassembly during Mitotic Entry. *Cell* **144**, 539–550 (2011).
39. Linder, M. I. *et al.* Mitotic Disassembly of Nuclear Pore Complexes Involves CDK1- and PLK1-Mediated Phosphorylation of Key Interconnecting Nucleoporins. *Developmental cell* **43**, 141–156 (2017).

40. Otsuka, S. & Ellenberg, J. Mechanisms of nuclear pore complex assembly – two different ways of building one molecular machine. *FEBS Letters* **592**, 475–488 (2018).
41. Anderson, D. J. & Hetzer, M. W. Nuclear envelope formation by chromatin-mediated reorganization of the endoplasmic reticulum. *Nature Cell Biology* **9**, 1160–1166 (2007).
42. Otsuka, S. *et al.* Postmitotic nuclear pore assembly proceeds by radial dilation of small membrane openings. *Nat Struct Mol Biol* **25**, 21–28 (2018).
43. Kutay, U., Jühlen, R. & Antonin, W. Mitotic disassembly and reassembly of nuclear pore complexes. *Trends in Cell Biology* **31**, 1019–1033 (2021).
44. Ellenberg, J. *et al.* Nuclear membrane dynamics and reassembly in living cells: targeting of an inner nuclear membrane protein in interphase and mitosis. *The Journal of cell biology* **138**, 1193–206 (1997).
45. Otsuka, S. *et al.* Nuclear pore assembly proceeds by an inside-out extrusion of the nuclear envelope. *eLife* **5**, e19071 (2016).
46. Zhao, G. *et al.* A tubule-sheet continuum model for the mechanism of nuclear envelope assembly. *Developmental Cell* **58**, 847-865.e10 (2023).
47. D'Angelo, M. A., Anderson, D. J., Richard, E. & Hetzer, M. W. Nuclear Pores Form de Novo from Both Sides of the Nuclear Envelope. *Science* **312**, 440–443 (2006).
48. Maul, G. G. *et al.* Time Sequence of Nuclear Pore Formation in Phytohemagglutinin-stimulated Lymphocytes and in HeLa Cells during the Cell Cycle. *Journal of Cell Biology* **55**, 433–447 (1972).
49. Walther, T. C. *et al.* The nucleoporin Nup153 is required for nuclear pore basket formation, nuclear pore complex anchoring and import of a subset of nuclear proteins. *The EMBO journal* **20**, 5703–14 (2001).
50. Doucet, C. M., Talamas, J. A. & Hetzer, M. W. Cell Cycle-Dependent Differences in Nuclear Pore Complex Assembly in Metazoa. (2010) doi:10.1016/j.cell.2010.04.036.
51. Vollmer, B. *et al.* Dimerization and direct membrane interaction of Nup53 contribute to nuclear pore complex assembly. *The EMBO journal* **31**, 4072–84 (2012).
52. Vollmer, B. *et al.* Nup153 Recruits the Nup107-160 Complex to the Inner Nuclear Membrane for Interphasic Nuclear Pore Complex Assembly. *Developmental Cell* **33**, 717–728 (2015).
53. Voeltz, G. K., Prinz, W. A., Shibata, Y., Rist, J. M. & Rapoport, T. A. A class of membrane proteins shaping the tubular endoplasmic reticulum. *Cell* **124**, 573–586 (2006).
54. Dawson, T. R., Lazarus, M. D., Hetzer, M. W. & Wente, S. R. ER membrane–bending proteins are necessary for de novo nuclear pore formation. *Journal of Cell Biology* **184**, 659–675 (2009).
55. Maul, H. M., Hsu, B. Y. L., Borun, T. M. & Maul, G. G. Effect of Metabolic Inhibitors on Nuclear Pore Formation During the HeLa S3 Cell Cycle. *J Cell Biol* **59**, 669–676 (1973).
56. Maul, G. G., Deaven, L. L., Freed, J. J., Campbell, L. M. & Beçak, W. Investigation of the determinants of nuclear pore number. *Cytogenet Genome Res* **26**, 175–190 (1980).
57. Dultz, E. & Ellenberg, J. Live imaging of single nuclear pores reveals unique assembly kinetics and mechanism in interphase. *Journal of Cell Biology* **191**, 15–22 (2010).
58. Varberg, J. M., Unruh, J. R., Bestul, A. J., Khan, A. A. & Jaspersen, S. L. Quantitative analysis of nuclear pore complex organization in Schizosaccharomyces pombe. *Life Science Alliance* **5**, (2022).
59. Lodin, Z., Blumajer, J. & Mares, V. Nuclear pore complexes in cells of the developing mouse cerebral cortex. *Acta Histochemica* **63**, 74–79 (1978).

60. Maul, G. & Deaven, L. Quantitative determination of nuclear pore complexes in cycling cells with differing DNA content. *Journal of Cell Biology* **73**, 748–760 (1977).
61. Savas, J. N., Toyama, B. H., Xu, T., Yates, J. R. & Hetzer, M. W. Extremely Long-Lived Nuclear Pore Proteins in the Rat Brain. *Science* **335**, 942–942 (2012).
62. Toyama, B. H. *et al.* Identification of Long-Lived Proteins Reveals Exceptional Stability of Essential Cellular Structures. *Cell* **154**, 971–982 (2013).
63. Sutton, M. A. & Schuman, E. M. Dendritic Protein Synthesis, Synaptic Plasticity, and Memory. *Cell* **127**, 49–58 (2006).
64. Lin, A. C. & Holt, C. E. Local translation and directional steering in axons. *The EMBO Journal* **26**, 3729–3736 (2007).
65. Jung, H., Gkogkas, C. G., Sonenberg, N. & Holt, C. E. Remote Control of Gene Function by Local Translation. *Cell* **157**, 26–40 (2014).
66. Batista, A. F. R. & Hengst, U. Intra-axonal protein synthesis in development and beyond. *International Journal of Developmental Neuroscience* **55**, 140–149 (2016).
67. Cioni, J.-M., Koppers, M. & Holt, C. E. Molecular control of local translation in axon development and maintenance. *Current Opinion in Neurobiology* **51**, 86–94 (2018).
68. Holt, C. E., Martin, K. C. & Schuman, E. M. Local translation in neurons: visualization and function. *Nat Struct Mol Biol* **26**, 557–566 (2019).
69. Kandel, E. R. The Molecular Biology of Memory Storage: A Dialogue Between Genes and Synapses. *Science* **294**, 1030–1038 (2001).
70. Thompson, K. R. *et al.* Synapse to Nucleus Signaling during Long-Term Synaptic Plasticity: a Role for the Classical Active Nuclear Import Pathway. *Neuron* **44**, 997–1009 (2004).
71. Cohen, S. & Greenberg, M. E. Communication Between the Synapse and the Nucleus in Neuronal Development, Plasticity, and Disease. *Annual Review of Cell and Developmental Biology* **24**, 183–209 (2008).
72. Basel-Vanagaite, L. *et al.* Mutated nup62 causes autosomal recessive infantile bilateral striatal necrosis. *Annals of Neurology* **60**, 214–222 (2006).
73. Harrer, P. *et al.* Recessive NUP54 Variants Underlie Early-Onset Dystonia with Striatal Lesions. *Annals of Neurology* **93**, 330–335 (2023).
74. Grima, J. C. *et al.* Mutant Huntingtin Disrupts the Nuclear Pore Complex. *Neuron* (2017) doi:10.1016/j.neuron.2017.03.023.
75. Pappas, S. S., Liang, C. C., Kim, S., Rivera, C. A. O. & Dauer, W. T. TorsinA dysfunction causes persistent neuronal nuclear pore defects. *Human Molecular Genetics* **27**, 407–420 (2018).
76. Eftekharzadeh, B. *et al.* Tau Protein Disrupts Nucleocytoplasmic Transport in Alzheimer's Disease. *Neuron* (2018) doi:10.1016/j.neuron.2018.07.039.
77. Coyne, A. N. *et al.* G4C2 Repeat RNA Initiates a POM121-Mediated Reduction in Specific Nucleoporins in C9orf72 ALS/FTD. *Neuron* **107**, 1124-1140.e11 (2020).
78. Lin, Y.-C. *et al.* Interactions between ALS-linked FUS and nucleoporins are associated with defects in the nucleocytoplasmic transport pathway. *Nat Neurosci* **24**, 1077–1088 (2021).
79. Ozelius, L. J. *et al.* Fine localization of the torsion dystonia gene (DYT1) on human chromosome 9q34: YAC map and linkage disequilibrium. *Genome Research* **7**, 483–494 (1997).
80. Ozelius, L. J. *et al.* The early-onset torsion dystonia gene (DYT1) encodes an ATP-binding protein. *Nat Genet* **17**, 40–48 (1997).

81. Ozelius, L. J. *et al.* The TOR1A (DYT1) gene family and its role in early onset torsion dystonia. *Genomics* **62**, 377–384 (1999).
82. Bressman, S. B. *et al.* The DYT1 phenotype and guidelines for diagnostic testing. *Neurology* **54**, 1746–52 (2000).
83. Vidailhet, M., Jutras, M.-F., Grabli, D. & Roze, E. Deep brain stimulation for dystonia. *J Neurol Neurosurg Psychiatry* **84**, 1029–1042 (2013).
84. Hewett, J. *et al.* TorsinA in PC12 cells: Localization in the endoplasmic reticulum and response to stress. *Journal of Neuroscience Research* **72**, 158–168 (2003).
85. Goodchild, R. E. & Dauer, W. T. Mislocalization to the nuclear envelope: An effect of the dystonia-causing torsinA mutation. *Proceedings of the National Academy of Sciences* **101**, 847–852 (2004).
86. Naismith, T. V., Heuser, J. E., Breakefield, X. O. & Hanson, P. I. TorsinA in the nuclear envelope. *Proceedings of the National Academy of Sciences* **101**, 7612–7617 (2004).
87. Rose, A. E., Brown, R. S. H. & Schlieker, C. Torsins: not your typical AAA+ ATPases. *Critical Reviews in Biochemistry and Molecular Biology* **50**, 532–549 (2015).
88. Goodchild, R. E. & Dauer, W. T. The AAA+ protein torsinA interacts with a conserved domain present in LAP1 and a novel ER protein. *Journal of Cell Biology* **168**, 855–862 (2005).
89. Kim, C. E., Perez, A., Perkins, G., Ellisman, M. H. & Dauer, W. T. A molecular mechanism underlying the neural-specific defect in torsinA mutant mice. *Proceedings of the National Academy of Sciences* **107**, 9861–9866 (2010).
90. Zhao, C., Brown, R. S. H., Chase, A. R., Eisele, M. R. & Schlieker, C. Regulation of Torsin ATPases by LAP1 and LULL1. *Proceedings of the National Academy of Sciences* **110**, E1545–E1554 (2013).
91. Brown, R. S. H., Zhao, C., Chase, A. R., Wang, J. & Schlieker, C. The mechanism of Torsin ATPase activation. *Proceedings of the National Academy of Sciences of the United States of America* **111**, E4822-31 (2014).
92. Chase, A. R., Laudermilch, E. & Schlieker, C. Torsin ATPases: Harnessing Dynamic Instability for Function. *Frontiers in Molecular Biosciences* **4**, 1–7 (2017).
93. Demircioglu, F. E. *et al.* The AAA + ATPase TorsinA polymerizes into hollow helical tubes with 8.5 subunits per turn. *Nat Commun* **10**, 3262 (2019).
94. Jungwirth, M., Dear, M. L., Brown, P., Holbrook, K. & Goodchild, R. Relative tissue expression of homologous torsinB correlates with the neuronal specific importance of DYT1 dystonia-associated torsinA. *Human Molecular Genetics* **19**, 888–900 (2010).
95. Tanabe, L. M., Liang, C. C. & Dauer, W. T. Neuronal Nuclear Membrane Budding Occurs during a Developmental Window Modulated by Torsin Paralogs. *Cell Reports* **16**, 3322–3333 (2016).
96. McLean, P. J. *et al.* TorsinA and heat shock proteins act as molecular chaperones: suppression of alpha-synuclein aggregation. *Journal of neurochemistry* **83**, 846–854 (2002).
97. Hewett, J. W. *et al.* Mutant torsinA interferes with protein processing through the secretory pathway in DYT1 dystonia cells. *Proceedings of the National Academy of Sciences* **104**, 7271–7276 (2007).
98. Chen, P. *et al.* The early-onset torsion dystonia-associated protein, torsinA, is a homeostatic regulator of endoplasmic reticulum stress response. *Human Molecular Genetics* **19**, 3502–3515 (2010).

99. Nery, F. C. *et al.* TorsinA participates in endoplasmic reticulum-associated degradation. *Nature Communications* **2**, (2011).
100. Rittiner, J. E. *et al.* Functional Genomic Analyses of Mendelian and Sporadic Disease Identify Impaired eIF2α Signaling as a Generalizable Mechanism for Dystonia. *Neuron* **92**, 1238–1251 (2016).
101. György, B. *et al.* Mutant torsinA in the heterozygous DYT1 state compromises HSV propagation in infected neurons and fibroblasts. *Sci Rep* **8**, 2324 (2018).
102. Jokhi, V. *et al.* Torsin Mediates Primary Envelopment of Large Ribonucleoprotein Granules at the Nuclear Envelope. *Cell Reports* **3**, 988–995 (2013).
103. Valastyan, J. S. & Lindquist, S. TorsinA and the TorsinA-Interacting Protein Printor Have No Impact on Endoplasmic Reticulum Stress or Protein Trafficking in Yeast. *PLOS ONE* **6**, e22744 (2011).
104. Esra Demircioglu, F., Sosa, B. A., Ingram, J., Ploegh, H. L. & Schwartz, T. U. Structures of torsinA and its disease-mutant complexed with an activator reveal the molecular basis for primary dystonia. *eLife* **5**, (2016).
105. Grillet, M. *et al.* Torsins Are Essential Regulators of Cellular Lipid Metabolism. *Developmental Cell* **38**, 235–247 (2016).
106. Cascalho, A. *et al.* Excess Lipin enzyme activity contributes to TOR1A recessive disease and DYT-TOR1A dystonia. *Brain* **143**, 1746–1765 (2020).
107. Jacquemyn, J. *et al.* Torsin and NEP1R1-CTDNEP1 phosphatase affect interphase nuclear pore complex insertion by lipid-dependent and lipid-independent mechanisms. *The EMBO Journal* **40**, e106914 (2021).
108. Shin, J.-Y. *et al.* Nuclear envelope–localized torsinA-LAP1 complex regulates hepatic VLDL secretion and steatosis. *J Clin Invest* **129**, 4885–4900 (2019).
109. Goodchild, R. E., Kim, C. E. & Dauer, W. T. Loss of the dystonia-associated protein torsinA selectively disrupts the neuronal nuclear envelope. *Neuron* **48**, 923–932 (2005).
110. VanGompel, M. J. W., Nguyen, K. C. Q., Hall, D. H., Dauer, W. T. & Rose, L. S. A novel function for the Caenorhabditis elegans torsin OOC-5 in nucleoporin localization and nuclear import. *MBoC* **26**, 1752–1763 (2015).
111. Laudermilch, E. *et al.* Dissecting Torsin/cofactor function at the nuclear envelope: a genetic study. *Molecular Biology of the Cell* **27**, 3964–3971 (2016).
112. Rampello, A. J. *et al.* Torsin ATPase deficiency leads to defects in nuclear pore biogenesis and sequestration of MLF2. *Journal of Cell Biology* **219**, e201910185 (2020).
113. Prophet, S. M. *et al.* Atypical nuclear envelope condensates linked to neurological disorders reveal nucleoporin-directed chaperone activities. *Nat Cell Biol* **24**, 1630–1641 (2022).
114. Liang, C. C., Tanabe, L. M., Jou, S., Chi, F. & Dauer, W. T. TorsinA hypofunction causes abnormal twisting movements and sensorimotor circuit neurodegeneration. *Journal of Clinical Investigation* **124**, 3080–3092 (2014).
115. Kuiper, E. F. E. *et al.* The chaperone DNAJB6 surveils FG-nucleoporins and is required for interphase nuclear pore complex biogenesis. *Nat Cell Biol* **24**, 1584–1594 (2022).
116. Vasudevan, A., Breakefield, X. O. & Bhide, P. G. Developmental patterns of torsinA and torsinB expression. *Brain Research* **1073–1074**, 139–145 (2006).
117. Li, J., Liang, C.-C., Pappas, S. S. & Dauer, W. T. TorsinB overexpression prevents abnormal twisting in DYT1 dystonia mouse models. *eLife* **9**, e54285 (2020).

118. Li, J., Levin, D. S., Kim, A. J., Pappas, S. S. & Dauer, W. T. TorsinA restoration in a mouse model identifies a critical therapeutic window for DYT1 dystonia. *J Clin Invest* **131**, (2021).
119. Zhang, Y. *et al.* Rapid Single-Step Induction of Functional Neurons from Human Pluripotent Stem Cells. *Neuron* **78**, 785–798 (2013).
120. Gupta, S. *et al.* Fibroblast growth factor 2 regulates activity and gene expression of human post-mitotic excitatory neurons. *J Neurochem* **145**, 188–203 (2018).
121. Grimm, J. B. *et al.* A general method to improve fluorophores for live-cell and single-molecule microscopy. *Nat Methods* **12**, 244–250 (2015).
122. Grimm, J. B. *et al.* A General Method to Improve Fluorophores Using Deuterated Auxochromes. *JACS Au* **1**, 690–696 (2021).
123. Niopek, D., Wehler, P., Roensch, J., Eils, R. & Di Ventura, B. Optogenetic control of nuclear protein export. *Nat Commun* **7**, 10624 (2016).
124. Chozinski, T. J. *et al.* Expansion Microscopy with Conventional Antibodies and Fluorescent Proteins. *Nat Methods* **13**, 485–488 (2016).
125. Asano, S. M. *et al.* Expansion Microscopy: Protocols for Imaging Proteins and RNA in Cells and Tissues. *Curr Protoc Cell Biol* **80**, e56 (2018).
126. Gambarotto, D. *et al.* Imaging cellular ultrastructures using expansion microscopy (U-ExM). *Nat Methods* **16**, 71–74 (2019).
127. Phan, S. *et al.* 3D reconstruction of biological structures: automated procedures for alignment and reconstruction of multiple tilt series in electron tomography. *Adv Struct Chem Imaging* **2**, 8 (2016).
128. Shaw, T. R. *et al.* Estimating the localization spread function of static single-molecule localization microscopy images. *Biophysical Journal* **121**, 2906–2920 (2022).
129. Ester, M., Kriegel, H.-P., Sander, J. & Xu, X. A Density-Based Algorithm for Discovering Clusters in Large Spatial Databases with Noise.
130. Heydarian, H. *et al.* Template-free 2D particle fusion in localization microscopy. *Nat Methods* **15**, 781–784 (2018).
131. Veatch, S. L. *et al.* Correlation Functions Quantify Super-Resolution Images and Estimate Apparent Clustering Due to Over-Counting. *PLOS ONE* **7**, e31457 (2012).
132. Schindelin, J. *et al.* Fiji: an open-source platform for biological-image analysis. *Nat Methods* **9**, 676–682 (2012).
133. Zhang, K. *et al.* The C9orf72 repeat expansion disrupts nucleocytoplasmic transport. *Nature* **525**, 56–61 (2015).
134. Lord, S. J., Velle, K. B., Mullins, R. D. & Fritz-Laylin, L. K. SuperPlots: Communicating reproducibility and variability in cell biology. *Journal of Cell Biology* **219**, e202001064 (2020).
135. Karpova, A. *et al.* Encoding and Transducing the Synaptic or Extrasynaptic Origin of NMDA Receptor Signals to the Nucleus. *Cell* **152**, 1119–1133 (2013).
136. Kaushik, R., Grochowska, K. M., Butnaru, I. & Kreutz, M. R. Protein trafficking from synapse to nucleus in control of activity-dependent gene expression. *Neuroscience* **280**, 340–350 (2014).
137. Sutton, M. A. & Schuman, E. M. Local translational control in dendrites and its role in long-term synaptic plasticity. *Journal of Neurobiology* **64**, 116–131 (2005).
138. Lesuisse, C. & Martin, L. J. Long-term culture of mouse cortical neurons as a model for neuronal development, aging, and death. *Journal of Neurobiology* **51**, 9–23 (2002).

139. Chambers, S. M. *et al.* Highly efficient neural conversion of human ES and iPS cells by dual inhibition of SMAD signaling. *Nat Biotechnol* **27**, 275–280 (2009).
140. Mosalaganti, S. *et al.* In situ architecture of the algal nuclear pore complex. *Nat Commun* **9**, 2361 (2018).
141. Lin, D. H. & Hoelz, A. The Structure of the Nuclear Pore Complex (An Update). *Annu Rev Biochem* **88**, 725–783 (2019).
142. Los, G. V. *et al.* HaloTag: A Novel Protein Labeling Technology for Cell Imaging and Protein Analysis. *ACS Publications* https://pubs.acs.org/doi/pdf/10.1021/cb800025k (2008) doi:10.1021/cb800025k.
143. Rabut, G., Doye, V. & Ellenberg, J. Mapping the dynamic organization of the nuclear pore complex inside single living cells. *Nat Cell Biol* **6**, 1114–1121 (2004).
144. Shi, Y., Kirwan, P. & Livesey, F. J. Directed differentiation of human pluripotent stem cells to cerebral cortex neurons and neural networks. *Nat Protoc* **7**, 1836–1846 (2012).
145. Doucet, C. M., Talamas, J. A. & Hetzer, M. W. Cell Cycle-Dependent Differences in Nuclear Pore Complex Assembly in Metazoa. (2010) doi:10.1016/j.cell.2010.04.036.
146. Otsuka, S. *et al.* A quantitative map of nuclear pore assembly reveals two distinct mechanisms. *Nature* **613**, 575–581 (2023).
147. Doucet, C. M. & Hetzer, M. W. Nuclear pore biogenesis into an intact nuclear envelope. *Chromosoma* **119**, 469–477 (2010).
148. Thevathasan, J. V. *et al.* Nuclear pores as versatile reference standards for quantitative superresolution microscopy. *Nat Methods* **16**, 1045–1053 (2019).
149. Chou, Y.-Y. *et al.* Inherited nuclear pore substructures template post-mitotic pore assembly. *Developmental Cell* **56**, 1786-1803.e9 (2021).
150. Kustedjo, K., Bracey, M. H. & Cravatt, B. F. Torsin A and Its Torsion Dystonia-associated Mutant Forms Are Lumenal Glycoproteins That Exhibit Distinct Subcellular Localizations*. *Journal of Biological Chemistry* **275**, 27933–27939 (2000).
151. Gonzalez-Alegre, P. & Paulson, H. L. Aberrant Cellular Behavior of Mutant TorsinA Implicates Nuclear Envelope Dysfunction in DYT1 Dystonia. *J. Neurosci.* **24**, 2593–2601 (2004).
152. Gerace, L. TorsinA and torsion dystonia: Unraveling the architecture of the nuclear envelope. *Proceedings of the National Academy of Sciences* **101**, 8839–8840 (2004).
153. Callan, A. C., Bunning, S., Jones, O. T., High, S. & Swanton, E. Biosynthesis of the dystonia-associated AAA+ ATPase torsinA at the endoplasmic reticulum. *Biochemical Journal* **401**, 607–612 (2006).
154. Nery, F. C. *et al.* TorsinA binds the KASH domain of nesprins and participates in linkage between nuclear envelope and cytoskeleton. *Journal of Cell Science* **121**, 3476–3486 (2008).
155. Vander Heyden, A. B., Naismith, T. V., Snapp, E. L., Hodzic, D. & Hanson, P. I. LULL1 retargets TorsinA to the nuclear envelope revealing an activity that is impaired by the DYT1 dystonia mutation. *Molecular biology of the cell* **20**, 2661–72 (2009).
156. Pappas, S. S. *et al.* Forebrain deletion of the dystonia protein torsinA causes dystonic-like movements and loss of striatal cholinergic neurons. *eLife* **4**, e08352 (2015).
157. Wälde, S. *et al.* The Nucleoporin Nup358/RanBP2 Promotes Nuclear Import in a Cargo- and Transport Receptor-Specific Manner. *Traffic* **13**, 218–233 (2012).
158. Bernad, R., van der Velde, H., Fornerod, M. & Pickersgill, H. Nup358/RanBP2 Attaches to the Nuclear Pore Complex via Association with Nup88 and Nup214/CAN and Plays a

Supporting Role in CRM1-Mediated Nuclear Protein Export. *Molecular and Cellular Biology* **24**, 2373–2384 (2004).
159. Maul, G. G. The nuclear and the cytoplasmic pore complex: structure, dynamics, distribution, and evolution. *Int Rev Cytol Suppl* 75–186 (1977).
160. Bucci, M. & Wente, S. R. In vivo dynamics of nuclear pore complexes in yeast. *J Cell Biol* **136**, 1185–1199 (1997).
161. Mattaj, I. W. Sorting out the nuclear envelope from the endoplasmic reticulum. *Nat Rev Mol Cell Biol* **5**, 65–69 (2004).
162. Iino, H. *et al.* Live imaging system for visualizing nuclear pore complex (NPC) formation during interphase in mammalian cells. *Genes to Cells* **15**, 647–660 (2010).
163. Romanauska, A. & Köhler, A. The Inner Nuclear Membrane Is a Metabolically Active Territory that Generates Nuclear Lipid Droplets. *Cell* **174**, 700-715.e18 (2018).
164. Ohsaki, Y. *et al.* PML isoform II plays a critical role in nuclear lipid droplet formation. *Journal of Cell Biology* **212**, 29–38 (2016).
165. Merta, H. & Bahmanyar, S. The Inner Nuclear Membrane Takes On Lipid Metabolism. *Developmental Cell* **47**, 397–399 (2018).
166. Sołtysik, K., Ohsaki, Y., Tatematsu, T., Cheng, J. & Fujimoto, T. Nuclear lipid droplets derive from a lipoprotein precursor and regulate phosphatidylcholine synthesis. *Nat Commun* **10**, 473 (2019).
167. Sołtysik, K. *et al.* Nuclear lipid droplets form in the inner nuclear membrane in a seipin-independent manner. *Journal of Cell Biology* **220**, e202005026 (2021).
168. Lee, S., Merta, H., Rodríguez, J. W. C. & Bahmanyar, S. A membrane sensing mechanism couples local lipid metabolism to protein degradation at the inner nuclear membrane. 2022.07.06.498903 Preprint at https://doi.org/10.1101/2022.07.06.498903 (2022).
169. Keuenhof, K. S. *et al.* Nuclear envelope budding and its cellular functions. *Nucleus* **14**, 2178184 (2023).
170. Ding, B. *et al.* Disease Modeling with Human Neurons Reveals LMNB1 Dysregulation Underlying DYT1 Dystonia. *J. Neurosci.* **41**, 2024–2038 (2021).
171. Quartarone, A. & Hallett, M. Emerging concepts in the physiological basis of dystonia. *Mov Disord* **28**, 958–967 (2013).
172. Quartarone, A. & Ghilardi, M. F. Chapter 14 - Neuroplasticity in dystonia: Motor symptoms and beyond. in *Handbook of Clinical Neurology* (eds. Quartarone, A., Ghilardi, M. F. & Boller, F.) vol. 184 207–218 (Elsevier, 2022).
173. Yellajoshyula, D., Opeyemi, S., Dauer, W. T. & Pappas, S. S. Genetic evidence of aberrant striatal synaptic maturation and secretory pathway alteration in a dystonia mouse model. *Dystonia* **0**, (2022).
174. Song, C.-H. *et al.* Subtle microstructural changes of the striatum in a DYT1 knock-in mouse model of dystonia. *Neurobiology of Disease* **54**, 362–371 (2013).
175. Song, C.-H., Bernhard, D., Hess, E. J. & Jinnah, H. A. Subtle microstructural changes of the cerebellum in a knock-in mouse model of DYT1 dystonia. *Neurobiology of Disease* **62**, 372–380 (2014).
176. Vanni, V. *et al.* Cerebellar synaptogenesis is compromised in mouse models of DYT1 dystonia. *Experimental Neurology* **271**, 457–467 (2015).
177. Maltese, M. *et al.* Early structural and functional plasticity alterations in a susceptibility period of DYT1 dystonia mouse striatum. *eLife* **7**, e33331 (2018).

178. Pascual-Garcia, P. *et al.* Metazoan Nuclear Pores Provide a Scaffold for Poised Genes and Mediate Induced Enhancer-Promoter Contacts. *Mol Cell* **66**, 63-76.e6 (2017).
179. Li, J., Kim, S., Pappas, S. S. & Dauer, W. T. CNS critical periods: implications for dystonia and other neurodevelopmental disorders. *JCI Insight* **6**, (2021).
180. Albanese, A. *et al.* EFNS guidelines on diagnosis and treatment of primary dystonias. *European Journal of Neurology* **18**, 5–18 (2011).
181. Akbari, M. T., Zand, Z., Shahidi, G. A. & Hamid, M. Clinical Features, DYT1 Mutation Screening and Genotype-Phenotype Correlation in Patients with Dystonia from Iran. *Medical Principles and Practice* **21**, 462–466 (2012).
182. Hubel, D. H. & Wiesel, T. N. The period of susceptibility to the physiological effects of unilateral eye closure in kittens. *The Journal of Physiology* **206**, 419–436 (1970).
183. Sonzogni, M. *et al.* Delayed loss of UBE3A reduces the expression of Angelman syndrome-associated phenotypes. *Molecular Autism* **10**, 23 (2019).
184. Clement, J. P. *et al.* Pathogenic SYNGAP1 Mutations Impair Cognitive Development by Disrupting Maturation of Dendritic Spine Synapses. *Cell* **151**, 709–723 (2012).
185. Tanaka, K. F. *et al.* Flexible Accelerated STOP Tetracycline Operator-Knockin (FAST): A Versatile and Efficient New Gene Modulating System. *Biological Psychiatry* **67**, 770–773 (2010).
186. Giles, L. M., Chen, J., Li, L. & Chin, L.-S. Dystonia-associated mutations cause premature degradation of torsinA protein and cell-type-specific mislocalization to the nuclear envelope. *Human Molecular Genetics* **17**, 2712–2722 (2008).
187. Pankiewicz, R., Karlen, Y., Imhof, M. O. & Mermod, N. Reversal of the silencing of tetracycline-controlled genes requires the coordinate action of distinctly acting transcription factors. *The Journal of Gene Medicine* **7**, 117–132 (2005).
188. Oyer, J. A., Chu, A., Brar, S. & Turker, M. S. Aberrant Epigenetic Silencing Is Triggered by a Transient Reduction in Gene Expression. *PLoS One* **4**, e4832 (2009).
189. Gödecke, N. *et al.* Controlled re-activation of epigenetically silenced Tet promoter-driven transgene expression by targeted demethylation. *Nucleic Acids Res* **45**, e147 (2017).
190. Callan, H. G., Tomlin, S. G. & Waddington, C. H. Experimental studies on amphibian oocyte nuclei I. Investigation of the structure of the nuclear membrane by means of the electron microscope. *Proceedings of the Royal Society of London. Series B - Biological Sciences* **137**, 367–378 (1950).
191. Guelen, L. *et al.* Domain organization of human chromosomes revealed by mapping of nuclear lamina interactions. *Nature* **453**, 948–951 (2008).
192. Steensel, B. van & Belmont, A. S. Lamina-Associated Domains: Links with Chromosome Architecture, Heterochromatin, and Gene Repression. *Cell* **169**, 780–791 (2017).
193. McCloskey, A., Ibarra, A. & Hetzer, M. W. Tpr regulates the total number of nuclear pore complexes per cell nucleus. *Genes Dev.* **32**, 1321–1331 (2018).
194. Mauro, M. S. *et al.* Ndc1 drives nuclear pore complex assembly independent of membrane biogenesis to promote nuclear formation and growth. *eLife* **11**, e75513 (2022).
195. Markovics, J., Glass, L. & Maul, G. G. Pore patterns on nuclear membranes. *Experimental Cell Research* **85**, 443–451 (1974).
196. Blobel, G. Gene gating: a hypothesis. *Proceedings of the National Academy of Sciences* **82**, 8527–8529 (1985).
197. Speese, S. D. *et al.* Nuclear Envelope Budding Enables Large Ribonucleoprotein Particle Export during Synaptic Wnt Signaling. *Cell* **149**, 832–846 (2012).

198. Thaller, D. J. *et al.* An ESCRT-LEM protein surveillance system is poised to directly monitor the nuclear envelope and nuclear transport system. *eLife* **8**, e45284 (2019).
199. Buckley, D. L. *et al.* HaloPROTACS: Use of Small Molecule PROTACs to Induce Degradation of HaloTag Fusion Proteins. *ACS Chem. Biol.* **10**, 1831–1837 (2015).